UNIWERSYTET ŚLĄSKI
W KATOWICACH

Uniwersytet Śląski w Katowicach
Wydział Nauk Ścisłych i Technicznych
Instytut Fizyki im. Augusta Chełkowskiego

ROZPRAWA DOKTORSKA

Obraz dynamiki reorientacyjnej dużych i anizotropowych molekuł w stanie krystalicznym i amorficznym na podstawie badań spektroskopią dielektryczną

mgr Alfred Błażytko

Promotor: prof. dr hab. Marian Paluch
Promotor pomocniczy: dr hab. Marzena Rams-Baron, prof. UŚ

Chorzów 2026

Pragnę złożyć wyrazy wdzięczności mojemu promotorowi, prof. dr. hab. Marianowi Paluchowi za nieocenione wsparcie merytoryczne, opiekę naukową, inspirujące dyskusje oraz możliwość pracy w grupie badawczej.

Serdeczne podziękowania składam również mojej promotor pomocniczej, dr hab. Marzenie Rams-Baron, prof. UŚ, za przekazaną wiedzę, opiekę, cierpliwość i motywację, a także nieustanne wsparcie przy realizacji badań i tworzeniu publikacji.

Wyrazy wdzięczności składam wszystkim Kolegom, Koleżankom i Współpracownikom z grupy badawczej za miłą atmosferę pracy, wszelką przekazaną wiedzę, pomoc w rozwiązywaniu problemów i wspólnie spędzony czas.

NARODOWE CENTRUM NAUKI

Badania przeprowadzone na potrzeby niniejszej rozprawy doktorskiej finansowane były w ramach projektu Narodowego Centrum Nauki - OPUS 21, pt. „W kierunku zrozumienia dynamiki reorientacji sztywnych i niesztywnych, dużych anizotropowych cząsteczek stanowiących nową klasę materiałów szklistych o osobliwych własnościach relaksacyjnych ujawnionych w badaniach relaksacji dielektrycznej” (Nr 2021/41/B/ST5/00992), którego kierownikiem jest dr hab. Marzena Rams-Baron, prof. UŚ.

Spis treści

1. Wstęp

Rotory molekularne od kilku dekad stanowią istotny przedmiot badań w kontekście projektowania nanoskalowych układów dynamicznych i elementów przyszłych maszyn molekularnych. Wraz z postępującą miniaturyzacją elektroniki oraz robotyki w ostatnich latach coraz częściej podnoszony jest temat wykorzystania pojedynczych molekuł jako rozwiązanie problemu limitu klasycznego podejścia do urządzeń mechanicznych. Dodatkowo rosnąca liczba publikacji świadczy o wzroście zainteresowania tym aspektem wśród fizyków, chemików oraz inżynierów, którzy zgłębiają mechanizmy powstawania i kontrolowania rotacji molekularnej (*1–6*).

W zależności od stanu materii rotacja molekularna przyjmuje zasadniczo odmienne formy. W cieczach, w których oddziaływania międzycząsteczkowe ulegają nieustannym fluktuacjom, obrót całych molekuł lub ich wybranych fragmentów może zachodzić stosunkowo swobodnie i szybko. Sytuacja ulega istotnej zmianie w cieczy przechłodzonej, gdzie wraz z obniżaniem temperatury dochodzi do silnego spowolnienia dynamiki rotacyjnej (*7*). W wyniku braku dalekosiężnego uporządkowania krystalicznego ruch obrotowy nie zanika spontanicznie, lecz staje się coraz wolniejszy i bardziej heterogeniczny przestrzennie i czasowo (*8*, *9*). Co więcej, w pobliżu temperatury zeszklenia (T_g) dynamika orientacyjna całych molekuł zostaje silnie spowolniona i osiąga skalę wykraczającą poza okna pomiarowe dostępnej aparatury eksperymentalnej. W stanie szklistym, mimo makroskopowego „zamrożenia" struktury, niektóre stopnie swobody rotacyjnej mogą nadal pozostawać aktywne. Dotyczy to zwłaszcza niewielkich grup bocznych, fragmentów o budowie sprzyjającej reorientacji lub elementów osadzonych w relatywnie swobodnym otoczeniu energetycznym (*10*). Ich ruch ma zwykle charakter lokalny, aktywowany termicznie i skokowy, a obserwowane procesy są często interpretowane w kategoriach pokonywania barier potencjału pomiędzy minimami energetycznymi (*11*, *12*). Z tego względu szkło nie powinno być traktowane jako układ całkowicie statyczny, lecz raczej jako ośrodek, w którym globalna sztywność może współistnieć z ograniczoną, lecz mierzalną dynamiką wewnątrzcząsteczkową.

Podczas obniżania temperatury alternatywnie do metastabilnego szkła układ może przyjąć formę kryształu, czyli stanu równowagowego o wysoce uporządkowanej strukturze. Taki stan materii zazwyczaj wiąże się z faktem, że dynamika orientacyjna molekuł zostaje całkowicie zatrzymana przez silne oddziaływania z sąsiednimi cząsteczkami. Istnieją jednak pewne unikalne odmiany kryształów, które łączą cechy porządku i ruchu.

Szczególnie interesującą klasę materiałów stanowią opisane na początku XXI wieku przez M. A. Garcia-Garibaya kryształy amfidynamiczne (*13*). Molekuły tworzące taką fazę można podzielić na dwie podjednostki - nieruchomy stator i dynamiczny rotor. Stator odpowiada za utrzymanie uporządkowania krystalicznego, natomiast rotor zachowuje zdolność do termicznie aktywowanej reorientacji. O możliwości wystąpienia rotacji decyduje nie tylko sama budowa chemiczna rotora, lecz również lokalna wolna objętość, geometria statora, gęstość upakowania, jak również charakter oddziaływań międzycząsteczkowych (*5*, *6*). Taka sytuacja sprawia, że kryształy amfidynamiczne są wyjątkowo atrakcyjne z punktu widzenia badań podstawowych, ponieważ umożliwiają analizę ruchu obrotowego w dobrze zdefiniowanym, homogenicznym środowisku, a zarazem oferują możliwość projektowania materiałów o kontrolowanych właściwościach dynamicznych.

W literaturze opisano kilka głównych strategii projektowania kryształów amfidynamicznych. W jednych układach swoboda rotacji uzyskiwana jest dzięki obecności rozbudowanego statora, który osłania rotor i tworzy wokół niego lokalną, wolną objętość (*6*, *14–19*). W innych przypadkach kluczowe znaczenie ma luźniejsze upakowanie cząsteczek lub obecność porów, jak w niektórych strukturach typu MOF (ang. *metal-organic framework*) (*20–23*). Odrębną grupę stanowią kokryształy i układy supramolekularne, w których dynamika rotacyjna jest regulowana przez sieć oddziaływań niekowalencyjnych (*24*, *25*). Pomimo znacznego postępu w projektowaniu krystalicznych rotorów molekularnych nadal istotnym problemem pozostaje określenie, w jaki sposób uporządkowane otoczenie krystaliczne wpływa na parametry wewnętrznej rotacji. Większość dotychczasowych strategii koncentrowała się na modyfikacji architektury statora i/lub rotora w celu zapewnienia odpowiedniej wolnej objętości oraz ograniczenia niekorzystnych kontaktów sterycznych. Znacznie słabiej poznanym zagadnieniem jest natomiast możliwość kontrolowania dynamiki rotacji poprzez zmianę sposobu upakowania tych samych cząsteczek w różnych formach krystalicznych. Z tego względu szczególnie interesujące staje się badanie zjawiska polimorfizmu jako narzędzia modyfikowania lokalnego krajobrazu barier energetycznych bez konieczności zmiany budowy chemicznej molekuły. Korzyści wynikające z takiego podejścia w swoich teoretycznych rozważaniach wskazał M. A. Garcia-Garibay ponad 20 lat temu. Jednak pomimo upływu wielu lat wciąż brakuje systematycznych badań eksperymentalnych, które bezpośrednio wiązałyby polimorfizm z modyfikacją bariery rotacji w kryształach amfidynamicznych (*13*).

W badaniach dynamiki rotacji standardową praktyką jest wykorzystywanie spektroskopii magnetycznego rezonansu jądrowego (NMR – ang. *nuclear magnetic resonance*). Technika ta umożliwia bezpośrednią i lokalnie selektywną obserwację ruchu rotorów. W szczególności

^{2}H NMR w ciele stałym znalazł szerokie zastosowanie w badaniach dynamiki amfidynamicznych kryształów i układów amorficznych (*4*, *26–28*). Należy jednak podkreślić, że metoda ta charakteryzuje się stosunkowo niewielkim zakresem badanych częstotliwości, obejmującym zazwyczaj przedział około 10^3 - 10^7 Hz (*15*, *26*). Ograniczenie to staje się szczególnie widoczne w porównaniu z szerokopasmową spektroskopią dielektryczną (BDS – ang. *broadband dielectric spectroscopy*), która umożliwia badanie procesów relaksacyjnych w wyjątkowo szerokim zakresie częstotliwości, bo sięgającym aż 18 rzędów wielkości (*26*, *29*). Najczęściej badany zakres przy użyciu popularnych analizatorów (np. Alpha-A firmy Novocontrol) mieści się w przedziale od 10^{-6} do 10^7 Hz, lecz przy zastosowaniu odpowiednich technik wysokoczęstotliwościowych możliwe jest rozszerzenie tego zakresu aż do 10^{12} Hz (*29*, *30*). Co istotne, kluczowym warunkiem, aby zaobserwować ruch orientacyjny za pomocą techniki BDS jest zmiana momentu dipolowego podczas jego zachodzenia. To implikuje możliwość badania wyłącznie polarnych rotorów. Do tej pory spektroskopia dielektryczna była bardzo rzadko wykorzystywana w badaniach rotacji w amfidynamicznych kryształach, o czym świadczy obecność tylko kilku artykułów naukowych, w których badacze wykorzystali tę technikę (*22*, *31–35*).

Na tle opisanych w literaturze typów kryształów amfidynamicznych badane w niniejszej rozprawie cząsteczki reprezentują szczególnie interesujący wariant architektury molekularnej. Nie są to klasyczne układy, w których rotor jest całkowicie osłonięty przez rozbudowaną ramę statora, ani struktury porowate typu MOF, w których ruch zachodzi w relatywnie dużych kanałach lub wnękach. W analizowanych związkach rotujący pierścień fenylowy z polarnym podstawnikiem jest połączony jednostronnie z masywnym, słabo polarnym rdzeniem pełniącym funkcję statora. Obecność donora momentu dipolowego w rotującym fragmencie badanych przeze mnie molekuł pozwoliła wykorzystać BDS jako główną technikę badawczą. W tej roli wykorzystano atom fluoru lub grupę trifluorometylową, które zostały podstawione w pozycji *orto*, *meta* lub *para*. Architektura cząsteczki sprawia, że rotor zachowuje pewien stopień swobody orientacyjnej, ale jednocześnie pozostaje silnie narażony na lokalne oddziaływania z sąsiednimi cząsteczkami. Ponadto niezwykle interesujący jest fakt, że niektóre wykorzystywane przeze mnie molekuły mają zdolność do tworzenia różnych odmian polimorficznych. W związku z tym układy te stanowią dogodny model do określenia, w jaki sposób upakowanie krystaliczne i specyficzne kontakty międzycząsteczkowe wpływają na barierę oraz mechanizm rotacji.

Ponadto dzięki obecności dwóch łańcuchów alkilowych przyłączonych do rdzenia, badane przeze mnie molekuły charakteryzują się również dosyć dobrą zdolnością do tworzenia fazy

szklistej. W połączeniu z wydłużonym kształtem molekuł stwarza to możliwość badania wpływu anizotropii oraz orientacji momentu dipolowego cząsteczek cieczy szkłotwórczych na ich relaksację strukturalną. Dzięki precyzyjnemu umiejscowieniu polarnego podstawnika możliwe jest selektywne próbkowanie reorientacji molekularnej względem wybranych osi molekuły, tj. osi długiej i/lub krótkiej.

Przedstawione zagadnienia pokazują, że dynamika molekularna w układach uporządkowanych i amorficznych jest kontrolowana przez właściwości budowy chemicznej cząsteczki, jej lokalne otoczenie oraz charakter oddziaływań międzycząsteczkowych. W przypadku kryształów amfidynamicznych szczególnie istotne jest określenie, w jaki sposób sieć krystaliczna, zwykle utożsamiana z ograniczeniem ruchu, może jednocześnie umożliwiać i modyfikować lokalną rotację wybranych fragmentów molekuły. Z kolei w fazach cieczy przechłodzonej i szklistej analiza procesów relaksacyjnych pozwala powiązać architekturę cząsteczki oraz orientację momentu dipolowego z charakterem relaksacji strukturalnej i drugorzędowej. Szerokopasmowa spektroskopia dielektryczna, dzięki swojej czułości na fluktuacje momentu dipolowego oraz szerokiemu oknu częstotliwościowemu, stanowi szczególnie użyteczne narzędzie do badania obu tych problemów.

Celem niniejszej rozprawy doktorskiej pt. „Obraz dynamiki reorientacyjnej dużych i anizotropowych molekuł w stanie krystalicznym i amorficznym na podstawie badań spektroskopią dielektryczną” było:

- określenie wpływu miejsca podstawienia atomu fluoru w rotorze fenylowym na wysokość bariery rotacji i charakter odpowiedzi dielektrycznej w krysztale amfidynamicznym
- zbadanie wpływu sposobu upakowania cząsteczek w różnych odmianach krystalicznych na wartość energii aktywacji dla wewnętrznej rotacji
- ustalenie, w jaki sposób kształt cząsteczki oraz orientacja momentu dipolowego względem osi molekularnych wpływają na kształt procesu relaksacji strukturalnej w stanie cieczy przechłodzonej

Wyniki moich badań zostały opublikowane w uznanych czasopismach naukowych jako ciąg tematycznie spójnych artykułów naukowych, które stanowią niniejszą rozprawę doktorską:

A1. M. Rams-Baron, A. Błażytko, K. Jurkiewicz, P. Lodowski, M. Książek, J. Kusz, W. Mozga, M. Fordymacka, M. Teymouri, J. Krzywik & M. Paluch. Image of the solid-state rotary motion encoded in the dielectric response. Reports on Progress in Physics. 87, 108002 (2024), DOI: 10.1088/1361-6633/ad7288. (MNiSW: 200 p., IF: 20,7)

A2. A. Błażytko, M. Rams-Baron, M. Książek, J. Kusz, M. Matussek, J. Grelska & M. Paluch. Engineering of Rotational Dynamics via Polymorph Manipulation. The Journal of Physical Chemistry A, 128, 50 (2024). DOI: 10.1021/acs.jpca.4c04964. (MNiSW: 100 p., IF: 2,7)

A3. A. Błażytko, M. Rams-Baron & M. Paluch. The influence of molecular shape on reorientation dynamics of sizable glass-forming isomers at ambient and elevated pressure. Scientific Reports, 14, 887 (2024). DOI: 10.1038/s41598-023-50894-8. (MNiSW: 140 p., IF: 4,1)

Uzupełnieniem dorobku naukowego związanego z realizacją doktoratu są również publikacje, które nie zostały włączone do cyklu stanowiącego podstawę niniejszej rozprawy doktorskiej:

B1. M. Rams-Baron, A. Błażytko, M. Książek, J. Kusz & M. Paluch. Internal Secondary Relaxation as a Dielectric Probe of Molecular Surroundings. The Journal of Physical Chemistry Letters, 15, 9, 2595–2600 (2024). DOI: 10.1021/acs.jpclett.4c00128. (MNiSW: 200 p., IF: 4,9)

B2. M. Rams-Baron, A. Błażytko, R. Casalini & M. Paluch. Insight into properties of sizable glass former from volumetric measurements. Journal of Chemical Physics B. 161 (6): 064502 (2024). DOI: 10.1063/5.0217660 (MNiSW: 100 p., IF: 2.9)

B3. J. Grelska, K. Grzybowska, A. Błażytko, K. Jurkiewicz & S. Pawlus. Temperature dependence of structural evolution and fragility of glass-forming monohydroxy alcohols. Journal of Molecular Liquids, 414 (2024). DOI: 10.1016/j.molliq.2024.126206. (MNiSW: 100 p., IF: 5,8)

B4. M. Rams-Baron, A. Błażytko, M. Matussek, P. Lodowski, A. Radoń & M. Paluch. Onset and Morphological Evolution of Cooperativity in Glass-Forming Liquids Composed of Anisotropically Shaped Molecules. The Journal of Physical Chemistry Letters. 16, 31 (2025). DOI: 10.1021/acs.jpclett.5c01863. (MNiSW: 200 p., IF: 4,9)

B5. M. Rams-Baron, A. Błażytko, R. Casalini & M. Paluch. Resolving the Arrhenius Paradox by Isochoric Analysys of Rotational Barriers in Molecular Glasses. Physical Review Letters. 136 (18), 188202 (2026). DOI: 10.1103/jpnz-xfbj. (MNiSW: 200 p., IF: 8,5)

Wyniki swoich badań prezentowałem również na niżej wymienionych międzynarodowych konferencjach naukowych:

C1. YoungMultis 2023, wystąpienie ustne: „Reorientation dynamics of structural isomers of sizeable glass-forming liquids revealed in dielectric studies at ambient and elevated pressure". Kraków, 2023

C2. 12th Conference on Broadband Dielectric Spectroscopy and its Applications, prezentacja plakatu: „Unusual secondary relaxation in the glass-forming molecular rotors". Lizbona, 2024 (plakat wyróżniony)

C3. 3d-ICOMAS, wystąpienie ustne: „Tuning rotational dynamics of molecular rotors through crystal structure manipulation". Werona, 2025

2. Omówienie artykułów naukowych

2.1 Analiza wpływu otoczenia molekularnego na parametry rotacji wewnętrznej za pomocą spektroskopii dielektrycznej

W pracy A1 wykazano, że szerokopasmowa spektroskopia dielektryczna stanowi wyjątkowo użyteczne narzędzie do badania rotacji molekularnej w układach zawierających polarne rotory. Opracowana została cała metodologia umożliwiająca powiązanie makroskopowej odpowiedzi dielektrycznej z mikroskopowymi właściwościami rotacji w krysztale amfidynamicznym. Pozwoliła ona uzyskać informacje nie tylko o czasie relaksacji i wysokości bariery rotacji, ale także o charakterze oddziaływań rotora z sąsiednimi molekułami.

W badaniach wykorzystano serię pokrewnych molekuł zbudowanych z dużego, słabo polarnego statora oraz małego polarnego rotora fenylowego połączonego ze szkieletem mostkiem acetylenowym (C-C≡C-C). Jako rotujące jednostki zastosowano: 2-fluorofenylen, 3-fluorofenylen, 2,3-difluorofenylowy oraz niepolarny fenylen, oznaczone odpowiednio jako M-ortho-F, M-meta-F, M-2F oraz M-Ph [A1 rysunek 1]. Tak zaprojektowany zestaw molekuł umożliwił porównanie wpływu położenia i liczby atomów fluoru na dynamikę rotacyjną przy zachowaniu bardzo zbliżonej architektury statora.

Dla wszystkich polarnych związków zaobserwowano wyraźne maksimum strat dielektrycznych przypisane reorientacji fragmentu fluorofenylowego. Szczególnie wyróżniał się układ M-meta-F, dla którego stwierdzono najszybszą rotację i najniższą barierę aktywacji. Wyznaczone energie aktywacji wyniosły 6,06 ± 0,03 kcal/mol (25,36 ± 0,13 kJ/mol) dla M-meta-F, 9,57 ± 0,03 kcal/mol (40,03 ± 0,13 kJ/mol) dla M-2F oraz 11,84 ± 0,06 kcal/mol (49,54 ± 0,25 kJ/mol) dla M-ortho-F [A1 tabela 1]. Dla M-meta-F zaobserwowano ponadto odmienny przebieg zmian amplitudy maksimum strat dielektrycznych wraz z temperaturą - przy obniżaniu temperatury amplituda rosła, podczas gdy dla dwóch pozostałych rotorów malała [A1 rysunek 2a, b, c]. Oznaczało to, że badane układy reprezentują dwa różne wzorce odpowiedzi dielektrycznej, odpowiadające dwóm różnym typom krajobrazu potencjału rotacyjnego. Do interpretacji tych wyników zastosowano model asymetrycznej podwójnej jamy potencjału (ADWP – ang. *asymmetric double-well potential*). Analiza wykazała, że rotacja w M-meta-F zachodzi w potencjale niemal symetrycznym, dla którego parametr asymetrii Δ przyjmuje wartość 0,51 ± 0,01 kcal/mol (2,13 ± 0,04 kJ/mol), natomiast

dla M-2F i M-ortho-F potencjał jest wyraźnie bardziej asymetryczny, a wartości parametru Δ wynoszą odpowiednio 1,38 ± 0,02 kcal/mol (5,77 ± 0,08 kJ/mol) oraz 1,70 ± 0,06 kcal/mol (7,11 ± 0,25 kJ/mol) [A1 tabela 2]. Uzyskano więc spójny obraz, w którym niskiej barierze rotacji odpowiada potencjał bliski symetrycznemu, natomiast wyższe bariery związane są z większą nierównoważnością energetyczną dostępnych orientacji. W konsekwencji wykazano, że sama ewolucja amplitudy procesu dielektrycznego może stanowić wskaźnik asymetrii potencjału rotacyjnego.

Istotnym elementem pracy było również porównanie zachowania tych samych układów w stanie szklistym. Po zeszkleniu obserwowane w krysztale różnice uległy znacznemu zatarciu. Energie aktywacji procesu β, przypisanego rotacji fluorofenylenu, stały się bardzo zbliżone i wyniosły 12,37 ± 0,16 kcal/mol (51,76 ± 0,67 kJ/mol) dla M-ortho-F, 11,58 ± 0,21 kcal/mol (48,45 ± 0,88 kJ/mol) dla M-meta-F oraz 11,40 ± 0,17 kcal/mol (47,70 ± 0,71 kJ/mol) dla M-2F [A1 tabela 1]. Również parametry asymetrii potencjału z modelu ADWP okazały się podobne dla wszystkich trzech rotorów. Wynik ten miał zasadnicze znaczenie interpretacyjne, ponieważ wskazał, że różnice obserwowane w stanie krystalicznym nie wynikają wyłącznie z budowy chemicznej samego rotora, lecz przede wszystkim z uporządkowanego środowiska krystalicznego i z obecnych w nim specyficznych oddziaływań międzycząsteczkowych.

Badania strukturalne umożliwiły bezpośrednie powiązanie właściwości dynamicznych z typem kontaktów międzycząsteczkowych. Wykazano, że w krysztale M-meta-F preferowane są kontakty rotor-rotor, a taka organizacja sprzyja bardziej niezależnej i niskobarierowej rotacji. Dla M-ortho-F obecne są natomiast kontakty rotor-stator, które zwiększają barierę ruchu i prowadzą do wzrostu asymetrii potencjału, natomiast w M-2F współistnieją oba typy oddziaływań [A1 rysunek 4]. Otrzymany obraz strukturalny dostarczył zatem molekularnego uzasadnienia dla dwóch zidentyfikowanych wzorców odpowiedzi dielektrycznej.

2.2 Modyfikacja dynamiki rotacji poprzez manipulację strukturą krystaliczną

W pracy A2 podjęto zagadnienie wpływu polimorfizmu krystalicznego na dynamikę rotacji w kryształach amfidynamicznych. Punktem wyjścia było założenie, że właściwości rotacyjne nie muszą być kształtowane wyłącznie przez projektowanie nowych struktur chemicznych, lecz mogą być również modulowane poprzez zmianę sposobu upakowania tych

samych cząsteczek w sieci krystalicznej. Celem badań było więc ustalenie, w jakim stopniu niewielkie zmiany geometrii upakowania w różnych polimorfach jednego związku wpływają na wysokość bariery rotacji fluorofenylowego rotora. Tym samym praca stanowiła próbę wykazania, że polimorfizm może zostać wykorzystany jako narzędzie inżynierii rotacji molekularnej w ciele stałym.

W badaniach wykorzystano dwa zaprojektowane wcześniej układy amfidynamiczne zawierające duży, sztywny i słabo polarny stator oraz rotor fluorofenylowy połączony ze szkieletem pojedynczym wiązaniem C-C. Analizie poddano dwa izomery: M-meta-F, zawierający rotor 3-fluorofenylowy, oraz M-ortho-F, zawierający rotor 2-fluorofenylowy. W odróżnieniu od wcześniejszych molekuł opartych na mostku acetylenowym (wykorzystanych w pracy A1), w tej pracy zastosowano pojedyncze wiązanie łączące rotor ze statorem, co obniżyło swobodę ruchu, lecz umożliwiło uzyskanie różnych form polimorficznych.

W pierwszym etapie wykazano, że oba badane związki przechodzą w stan szklisty i charakteryzują się identyczną temperaturą zeszklenia równą $T_g = 313 \pm 1$ K [A2 rysunek 1a]. Następnie, poprzez zastosowanie dwóch odmiennych protokołów rekrystalizacji z cieczy przechłodzonej, uzyskano różne polimorfy obu izomerów, co potwierdzono dzięki badaniom za pomocą skaningowej kalorymetrii różnicowej (DSC – ang. *differential scanning calorimetry*) oraz dyfrakcji rentgenowskiej (XRD – ang. *X-Ray diffraction*) [A2 rysunek 2].

W stanie szklistym energie aktywacji procesu β były do siebie zbliżone i wyniosły 45,20 ± 0,72 kJ/mol dla M-meta-F oraz 47,1 ± 0,58 kJ/mol dla M-ortho-F. W stanie krystalicznym różnice okazały się jednak bardzo duże. Dla M-meta-F po rekrystalizacji z użyciem ścieżki I otrzymano polimorf 1a charakteryzujący się barierą rotacji w wysokości 83,32 ± 0,65 kJ/mol. Natomiast po rekrystalizacji z użyciem ścieżki II zidentyfikowano dwa procesy relaksacyjne: wolniejszy, którego energia aktywacji wynosi 85,00 ± 0,42 kJ/mol oraz szybszy i dominujący o barierze wynoszącej 58,26 ± 0,08 kJ/mol. Dzięki dodatkowym badaniom przy pomocy DSC oraz XRD stwierdzono, że po ścieżce II otrzymano mieszaninę dwóch odmian krystalicznych: polimorfa 1a oraz polimorfa 2a. Dla M-ortho-F polimorf 1b charakteryzował się barierą 86,47 ± 0,08 kJ/mol, podczas gdy dla polimorfu 2b uzyskano znacznie wyższą wartość 128,49 ± 2,66 kJ/mol [A2 rysunek 3]. Oznacza to, że sama reorganizacja molekuł w krysztale prowadziła do bardzo wyraźnej zmiany dynamiki rotacji.

Analiza strukturalna dostarczyła molekularnego uzasadnienia tych różnic, gdyż wykazano, że podstawowym czynnikiem determinującym wysokość bariery rotacji jest liczba i geometria kontaktów typu C-H···F pomiędzy rotorem a jego otoczeniem. W przypadku M-

meta-F słabsze i rzadsze oddziaływania rotor-stator (polimorf 2a) sprzyjają niższej barierze, natomiast obecność zarówno kontaktów rotor-rotor, jak i rotor–stator (polimorf 1a) prowadzi do jej wzrostu. Dla M-ortho-F, ze względu na geometrię fluorofenylowego fragmentu, dominują silniejsze oddziaływania rotor-stator, w tym również kontakty wewnątrzcząsteczkowe, co skutkuje najwyższymi barierami rotacji, szczególnie w polimorfie 2b [A2 rysunek 4].

Te nowatorskie wyniki wskazują, że polimorfizm może pełnić funkcję narzędzia kontroli dynamiki molekularnej w kryształach amfidynamicznych. W przeciwieństwie do klasycznego podejścia, opartego na modyfikacji chemicznej rotora lub statora, zaprezentowane wyniki pokazują, że porównywalny efekt dynamiczny można uzyskać poprzez zmianę organizacji tych samych cząsteczek w sieci krystalicznej.

2.3 Znaczenie kształtu cząsteczki i orientacji momentu dipolowego w dynamice cieczy szkłotwórczych

Trzecia praca rozszerza analizę dynamiki rotacyjnej z lokalnej reorientacji fragmentu molekularnego w fazie krystalicznej na reorientację całych anizotropowych cząsteczek w stanie cieczy przechłodzonej. Celem artykułu A3 było określenie, w jaki sposób zmiana położenia grupy trifluorometylowej, prowadząca do modyfikacji geometrii molekuły oraz kierunku wektora momentu dipolowego, wpływa na relaksację strukturalną oraz kooperatywny charakter dynamiki molekularnej. Przedmiotem badań były trzy izomery strukturalne oznaczone jako ortho-CF_3, meta-CF_3 oraz para-CF_3 [A3 rysunek 1]. Tak zaprojektowana seria związków pozwoliła wyeliminować wpływ masy i składu chemicznego, a tym samym bezpośrednio ocenić znaczenie geometrii cząsteczki oraz orientacji momentu dipolowego dla dynamiki molekularnej.

W pierwszym etapie przeprowadzono charakterystykę termiczną badanych układów z wykorzystaniem różnicowej kalorymetrii skaningowej. Wykazano, że pomimo identycznego składu chemicznego badane izomery różnią się temperaturą topnienia, temperaturą zeszklenia oraz zdolnością do rekrystalizacji ze stanu amorficznego [A3 rysunek 2].

Zasadniczą część pracy stanowiła analiza widm szerokopasmowej spektroskopii dielektrycznej w stanie cieczy przechłodzonej. Dla wszystkich izomerów zaobserwowano proces relaksacji strukturalnej, który jest związany z reorientacją całych cząsteczek [A3 rysunek 3]. Stwierdzono jednak, że kształt maksimum strat dielektrycznych jest silnie

zależny od położenia grupy -CF_3 oraz od względnych wartości podłużnej i poprzecznej składowej momentu dipolowego. W przypadku izomeru para-CF_3, dla którego moment dipolowy jest zorientowany niemal równolegle do długiej osi molekuły, widmo relaksacyjne charakteryzowało się najwęższym maksimum strat dielektrycznych (β_{KWW} = 0,71). Odmienny charakter odpowiedzi dielektrycznej zaobserwowano dla izomeru meta-CF_3. W wysokich temperaturach relaksacja strukturalna tego związku miała charakter bimodalny, co zinterpretowano jako przejaw rozdzielenia czasów relaksacji względem długiej i krótkiej osi molekularnej. Wynik ten miał kluczowe znaczenie, ponieważ wykazał, że możliwym jest obserwować przy pomocy spektroskopii dielektrycznej poszczególne składowe ruchu wokół różnych osi molekularnych. W pobliżu przejścia szklistego oba procesy relaksacyjne uległy stopniowemu scaleniu w jedno maksimum strat dielektrycznych, którego wartość parametru β_{KWW} wynosi 0,58. W przypadku izomeru ortho-CF_3 nie zaobserwowano tak wyraźnego rozdzielenia procesów relaksacyjnych, jednak poszerzenie α-relaksacji wskazywało na udział więcej niż jednej składowej reorientacyjnej (β_{KWW} = 0,51) [A3 rysunek 4].

Uzupełnieniem badań prowadzonych w ciśnieniu atmosferycznym były pomiary dielektryczne w warunkach podwyższonego ciśnienia. Wykazano, że wszystkie badane układy charakteryzują się bardzo dużą wrażliwością temperatury zeszklenia na ciśnienie. Wartości współczynnika dT_g/dP wynosiły 0,387 K/MPa dla para-CF_3, 0,332 K/MPa dla meta-CF_3 oraz 0,326 K/MPa dla ortho-CF_3 [A3 rysunek 7]. Na podstawie danych wysokociśnieniowych wyznaczono również objętości aktywacji w temperaturze zeszklenia. Otrzymane wartości wynosiły 735 cm^3/mol dla para-CF_3, 648 cm^3/mol dla meta-CF_3 oraz 624 cm^3/mol dla ortho-CF_3. Szczególnie wysoka wartość uzyskana dla para-CF_3 wskazuje, że większe wydłużenie cząsteczki prowadzi do wzrostu objętości niezbędnej do realizacji kooperatywnej reorientacji.
W końcowej części pracy określono stopień kooperatywności dynamiki w pobliżu temperatury zeszklenia, wykorzystując podejście Dontha oparte na analizie danych uzyskanych przy użyciu temperaturowo modulowanego DSC [A3 rysunek 10]. Liczba dynamicznie skorelowanych cząsteczek wynosiła 55 dla para-CF_3, 44 dla meta-CF_3 oraz 35 dla ortho-CF_3. Wartości te są niższe niż typowo obserwowane dla wielu klasycznych cieczy szkłotwórczych, co powiązano z dużym rozmiarem badanych molekuł. Dodatkowo przeanalizowano zależność pomiędzy objętością aktywacji a promieniem korelacji, charakteryzującym przestrzenny zasięg kooperatywnej dynamiki w pobliżu temperatury zeszklenia [A3 rysunek 11]. Porównanie uzyskanych w tej pracy wyników z zaproponowaną korelacją wykazało, że badane izomery rozszerzają zakres jej stosowalności na skrajne przypadki dużych molekuł szkłotwórczych.

Mimo że analizowane układy charakteryzują się szczególnie dużymi wartościami objętości aktywacji, ich zachowanie pozostaje zgodne z liniową zależnością wyznaczoną wcześniej dla innych klas cieczy szkłotwórczych.

3. Wykaz publikacji stanowiących podstawę rozprawy doktorskiej wraz z materiałami uzupełniającymi i oświadczeniami autorów

3.1 Artykuł A1

A1. M. Rams-Baron, A. Błażytko, K. Jurkiewicz, P. Lodowski, M. Książek, J. Kusz, W. Mozga, M. Fordymacka, M. Teymouri, J. Krzywik & M. Paluch. Image of the solid-state rotary motion encoded in the dielectric response. Reports on Progress in Physics. 87, 108002 (2024)

Impact Factor z roku opublikowania: 20.7

Punkty ministerialne: 200

DOI: 10.1088/1361-6633/ad7288

Mój wkład do tego artykułu polegał na zaplanowaniu i przeprowadzeniu części eksperymentów za pomocą spektroskopii dielektrycznej oraz skaningowej kalorymetrii różnicowej. Oświadczenia o wkładzie pozostałych współautorów zostały zamieszczone w podrozdziale 3.4.

OPEN ACCESS
IOP Publishing
Reports on Progress in Physics
Rep. Prog. Phys. 87 (2024) 108002 (12pp)
https://doi.org/10.1088/1361-6633/ad7288

Image of the solid-state rotary motion encoded in the dielectric response

Marzena Rams-Baron[1,*], Alfred Błażytko[1], Karolina Jurkiewicz[1], Piotr Lodowski[2], Maria Książek[1], Joachim Kusz[1], Witold Mozga[3], Marta Fordymacka[3], Mahshid Teymouri[3], Julia Krzywik[3] and Marian Paluch[1]

[1] August Chełkowski Institute of Physics, University of Silesia in Katowice, 75 Pulku Piechoty 1, 41-500 Chorzow, Poland
[2] Institute of Chemistry, University of Silesia in Katowice, Szkolna 9, 40-006 Katowice, Poland
[3] TriMen Chemicals Sp. z o.o., Al, Piłsudskiego 141, 92-318 Łódź, Poland

E-mail: marzena.rams-baron@us.edu.pl

Received 23 December 2023, revised 22 July 2024
Accepted for publication 22 August 2024
Published 10 September 2024

Corresponding editor: Dr Paul Mabey

Abstract
The future development of advanced molecular systems with controlled rotation requires the development of an effective methodology for assessing the rotational performance of artificial machine components. We identified two patterns of the dielectric behavior for polar rotators in a static non-polar framework of sizable crystal showing relations between the spectral and molecular-level features of solid-state rotary motion. Various functionalization of phenylene rotors with a fluorine atom(s) changed rotational performance from high to low with rotational barriers ranging from 6.06 to 11.84 kcal mol^{-1}. The meta-F-substitution favored rotator-rotator contacts allowing for the implementation of fast rotary motion. Contrary, the presence of rotator-stator contacts inhibited independent rotator dynamics leading to opposite spectral behavior in terms of temperature evolution of loss peak amplitude. Our observations, supported by an analysis based on an asymmetric double well-potential model, show that easily noticeable spectral differences encoded some molecular-level information important for the implementation of rotary motion.

Supplementary material for this article is available online

Keywords: dielectric spectroscopy, polar rotor, internal rotation, solid-state dynamics

1. Introduction

Referring to Einstein's theory of Brownian motion [1], in 1913 P. Debye gave the first description of the rotational motion in a polar molecule to understand the dielectric behavior of polar liquids [2, 3]. More than 100 years after the Debye theory, which approximated the molecule as a sphere and completely ignored intermolecular contributions, our understanding of the importance of intermolecular effects on the dielectric response has greatly increased. The knowledge accumulated over the years of study on glasses, polymers, liquid crystals, etc. provides us a picture of how various molecular features (e.g. molecular order, presence of H–bond network) may affect the dielectric response. Now we can transpose this knowledge to create such a picture for the rotators actively rotating in the crystalline interior.

We are witnessing enormous progress in creating potential components of intelligent materials and molecular machines [4–6]. Most of the work to date has focused on developing

* Author to whom any correspondence should be addressed.

perspective synthetic strategies that bring to life a multi-year vision of artificial molecular systems responsive to external stimuli and capable of controlled movement [7–12]. The attention attracts a group of crystalline materials with remarkable dynamical behavior called 'amphidynamic crystals' with mobile molecular units embedded in the static crystalline framework [8, 13–21]. Designing their controlled and tunable rotary motion is the ultimate goal of ongoing research [5]. The application of nuclear magnetic resonance to study the rotator's solid-state dynamics was a routine practice in the field [14, 22]. Recently, we have witnessed the growing interest in the dielectric evaluation of rotator dynamics [11, 17, 23–28], which is associated with an urgent need for research into dipolar rotators that have demonstrated potential as stimuli-responsive components of molecular machinery [24, 29–31].

Dielectric measurements can support the development of new components of artificial molecular machines well beyond assessing time scales and barriers associated with internal rotation. Careful analysis of the dielectric spectra, which account for the molecular structure, can provide information important from the implementation of the rotary motion. The sooner we begin to use the full potential of dielectric research for a holistic view of the solid-state rotator dynamics, taking into account the structure of the material, the better we will understand the structure-dynamics-function relationships, which will bring us closer to the goal of realizing controlled and correlated motion capable to perform useful tasks. Here we take a step in this direction by showing different patterns of dielectric response and combining these spectral features with molecular aspects of rotational motion resulting from the molecular structure of investigated crystals.

BDS is a versatile tool that provides insight into the dynamic of molecules on many scales—from independent movements of molecular subunits to collective rearrangements of whole molecules. The BDS method is ideal for studying rotary motion in solid polar materials in widely varying frequencies, temperatures, and pressures. Structural changes related to phase transitions or the emergence of dipolar order will be also reflected in the dielectric response [26]. Polar groups act as intrinsic motion probes, being the source of a dipole moment that changes orientation when an external electric field is applied. The change of dipole moment is the only condition for dielectric detection of any dynamic phenomenon [32].

Our principal goal was to study the solid-state dynamics of three polar rotators to understand how molecular-level properties impact the rotator dynamics probed by the BDS method. To realize that we synthesized systems with a sizable core (stator) containing diphenylamine and fluorene motifs functionalized with flexible alkyl chains (figure 1(a)). The sizable framework with a small dipole moment of 0.49 Debye (D) was linked via an acetylene bridge to a small polar rotator. Due to favorable molecular packing in a crystalline state, and the presence of bulky and protruding elements of the stator, the rotating units have enough free space to realize rotary motion in a crystalline state. The rotating part was 2-fluorophenyl (assigned as M-*ortho*-F), 3-fluorophenyl (M-*meta*-F), or 2, 3-difluorophenyl (M-2F). For comparative purposes, a non-polar derivative, with the rotating unit lacking polar substituent (M-Ph), was also synthesized. The description of synthetic protocols and materials characterization are included in sections 1.1 and 1.2 in supplementary methods and supplementary figures S1–S15. In the designed systems a dipole moment was carried out by a fluorine atom which imparts a large permanent electric dipole moment of 1.6 D to the rotating unit. The small size of the F atom, whose van der Waals radius of 0.14 nm is only slightly larger than the H radius of 0.12 nm, allowed us to realize the assumption about the minimal steric impact of the probe on the performance of the detected rotation [33]. The dipole moment acts as a probe, but at the same time, through dipole–dipole interactions, it affects the potential around the rotating unit. By changing the number and position of fluorine atoms in the phenylene unit we create systems with different magnitudes and directions of the effective dipole moment as depicted in figure 1(b). We demonstrated here that variations in fluorine atom position within the rotating unit notably affected the rotational behavior observed in crystals and probed using the BDS method. We identified two patterns of dielectric response with various temperature evolution of loss peak amplitude which correlated with rotational performance. DFT simulations and single crystal structural analysis helped interpret the dynamics in the context of the molecular-level justification of the discovered behavior. It is an important step in building our intuition for the effective evaluation of rotator properties by the dielectric method.

2. Results and discussion

2.1. The dielectric response of rotators in the crystalline interior

For all crystals, the frequency-dependence of the imaginary part of complex dielectric permittivity $\varepsilon''(f)$ shown in figures 2(a)–(c) revealed a well-pronounced loss peak at a specific frequency providing evidence of the dipolar relaxation (see figure S20 in supplementary data file for $\varepsilon'(f)$ data). This feature was attributed to the dipolar rotation of fluorphenylene or difluorphenylene unit in a crystalline framework of a sizable molecule. Its timescale was defined by the position of the loss peak maximum, $f_{\max}$ as $\tau = 1/2\pi f_{\max,}$ where τ is an internal rotation relaxation time. The observed peak shifting on heating toward a high frequency (i.e., shorter τ) manifests the acceleration of rotary motion. Figure 2(g) compares the dielectric response of a non-fluorinated M-Ph derivative and M-meta-F at 223 K. The absence of a relaxation process in the dielectric response of the non-polar counterpart confirms that the dipolar rotation of the phenylene unit is the source of the prominent relaxation process visible in figures 2(a)–(c).

The inspection of dielectric data presented in figure 2(b) revealed an intriguing feature related to the distinct pattern of dielectric behavior in M-*meta*-F. At 173 K, the rotational frequency for M-*meta*-F is $f_{\max} = 0.8$ kHz. At the same time, for other rotators, it is almost three decades smaller (for M-*ortho*-F $f_{\max}$ at 173 K is out of the experimental window), indicating

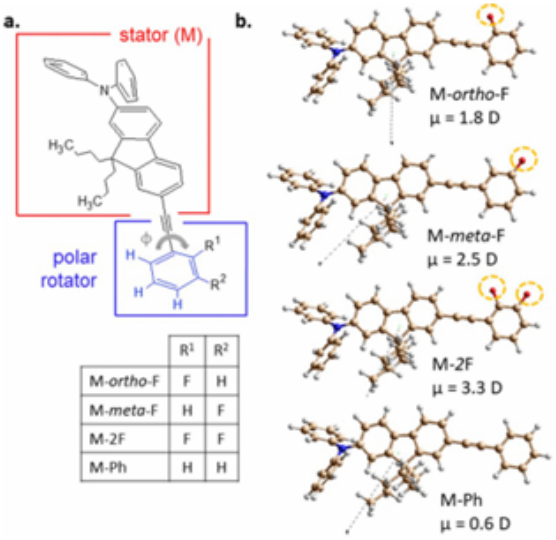

	R¹	R²
M-*ortho*-F	F	H
M-*meta*-F	H	F
M-2F	F	F
M-Ph	H	H

Figure 1. (a) Structural elements of a sizable molecule with a polar rotator. The common stator (black) contains phenylamine and fluorene units functionalized with flexible alkyl chains. The attachment of alkyl chains, increasing the bulkiness, and reducing the planarity of a molecule is a common strategy to suppress crystallization during the vitrification process. The sizable framework provided the necessary free volume to support a rotational motion of the phenylene unit (blue) variously substituted with F. For comparative purposes, a non-polar derivative was also investigated. (b) Ball and stick model of sizable rotators obtained for DFT geometry optimized structures with the indicated direction of an effective dipole moment (color code: F atom shown in red, N in blue, C in brown, H in white).

the favorable rotational performance of M-*meta*-F. The second striking feature is the opposite character of the temperature evolution of the peak amplitude in M-*meta*-F. To get more details, first, we quantitatively analyzed the dielectric data with the Debye and Cole–Cole (CC) models, both compared in figure 2(f). Both models provide almost identical relaxation time values. Still, the CC function better-described data in a low-temperature region where the loss peak broadened noticeably. Such behavior could be accounted for by the CC model and the decreasing value of the α parameter (see supplementary figure S21). The broadening of the loss peak is a typical feature of the dielectric response of supercooled liquids, considered a hallmark of dynamic heterogeneity [34]. In some structurally ordered systems, e.g., rotators embedded in MOF frameworks, such effect was also observed and explained by variations in rotator environments due to the presence of other dipoles [26] or to temperature-dependent mobility of MOF framework [23]. For M-2F, parameter α varies from 0.93 to 0.81, M-ortho-F from 0.99 to 0.90, and M-*meta*-F from 0.97 to 0.94. An intuitive explanation for such behavior may be considering it as a natural consequence of the discrete distribution of local free energy barriers in crystalline rotators. In a high-temperature limit, the relaxations corresponding to the sites of different energy merge into a single relaxation process. At lower temperatures, the site-dependent differences in relaxation rates gained more importance, leading to peak broadening. Notably, the symmetric peak broadening on cooling was the weakest for M-*meta*-F, i.e., the system with the lowest rotational barrier, as shown later. The smaller differences in the depth of potential wells expected for this sample lead to a smaller distribution in jump probabilities and are consistent with the experimentally observed narrower loss peak for M-*meta*-F.

The temperature dependence of τ is presented in the upper panel of figure 2(e). Table S1 summarizing the variable temperature data (T and τ values for all experiments) is given in the supplementary material. Relaxation times underlying the rotation of phenylene units in crystalline interior follow a thermally activated Arrhenius behavior:

$$\tau = \tau_0 \exp\left(\frac{E_a}{kT}\right)$$

where E_a is the activation energy, τ_0 is the pre-exponential factor, and k_B is a Boltzmann constant. For investigated rotators, τ_0, related to the attempt frequency at which the molecule tries to overcome the rotational barrier in a given environment [18] takes values from $4.27{\cdot}10^{-12}$ s to $1.38{\cdot}10^{-15}$ s (see table 1).

The most important outcome of the analysis was that activation energy for M-meta-F was significantly lower compared to other rotators. The found values were $E_a = 6.06 \pm 0.03$ kcal mol^{-1} for M-*meta*-F and much higher values for M-*ortho*-F ($E_a = 11.84 \pm 0.06$ kcal mol^{-1}) and M-2F ($E_a = 9.57 \pm 0.03$ kcal mol^{-1}). It is remarkable that identified differences in dielectric response correlate with rotational efficiency. A distinct behavior was found for M-*meta*-F, i.e., for the rotator with the lowest rotational barrier. Figures 2(a)–(c) proves that ε''_{max} (T) behavior of M-*meta*-F strongly deviates from two other rotators. For M-*ortho*-F and M-2F, the amplitude of the loss peak decreases on cooling. In contrast, for M-*meta*-F, the opposite behavior was identified. The observed character of amplitude changes found for M-ortho-F and M-2F could be treated as a manifestation of antiferroelectric ordering in these two materials [26]. In our research, however, we did not find any hallmark of order-disorder transition in M-*ortho*-F and M-2F, such as a step change in the temperature evolution of dielectric parameters $\Delta\varepsilon$ or τ, or any anomaly detected in the DSC scans indicating the presence of phase transition (see supplementary figure S22). On the contrary, all analyzed parameters were evolving quite systematically for all three rotators in the investigated T-range. To explain the behavior of M-*ortho*-F and M-2F and the distinctive behavior of M-*meta*-F we used a model of dipole reorienting in an asymmetric double-well potential (ADWP). According to the ADWP model, the variations in the rotator's surroundings can impact the potential and lead to its asymmetry. Taking into account the wells asymmetry Δ and the energy barrier U, the relaxation time τ and the maximum loss ε''_{max} according to ADWP is given by [35, 36]:

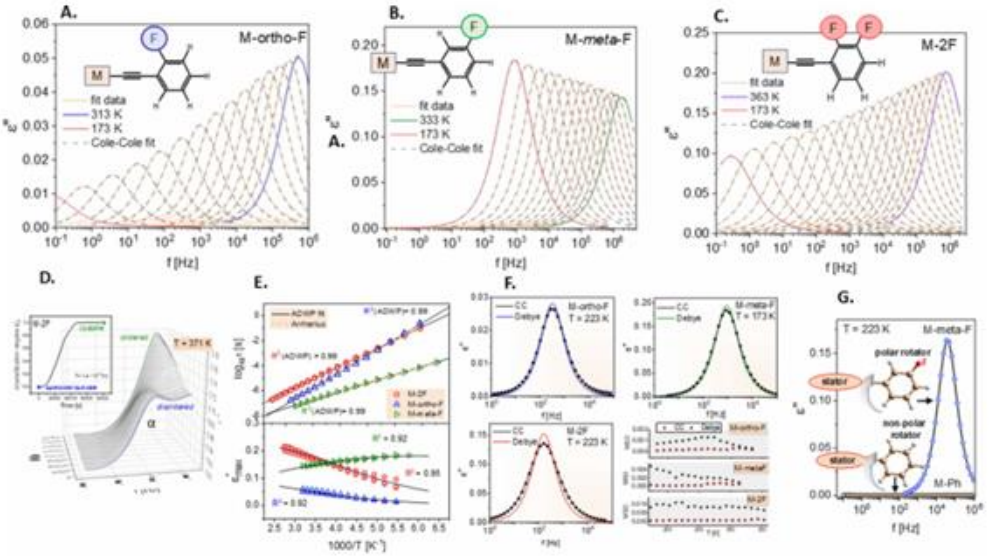

Figure 2. Rotational behavior of phenylene rotators in sizable molecules in the crystalline state. (a)–(c) Representative temperature-dependent dielectric loss spectra for the polar rotators in the crystalline state ($\Delta T = 10$ K). Notice a distinct relaxation behavior of M-*meta*-F. (d). Time-evolution of dielectric loss spectra during crystallization of M-2F sample, monitored *in situ* in dielectric apparatus. The progress of the liquid-crystal transformation was manifested as a gradual decrease of the α-process amplitude (due to the vanishing number of actively reorienting molecules) and the appearance of relaxation underlying the internal rotation of the phenylene unit. (e) Temperature dependence of the relaxation times (upper panel) and the loss peak maxima (bottom panel) extracted from dielectric data. Dashed lines denote Arrhenius fits while solid lines indicate fits obtained from the ADWP model with fitting parameters given in tables 1 and 2, respectively. (f) The comparison of the effectiveness of the Debye and Cole–Cole models in the description of experimental data. The mean square deviations in the y direction of each data point with the fitting function for different temperatures are given. (g) The comparison of dielectric response for polar (M-*meta*-F) and non-polar (M-Ph) rotator at 223 K. The rotation of the Ph-unit in M-Ph is dielectrically inactive due to the accompanying lack of dipole moment change.

Table 1. Activation parameters of rotational motion obtained from the Arrhenius fit (±standard errors). The value of activation energy was determined by taking into account relaxation times from three independent experiments. The error reflects the accuracy of the fit and scattering of experimental points.

	Crystalline state		Glassy state			
			β		γ	
	$\log_{10}\tau_0$ (s)	E_a (kcal mol^{-1})	$\log_{10}\tau_0$ (s)	E_a (kcal mol^{-1})	$\log_{10}\tau_0$ (s)	E_a (kcal mol^{-1})
M-*ortho*-F	-14.86 ± 0.05	11.84 ± 0.06	-17.68 ± 0.18	12.37 ± 0.16	-11.67 ± 0.30	5.46 ± 0.25
M-*meta*-F	-11.37 ± 0.03	6.06 ± 0.03	-17.14 ± 0.26	11.58 ± 0.21	-12.88 ± 0.10	6.30 ± 0.08
M-2F	-12.42 ± 0.03	9.57 ± 0.03	-15.36 ± 0.20	11.40 ± 0.17	-12.01 ± 0.13	6.06 ± 0.11
M-Ph					-12.00 ± 0.09	4.96 ± 0.07

$$\tau = \tau_0 \exp\left(\frac{2U+\Delta}{2kT}\right) \operatorname{sech}\left(\frac{\Delta}{2kT}\right)$$

$$\varepsilon''_{\max} = \frac{T_0}{T}\cosh^{-2}\left(\frac{\Delta}{2kT}\right)$$

where T_0, τ_0, U, and Δ are fitting parameters collected in table 2. The $\tau(T)$ and $\varepsilon''_{\max}(T)$ dependencies were acceptably fitted to the ADWP expressions (solid lines in figure 2(e)) with the following activation parameters: for M-*ortho*-F the lower potential barrier height $U = 11.90 \pm 0.06$ kcal mol^{-1}, and asymmetry parameter $\Delta = 1.70 \pm 0.06$ kcal mol^{-1}; for M-2F $U = 9.55 \pm 0.03$ kcal mol^{-1}, $\Delta = 1.38 \pm 0.02$ kcal mol^{-1}; for M-*meta*-F $U = 5.98 \pm 0.03$ kcal mol^{-1}, and $\Delta = 0.51 \pm 0.01$ kcal mol^{-1}. Both ADWP and Arrhenius models yielded consistent predictions leading to similar values of rotational barriers U and E_a. Data analysis in the framework of the ADWP model shows that in M-*meta*-F, the rotation occurs in an essentially symmetric double rotational potential well. In contrast, the two other systems are well-described by more asymmetric double well rotational potentials. Mentioned differences in potential symmetry can also explain the distinct evolution of peak amplitude. In the ADWP model, the maximal loss related to orientational polarization, in addition to the trivial $1/T$ dependence, is governed by the $\cosh^{-2}(\Delta/2kT)$ term. As temperature drops and kT decreases, the $\cosh^{-2}(\Delta/2kT)$ term decreases the polarization towards

Table 2. Fitting parameters (±standard errors referring to the precision of the fitted values and scattering of experimental points) obtained from analysis of $\varepsilon''_{max}(T)$ (or $\Delta\varepsilon$ for β-process in glass) and $\tau(T)$ data in the framework of an asymmetric double-well potential model (ADWP). Parameter U is the barrier height and Δ is an asymmetry parameter.

	ADWP model		
	M-*ortho*-F	M-*meta*-F	M-2F
	Crystal		
log τ_0 (s)	-15.13 ± 0.06	-11.43 ± 0.03	-12.62 ± 0.03
U (kcal mol^{-1})	11.90 ± 0.06	5.98 ± 0.03	9.55 ± 0.03
Δ (kcal mol^{-1})	1.70 ± 0.06	0.51 ± 0.01	1.38 ± 0.02
T_0 (K)	77.7 ± 7.4	52.2 ± 0.6	169.3 ± 5.0
	Glass		
log τ_0 (s)	-17.9 ± 0.2	-17.3 ± 0.3	-15.6 ± 0.2
U (kcal mol^{-1})	12.40 ± 0.16	11.61 ± 0.21	11.43 ± 0.17
Δ (kcal mol^{-1})	1.03 ± 0.02	0.95 ± 0.05	1.03 ± 0.02
T_0 (K)	172.8 ± 8.0	120.5 ± 15.1	365.9 ± 15.7

the applied field since rotators have insufficient thermal energy to overcome the intrinsic well asymmetry and jump to a higher well. Consequently, the rotators are trapped in the lower well at low T and do not respond to the field [37]. Such low-T freezing of active dipoles can rationalize the pattern of $\varepsilon''_{max}(T)$ changes observed for M-2F and M-*ortho*-F. The opposite behavior revealed for M-*meta*-F can be explained by the lowest value of potential asymmetry, which makes the term $\cosh^{-2}(\Delta/2kT)$ negligible. Note that the situation when $\Delta = 0$ corresponds to $\varepsilon''_{max} \sim T_0/T$, which is well-known for Curie behavior.

When the phenomenon of dielectric relaxation is viewed as a chemical reaction in which dipole reorientation from one equilibrium position to another occurs through a potential barrier height, the Eyring equation can be implemented to determine the following thermodynamic activation parameters: Gibbs free energy (ΔG), enthalpy (ΔH), and entropy (ΔS) [38–40]. The Eyring plots of ln (k/T) versus $1/T$, where $k = \tau^{-1}$ denotes the temperature-dependent dielectric relaxation rate, are shown in supplementary figure S23. The activation enthalpy and entropy were calculated as ΔH (kcal mol^{-1}) = −slope × R and ΔS (cal/(mol K)) = R (y-intercept−ln($k_B/\hbar$)) where R, k_B, and $\hbar$ are the gas, Boltzmann, and Plank's constants, respectively. The values of ΔS and ΔH determined from dielectric measurements are shown in table 3. Gibbs free energy was calculated subsequently at 273 K as $\Delta G = \Delta H — T\Delta S$.

From the data presented in table 3, one can see that ΔG and ΔH are the lowest for M-*meta*-F which is consistent with earlier results implementing Arrhenius and ADWP models. It is interesting that for M-*ortho*-F the activation entropy increases significantly (ΔS has a positive value) in comparison to other rotators. We interpret the variation in ΔS as reflecting various molecular packings and rotational freedoms for particular rotators leading to variation in the population of bound and unbound rotational states in particular environments. The

Table 3. The thermodynamic parameters ΔH, ΔS, and ΔG determined for crystalline rotators from dielectric data.

	ΔH (kcal mol^{-1})	ΔS (cal/(mol K))	$T\Delta S$ (kcal mol^{-1}) for $T = 273$ K	ΔG^a (kcal mol^{-1})
M-*ortho*-F	11.36	7.86	2.15	9.21
M-*meta*-F	5.61	−8.01	−2.19	7.79
M-2F	9.06	−3.40	−0.93	9.99

[a] Calculated for 273 K.

reduced entropy in M-*meta*-F indicates the increase in the internal order within the considered rotational motion.

2.2. *Dielectric response of rotators in a glassy state*

To better understand the differences in the behavior of rotators and how these differences may result from changes in the rotator environment we compared their dielectric responses in a glassy state. The conversion to the disordered glassy state was performed by rapid cooling of molten crystals. As the temperature dropped, the material lost its ability to structural rearrangements, and ultimately, below the glass transition temperature, T_g, the motion of the molecule as a whole became frozen in a glassy state lacking long-range order. Melting temperature, T_m, and T_g for investigated rotators can be recognized from differential scanning calorimetry thermograms presented in figure S24 in supplementary materials. Dielectric responses of glassy samples are presented in figure 3. For all rotators, the dielectric loss spectra $\varepsilon''(f)$ revealed broad loss curves with relaxation times distributed along the available frequency range. The ε''(f) data were satisfactorily fit by the sum of two CC functions, as indicated in figures 3(a)–(c). In a glassy state due to the lower density in comparison to a crystalline state, an excess free volume around the alkyl chain released their mobility. In turn, an additional relaxation process, assigned as γ and related to the chain reorientation was contributed to the $\varepsilon''(f)$ spectra for glassy samples. The γ-relaxation was clearly visible in the spectra of the non-fluorinated derivative M-Ph (figure 3(d)) where it was the only contribution to the dielectric response. The slower β-process was analogous to that observed in crystals and was attributed to the dipolar rotation of the phenylene unit. In the case of non-polar M-Ph, the internal rotation of the phenyl ring did not change a dipole moment and was dielectrically inactive. Consequently, $\varepsilon''(f)$ spectra for M-Ph lack the prominent spectral feature attributed to the β-process (see figure 3(d) and the comparison in figure 3(g)). For both β- and γ-relaxations, the temperature evolution of the characteristic relaxation times follows Arrhenius behavior (solid lines in figure 3(e)) with activation parameters summarized in table 1 (see table S2 in supplementary material for τ (T) values for all experiments). We found that placing a rotator in a disordered glassy environment canceled any differences in rotational parameters between investigated rotators. In contrast to crystals, comparable values of E_a were found for three rotators in a glassy state, i.e. $E_a = 12.37 \pm 0.16$ kcal mol^{-1}

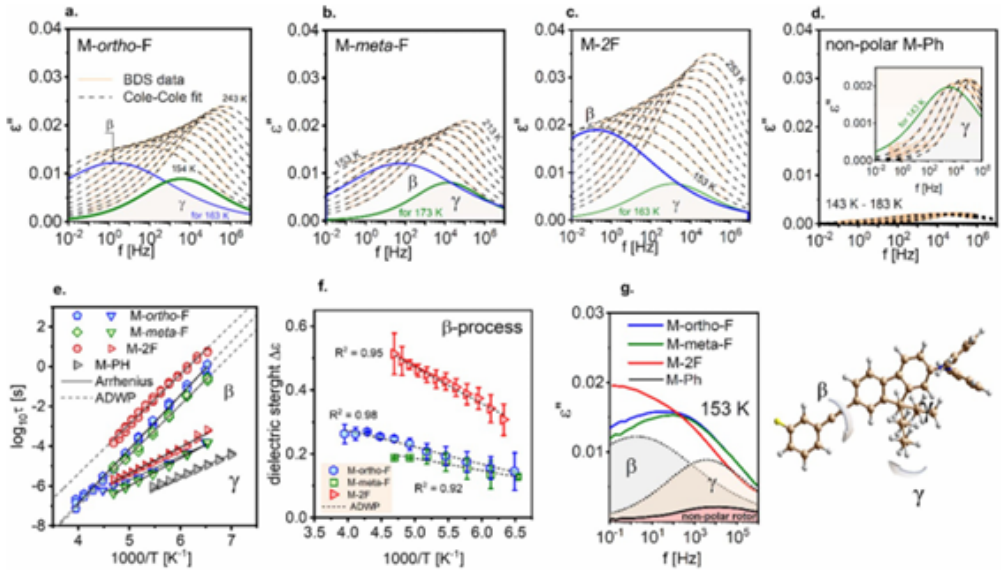

Figure 3. Rotational behavior of polar rotators in a glassy state (a)–(c). A similar pattern of dielectric response acquired for three rotators variously substituted with F atom at different temperatures ($\Delta T = 10$ K). Each dielectric loss spectrum contains two components: β-relaxation (low f) due to rotational motion of the phenylene unit and γ-process (higher f) from chain reorientation (d). The dielectric data for a non-fluorinated rotator ($\Delta T = 10$ K). (e) Temperature dependence of time-scale of rotational motion extracted from dielectric data for β and γ mobility. Solid lines denote Arrhenius fit with resulting activation parameters given in table 1 while dashed lines ADWP fit with parameters given in table 2. (f) The temperature evolution of $\Delta\varepsilon$ ($\pm$uncertainty indicated by error bars) for β-process in three glassy samples. (g) The comparison of dielectric response at $T = 153$ K with graphical indications for β- and γ-relaxations. Note the lack of β-process in non-fluorinated derivative M-Ph.

for M-*ortho*-F, $E_a = 11.58 \pm 0.21$ kcal mol^{-1} for M-*meta*-F, and $E_a = 11.40 \pm 0.17$ kcal mol^{-1} for M-2F. For M-*meta*-F, the observed change in behavior in the crystalline and glassy environment was the most significant since an almost twofold increase in the activation barrier was found as compared to the crystal. In the case of two other rotators, the values of the activation barrier in a crystalline and glassy state were comparable. The unification of the dielectric behavior in a disordered glassy environment occurred also in terms of the $\Delta\varepsilon$ (T^{-1}) behavior. Figure 3(f) shows that the temperature evolution of $\Delta\varepsilon$ was weakly temperature-dependent for all rotators sharing the phenomenology established for secondary relaxations in glass-forming liquids. The analysis of dielectric data for glassy samples in the framework of the ADWP model confirmed similarity in terms of potential asymmetry, returning the comparable Δ value for all three rotators, i.e. $\Delta = 1.03 \pm 0.02$ kcal mol^{-1} for M-ortho-F, $\Delta = 0.95 \pm 0.05$ kcal mol^{-1} for M-meta-F, and $\Delta = 1.03 \pm 0.02$ kcal mol^{-1} for M-2F (see table 2).

2.3. *Single crystal and powder X-ray diffraction studies*

The unification of the rotator's dynamics in the disordered glassy environment indicates that the properties of molecular surroundings impact the rotator's behavior to a large extent. Thus, a detailed understanding of the structural arrangement of molecules in a crystalline lattice was required to explain the distinct behavior of M-*meta*-F. Single crystals were grown by slow evaporation from a dichloromethane solution. X-ray diffraction data collected at 100 K revealed that all sizable systems crystallize in the same space triclinic group P1 with two molecules per unit cell ($Z = 2$) and minor differences in the unit cell parameters. The most relevant crystallographic data are compiled in supplementary table S3. Since the solvent molecule was present in the crystal lattice of all single crystals obtained, it was necessary to verify whether the structure of the solvent-free polycrystals that we studied dielectrically was the same as that of solvates used for x-ray crystallographic studies. The dielectrically tested polycrystalline samples, free of solvent, were recrystallized from the molten liquids directly between capacitor plates. The small size of the grown solvate crystals prevented their direct dielectric measurement. Thus, we powdered the solvate crystals and compared their powder X-ray diffraction patterns with those investigated dielectrically. As presented in figure 4(a), despite some differences in peak intensities, the similarity of peak positions confirmed the structural similarity of crystals. So we used solvate crystallographic data in further studies.

The comparison of single-crystal XRD data for solvates of M-*meta*-F, M-*ortho*-F, and M-2F confirmed their structural similarity in terms of the unit cell type, parameters and space symmetry of crystal lattice. In the case of mono-F-substituted rotators fluorine atom and the corresponding hydrogen atom were rotationally disordered over two positions with a refined

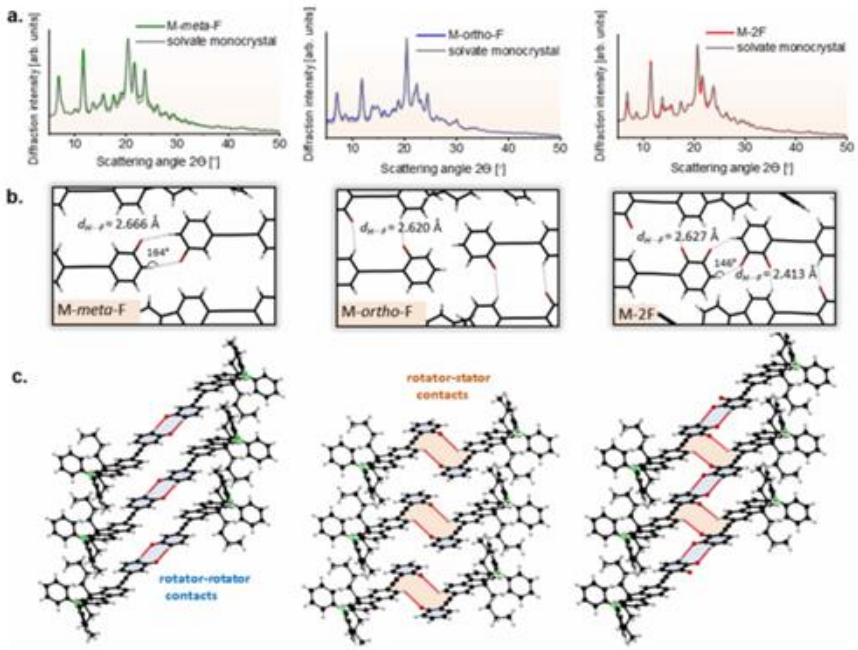

Figure 4. (a) The comparison of X-ray diffraction patterns at $T = 100$ K for powdered solvate monocrystals grown from CH_2Cl_2 solutions and polycrystalline samples that were measured on BDS. (b) The illustration of C–H···F interactions in investigated crystals. Molecular structures were obtained from refined single-crystal XRD data. (c) Packing arrangement obtained from refined single crystal XRD data indicating a distinct pattern of C–H···F contacts in M-*meta*-F (left panel), M-*ortho*-F (middle panel), and M-2F (right panel) crystals. View along $[1,-3,1]$ direction. For clarity, only the fluorine atom with higher occupancy was analyzed. The solvent molecules were removed. Color code: carbon–black, hydrogen–white, fluorine–red, nitrogen–green. Molecular interactions are depicted in red. Shaded areas are a guide for the eye.

ratio of 0.846(5):0.154(5) in M-*meta*-F, and 0.880(3):0.120(3) in M-*ortho*-F. In mono-F-substituted rotators, contrary to M-2F, structures related by 180° ring inversion are no longer equivalent [25, 28].

The most important outcome of structural studies was finding the remarkable differences in the pattern of molecular interactions that lead to substantial differences in stator–rotator and rotator–rotator contacts. In investigated crystals fluorine atom(s) can interact with the static fluorene unit and/or with the rotating unit of neighboring antiparallel arranged molecule via C–H···F contacts that can be regarded as weak hydrogen bonding interactions. Figure 4(b) shows the differences in intermolecular contacts formed in crystals depending on the F-substitution of the phenylene ring.

In M-*ortho*-F only interactions between the fluorine atom of the rotating phenylene ring and the hydrogen atom of the stator (with a distance $d_{H\cdots F} = 2.620$ Å) are possible leading to the situation depicted in figure 4(c) (middle panel). In M-*meta*-F, the situation is different since contrary to M-*ortho*-F, the rotating units of neighboring molecules can interact with each other through C–H···F contacts ($d_{H\cdots F} = 2.666$ Å) as depicted in figure 4(c) (left panel). When the fluorine atom in M-*meta*-F favors contact with the neighboring rotator during the rotation, then the interaction with the static part of a molecule cannot be created. In such a system, the activation energy for rotation will be lower due to the lower population of rotator–stator interactions that inhibit rotation [10]. Thus, the distinct rotational behavior of M-*meta*-F can be explained by a distinct pattern of rotator–rotator and rotator–stator contacts, in particular the lack of intermolecular interactions with a static sizable framework. In M-2F both types of contacts are relevant. A fragment of the crystalline array in figure 4(c) presenting the molecular arrangement of the six molecules with the existing network of C–H···F contacts (shaded areas are guiding for the eye) indicates that the absence of transverse rotator–stator interactions in M-*meta*-F. Such molecular-level features can be determinants of the nearly independent and low-barrier rotation of phenylene units in the crystalline interior. In contrast, the presence of transverse rotator–stator interactions in M-*ortho*-F and M-2F substantially raises the barrier and most likely serves as the source of potential asymmetry.

2.4. DFT calculations

Finally, we used DFT calculations to model the rotational potential to understand better the different rotational performance of M-*meta*-F revealed in BDS investigations. To determine the energy profile in the crystalline environment, a cluster structural model was used. Based on the resolved crystallographic structures, we extracted a fragment containing five

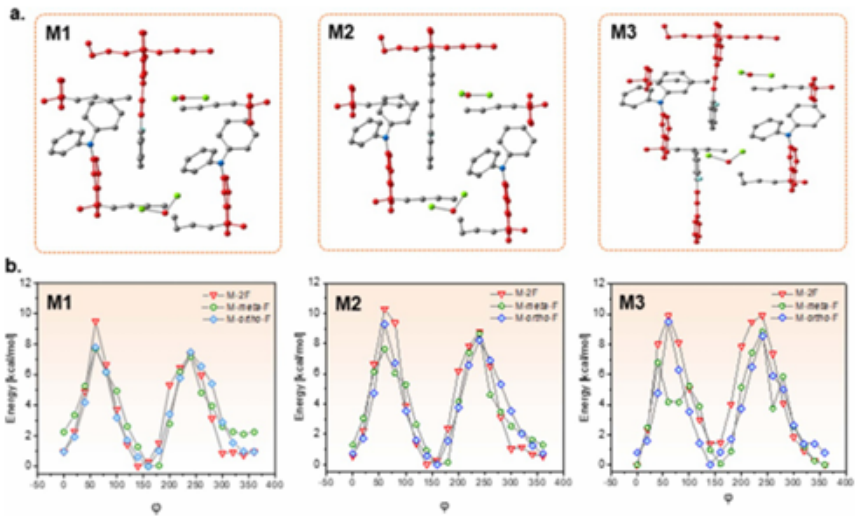

Figure 5. (a) Structural cluster models used in DFT calculations. Fragments that preserve the geometry of the crystallographic structure with frozen atoms during optimization are marked in red. (b) The comparison of computed energy rotation profile as a function of dihedral angle ϕ for sizable crystals with various rotators.

molecules around the rotator. Its geometry for M-2F is shown in figure S25 (left panel) in supplementary data file. Using the fast semi-empirical PM3 [41] method, the initial relaxation of hydrogen atoms was performed while keeping the position of the remaining atoms frozen. To simplify the structure of the cluster for DFT calculations, we removed fragments not remaining in the close and direct vicinity of the rotating unit, see figure S25 (right panel). Free valencies of carbon atoms were then supplemented with hydrogen atoms. Their positions were fully optimized using DFT calculations. For final calculations, we decided that the position of some atoms in the cluster should be frozen to avoid uncontrolled changes in geometry in relation to the crystallographic structure. A series of test calculations helped determine the extent to which the positions of atoms should be frozen, allowing us to obtain the most realistic energy profile for the rotating phenyl group. Full DFT calculations were made for three model molecular clusters labeled M1, M2, and M3 (figure 5(a)). Models M1 and M2 took into account the impact of the nonpolar environment on the rotational motion of phenylene rotators. In model M3, we introduced a second rotator to disentangle the importance of interactions resulting from the presence of another polar unit. The computed potential energy profiles for various models are shown in figure 5(b), while corresponding values of energy barriers ΔE and asymmetries are summarized in table 4 (and table S4 in supporting data file). In the case of isolated molecules, the calculated potential was symmetrical (figure S26 in supporting data file), but for the M1–M3 models, nonequivalent energy minima were found. The only exception was M-2F in the M3 model. In other cases, the non-zero asymmetry was found (in the range of 0.3–2.2 kcal mol^{-1} depending on the compound and

Table 4. DFT calculated values of asymmetries Δ and energy barriers ΔE (smallest value is given) determined from two-maxima potential profiles presented in figure 5(b) for various cluster structural models.

	M-*ortho*-F		M-*meta*-F		M-2 F	
	ΔE	Δ	ΔE	Δ	ΔE	Δ
	(kcal mol^{-1})		(kcal mol^{-1})		(kcal mol^{-1})	
M1	8.2	1.1	7.6	1.1	8.8	1.5
M2	7.5	0.3	7.2	0.5	7.3	2.2
M3	8.6	0.9	6.8	2.1	9.9	0.0

model used). The highest barrier was calculated for the M-2F, and the smallest for M-*meta*-F, regardless of the model used (table 4). Somewhat disappointingly, the agreement between observed and calculated rotational parameters was only semi-quantitative. None of the models reproduced the large difference in barrier heights between M-*meta*-F and M-*ortho*-F observed experimentally. The barrier calculated for M-*meta*-F ranged from 6.8 kcal mol^{-1} to 7.6 kcal mol^{-1}, depending on structural model (see table 4). These values were generally 0.8 kcal mol^{-1} to 1.6 kcal mol^{-1} higher than the experimental data.

In the crystalline phase, the rotation barrier arises from steric hindrance occurring as the rotator moves relative to the surrounding molecules. While rotation of fluorophenylene units in isolated M-*ortho*-F, M-*meta*-F, and M-2F is essentially free, in the crystal structure, it involves a deformation of both geometry of the surrounding molecules, as well as rotator's geometry, particularly affecting the C–C≡C–C bridge. Interestingly, our DFT results indicated that during

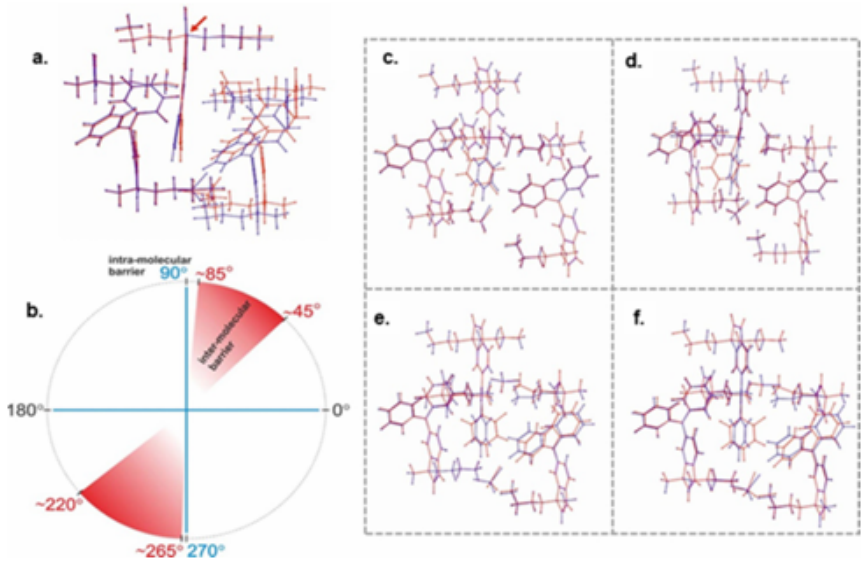

Figure 6. (a) Superimposition of the geometrical structures of M-*meta*-F (blue) and M-*ortho*-F (red). The geometry of the models corresponds to the crystallographic structure of a given isomer with the assumed rotation angle equal to 0°. The rotation angle for the crystallographic structure is 2.97° and −0.65° for meta and ortho isomers, respectively. The superimposition was made for three corresponding atoms in the common fragment of the structure indicated by the red arrow. (b) Schematic representation of the distribution of rotation angle for intramolecular rotation barrier and intermolecular rotator-environment interaction. (c)–(f) Superimposition of relaxed geometric structures of M-*meta*-F and M-*ortho*-F models for rotation angle 0° (blue) and 60° (red). (c), (d) Superimposition of M-*meta*-F structures for M1 and M2, respectively, (e), (f) superimposition of M-*ortho*-F structures for M1 and M2, respectively.

rotation the geometry of M-*meta*-F and M-*ortho*-F relaxes differently (see figure 6(a)). For a meta isomer, the deformation of the rotating unit is more pronounced than the deformation of its surrounding geometry. In contrast, for the ortho isomer, the surrounding deformation is more significant (figures 6(c)–(f), model M1 and M2). It means that the increase in internal energy due to rotation can be more easily compensated by the rotator deformation in M-*meta*-F. In the ortho isomer, however, the higher rigidity of this fragment necessitates conformational changes in the rotator's environment. The plane of the crystallographic structure of the M-*meta*-F is significantly bent (see figure 6(a)) and this effect intensifies when the phenylene group rotates. This deformation disturbs the π-electron system on the acetylene bridge, but this effect is partially mitigated by the electron density from fluorine-substituted phenylene units. This compensation is likely more effective and energetically favorable in the M-*ortho*-F. Consequently, the rotation of the phenyl ring in M-*ortho*-F induces more changes in the surrounding geometry, increasing the internal energy of the system. Such an energetic compromise between intramolecular and intermolecular relaxation yields a slightly higher rotational barrier for the ortho isomer in comparison to the meta isomer.

Additionally, our DFT results suggest that steric hindrance manifests significantly either before or immediately after reaching the intramolecular rotation barrier, depending on the direction of rotator motion (see figure 6(b)). Given this complexity, accurately estimating the energetics of the barrier in the crystal phase is challenging and requires further, more detailed studies.

3. Conclusion

We revealed two patterns of dielectric response for fluoro-substituted phenylene rotators more and less rapidly rotating inside the framework of sizable crystals. Their distinct dynamic behavior could be distinguished by a different pattern of peak amplitude temperature changes and rationalized in the framework of the ADWP model. We found that each pattern has a 'fingerprint' of the potential asymmetry which reflects the impact of the rotators surrounding. Negligible asymmetry and the smallest rotational barrier were found for a crystal favoring rotator–rotator contacts. The opposite behavior was observed for crystals with an asymmetric potential and a higher barrier due to the presence of hindering rotator-stator interactions. We demonstrated in our study that the character of interactions between the rotator and its surroundings that impact rotational potential and differentiate the rotational performance of studied rotators can be correlated with dielectric response allowing us to distinguish low- (i.e. more independent) and high-energy (more hindered) barrier patterns of dielectric behaviors. Extension of dielectric research to other groups of amphidynamic crystals in the future will verify the universality of our observation. This is an important step in building our physical intuition for recognizing and linking

spectral features with the molecular-level characteristics of internal rotations in crystalline rotators.

4. Experimental section

4.1. Dielectric measurements

Dielectric measurements were performed on polycrystalline and glassy samples in the broad frequency range from 10^{-1} Hz to $3{\cdot}10^{6}$ Hz using a Novo-Control GMBH Alpha dielectric spectrometer. The sample was placed in a stainless-steel parallel-plate capacitor (15 mm in diameter) with two fused silica fibers providing a gap of 0.1 mm. The temperature was controlled using a Novocool cryosystem (for crystals, with an accuracy of 0.3 K) or Quatro cryosystem (for glasses) with a stabilization accuracy of 0.1 K. Before measuring the rotational dynamics of the polycrystalline samples, the material was melted *in situ* between capacitor plates and cooled to a temperature where it was held until complete crystallization, i.e. $T = 373$ K for M-*meta*-F and M-*ortho*-F and $T = 371$ K for M-2F. The crystalline sample was then measured on cooling. Progress of crystallization was manifested by a gradual decrease of dielectric strength (being proportional to the number of actively reorienting dipoles) monitored for fixed frequency, while crystallization completion by a persistent lack of spectral changes (see figure 2(d)). The full crystallinity of the sample was confirmed by the absence of the glass transition on the DSC thermograms recorded after completing the BDS measurement. The measurements of glassy samples were performed by melting the sample *in situ* and cooling it below the glass transition temperature. There was no evidence of other phase transitions on the DSC thermograms in the range of 200 K–400 K. Relevant DSC data is shown in supplementary figure S24. We analyzed the dielectric data in the permittivity representation $\varepsilon^*(f) = \varepsilon'(f) - \mathrm{i}\varepsilon''(f)$, where ε' is the real and ε'' is the imaginary part. The fitting of $\varepsilon''(f)$ data with the CC function was performed using the WinFit program (Novocontrol). The standard deviations of fitting parameters depend on the quality of the fit and scattering between experimental points. We assumed that measured data points have the same relative accuracy without systematic errors. Activation parameters were determined based on three independent experiments.

4.2. X-ray diffraction

The X-ray single crystal structural studies were performed at $T = 100$ K with a four-circle SuperNova x-ray diffractometer with microfocus x-ray tube, optimized multi-layer optics for Mo–Kα ($\lambda = 0.71073$ Å) radiation, and an Atlas CCD detector. We used an Oxford Cryosystem; the temperature stability was 0.1 K. The control over the measurement and the data reduction were performed by CrysAlis$^{\mathrm{Pro}}$ software [42]. The crystal structures were solved using the SHELXS-2013 program and refined with the SHELXL-2019/2 program [43]. The non-hydrogen atoms were refined with anisotropic displacement parameters. Hydrogen atoms were introduced to the structure by appropriate rigid body constraints (AFIX 23, AFIX 43, AFIX 137) with $U_{\mathrm{iso}}(H)$ equal to $1.2U_{\mathrm{eq}}(C)$ or $1.5U_{\mathrm{eq}}(C)$. Crystal data and CheckCif reports are available as supplementary CIF data and supplementary XRD data, respectively. B-level alerts can be explained by the low symmetry of all crystal structures. Analysis of the diffraction patterns also revealed that the reflections with the lowest values of the theta angle were eliminated by the beam stop which is related to the use of Mo radiation.

4.3. DFT calculations

The reported calculational results were obtained by applying the DFT [44] level of theory with the hybrid B3LYP functional [45–47] and the def2-SVP basis set [48]. For all considered structures, the presence of dispersion interactions was taken into account by including semi-empirical D3BJ [49–52] dispersion corrections. The energy barrier of the rotational motion of the substituted phenyl ring with respect to the axis of the acetylene bridge was determined based on the energy profile calculated as a function of the dihedral angle ϕ, between the plane of the phenyl ring and that of the fluorene motif. The definition of the ϕ dihedral angle is shown in figure 1(a). Total energies have been calculated at the frozen value of the ϕ angle in the range from 0° to 350° with the step of 10°. Calculations were carried out with the use Gaussian 16 quantum chemistry package [53]. All calculations for the cluster structural model were performed using the 5.03 version of the ORCA [54–56] package. The basic analysis of the calculation results, as well as the drawings presenting the geometry, were made with the ChemCraft [57] program. The calculated geometric coordinates are included in supplementary DFT data. Part 'Isolated molecule' contains the coordinates of atoms for isolated isomers (vacuum, gas state), respectively for minima and transition states. The second part 'Structural models' contains optimized geometries for M1, M2, and M3 models.

Data availability statement

The X-ray crystallographic coordinates for M-*ortho*-F, M-*meta*-F, and M-2F reported in this study have been deposited at the Cambridge Crystallographic Data Centre (CCDC), under deposition number 2259776 (M-*ortho*-F), 2259777 (M-*meta*-F) and 2259778 (M-2F). These data can be obtained free of charge from The Cambridge Crystallographic Data Centre via www.ccdc.cam.ac.uk/structures.

The data that support the findings of this study are openly available at the following URL/DOI: 10.18150/UQAPHK [58].

Acknowledgments

This research was funded as a whole by National Science Centre, Poland. Project No. 2021/41/B/ST5/00992. For Open Access, the author has applied a CC-BY public copyright

license to any Author Accepted Manuscript (AAM) version arising from this submission. Calculations have been carried out in Wrocław Centre for Networking and Supercomputing (http://www.wcss.pl) under grant No. 18.

Author contribution

M R -B. conceived the project, performed dielectric measurements, analyzed the data, and wrote the manuscript, A B. carried out DSC and dielectric measurements, P L performed the DFT calculations, K J performed XRD measurements and analyzed XRD data, M K resolved and refined crystalline single crystal structures. J K performed single crystal X-ray measurements, W M, M F, M T, J K synthesized compounds, and M P supervised the project.

Conflict of interest

The authors declare no competing interests.

ORCID iDs

Marzena Rams-Baron https://orcid.org/0000-0001-8808-8067
Alfred Błażytko https://orcid.org/0000-0003-4653-0421
Karolina Jurkiewicz https://orcid.org/0000-0002-4289-7827
Piotr Lodowski https://orcid.org/0000-0002-5791-9208
Maria Książek https://orcid.org/0000-0001-9856-5090
Joachim Kusz https://orcid.org/0000-0001-8156-936X
Mahshid Teymouri https://orcid.org/0009-0005-3896-8185
Julia Krzywik https://orcid.org/0000-0003-3611-0984
Marian Paluch https://orcid.org/0000-0002-7280-8557

References

[1] Einstein A 1906 Zur Theorie der Brownschen Bewegung *Ann. Phys.* **324** 371–81
[2] Debye P 1912 Einige Resultate Einer Kinetischen Theorie Der Isolatoren *Phys.* Z **13** 97–100
[3] Debye P 1913 Zur Theorie Der Anomalen Dispersion im Gebiete der langwelligen elektrischen Strahlung *Verh. Dtsch. Phys. Ges.* **15** 777–93
[4] Lancia F, Ryabchun A and Katsonis N 2019 Life-like motion driven by artificial molecular machines *Nat. Rev. Chem.* **3** 536–51
[5] Aprahamian I 2020 The future of molecular machines *ACS Cent. Sci.* **6** 347–58
[6] Dattler D, Fuks G, Heiser J, Moulin E, Perrot A, Yao X and Giuseppone N 2020 Design of collective motions from synthetic molecular switches, rotors, and motors *Chem. Rev.* **120** 310–433
[7] Kistemaker J C M, Štacko P, Visser J and Feringa B L 2015 Unidirectional rotary motion in achiral molecular motors *Nat. Chem.* **7** 890–6
[8] Howe M E and Garcia-Garibay M A 2019 The roles of intrinsic barriers and crystal fluidity in determining the dynamics of crystalline molecular rotors and molecular machines *J. Org. Chem.* **84** 9835–49
[9] Roke D, Wezenberg S J and Feringa B L 2018 Molecular rotary motors: unidirectional motion around double bonds *Proc. Natl Acad. Sci.* **115** 9423–31
[10] Navarro-Huerta A, Jellen M J, Arcudia J, Teat S J, Toscano R A, Merino G and Rodríguez-Molina B 2021 Tailoring the cavities of hydrogen-bonded amphidynamic crystals using weak contacts: towards faster molecular machines *Chem. Sci.* **12** 2181–8
[11] Gonzalez-Nelson A *et al* 2021 Emergence of coupled rotor dynamics in metal–organic frameworks via tuned steric interactions *J. Am. Chem. Soc.* **143** 12053–62
[12] Zhu K, O'Keefe C A, Vukotic V N, Schurko R W and Loeb S J 2015 A molecular shuttle that operates inside a metal–organic framework *Nat. Chem.* **7** 514–9
[13] Garcia-Garibay M A 2005 Crystalline molecular machines: encoding supramolecular dynamics into molecular structure *Proc. Natl Acad. Sci.* **102** 10771–6
[14] Karlen S D, Reyes H, Taylor R E, Khan S I, Hawthorne M F and Garcia-Garibay M A 2010 Symmetry and dynamics of molecular rotors in amphidynamic molecular crystals *Proc. Natl Acad. Sci.* **107** 14973–7
[15] Jin M, Ando R, Jellen M J, Garcia-Garibay M A and Ito H 2021 Encapsulating N -heterocyclic carbene binuclear transition-metal complexes as a new platform for molecular rotation in crystalline solid-state *J. Am. Chem. Soc.* **143** 1144–53
[16] Aguilar-Granda A, García-González M C, Pérez-Estrada S, Kozina A and Rodríguez-Molina B 2018 Nanoscale organization and solid-state dynamics of carbazole-[π]-carbazole rotors edged with aliphatic chains *J. Phys. Chem.* C **122** 27093–9
[17] Liepuoniute I, Huynh C M, Perez-Estrada S, Wang Y, Khan S, Houk K N and Garcia-Garibay M A 2020 Enhanced rotation by ground state destabilization in amphidynamic crystals of a dipolar 2,3-difluorophenylene rotator as established by solid state 2 H NMR and dielectric spectroscopy *J. Phys. Chem.* C **124** 15391–8
[18] Vogelsberg C S and Garcia-Garibay M A 2012 Crystalline molecular machines: function, phase order, dimensionality, and composition *Chem. Soc. Rev.* **41** 1892–910
[19] Liepuoniute I, Jellen M J and Garcia-Garibay M A 2020 Correlated motion and mechanical gearing in amphidynamic crystalline molecular machines *Chem. Sci.* **11** 12994–3007
[20] Colin-Molina A, Jellen M J, García-Quezada E, Cifuentes-Quintal M E, Murillo F, Barroso J, Pérez-Estrada S, Toscano R A, Merino G and Rodríguez-Molina B 2019 Origin of the isotropic motion in crystalline molecular rotors with carbazole stators *Chem. Sci.* **10** 4422–9
[21] Dominguez Z, Khuong T-A V, Dang H, Sanrame C N, Nuñez J E and Garcia-Garibay M A 2003 Molecular compasses and gyroscopes with polar rotors: synthesis and characterization of crystalline forms *J. Am. Chem. Soc.* **125** 8827–37
[22] Zhang W, Ye H-Y, Graf R, Spiess H W, Yao Y-F, Zhu R-Q and Xiong R-G 2013 Tunable and switchable dielectric constant in an amphidynamic crystal *J. Am. Chem. Soc.* **135** 5230–3
[23] Liu Z, Wang Y and Garcia-Garibay M A 2021 Rotational dynamics of an amphidynamic zirconium metal–organic framework determined by dielectric spectroscopy *J. Phys. Chem. Lett.* **12** 5644–8
[24] Y-s S *et al* 2021 Dipolar order in an amphidynamic crystalline metal–organic framework through reorienting linkers *Nat. Chem.* **13** 278–83
[25] Horansky R D, Clarke L I, Winston E B, Price J C, Karlen S D, Jarowski P D, Santillan R and Garcia-Garibay M A 2006 Dipolar rotor-rotor interactions in a difluorobenzene molecular rotor crystal *Phys. Rev.* B **74** 054306

[26] Schnabel J, Schulz A, Lunkenheimer P and Volkmer D 2023 Benzothiadiazole-based rotation and possible antipolar order in carboxylate-based metal-organic frameworks *Commun. Chem.* **6** 161
[27] Harada J, Ohtani M, Takahashi Y and Inabe T 2015 Molecular motion, dielectric response, and phase transition of charge-transfer crystals: acquired dynamic and dielectric properties of polar molecules in crystals *J. Am. Chem. Soc.* **137** 4477–86
[28] Horansky R D, Clarke L I, Price J C, Khuong T-A V, Jarowski P D and Garcia-Garibay M A 2005 Dielectric response of a dipolar molecular rotor crystal *Phys. Rev.* B **72** 014302
[29] Perego J *et al* 2023 Benchmark dynamics of dipolar molecular rotors in fluorinated metal-organic frameworks *Angew. Chem., Int. Ed. Engl.* **62** e202215893
[30] Namsani S and Yazaydin A O 2018 Electric field induced rotation of halogenated organic linkers in isoreticular metal–organic frameworks for nanofluidic applications *Mol. Syst. Des. Eng.* **3** 951–8
[31] Michl J and Sykes E C H 2009 Molecular rotors and motors: recent advances and future challenges *ACS Nano* **3** 1042–8
[32] Kremer F and Schonhals A 2003 *Broadband Dielectric Spectroscopy* (Springer)
[33] Siegemund G, Schwertfeger W, Feiring A, Smart B, Behr F, Vogel H and McKusick B 2000 Fluorine compounds *Organic Ullmann's Encyclopedia of Industrial Chemistry* (Wiley) pp 141–65
[34] Richert R 2015 Probing liquid dynamics, one molecule at a time *Proc. Natl Acad. Sci.* **112** 4841–2
[35] Gilroy K S and Phillips W A 1981 An asymmetric double-well potential model for structural relaxation processes in amorphous materials *Phil. Mag.* B **43** 735–46
[36] Dyre J C and Olsen N B 2003 Minimal model for beta relaxation in viscous liquids *Phys. Rev. Lett.* **91** 155703
[37] Kottas G S, Clarke L I, Horinek D and Michl J 2005 Artificial molecular rotors *Chem. Rev.* **105** 1281–376
[38] Glasstone S, Laidler K J and Eyring H 1941 *The Theory of Rate Processes: The Kinetics of Chemical Reactions, Viscosity, Diffusion and Electrochemical Phenomena* (McGraw-Hill Book Company, Incorporated)
[39] Eyring H 1936 Viscosity, plasticity, and diffusion as examples of absolute reaction rates *J. Chem. Phys.* **4** 283–91
[40] Eyring H 1935 The activated complex and the absolute rate of chemical reactions *Chem. Rev.* **17** 65–77
[41] Stewart J J P 1989 Optimization of parameters for semiempirical methods I *Method J. Comput. Chem.* **10** 209–20
[42] Rigaku Oxford Diffraction 2015 *CrysAlis Pro Software system* version 1.171.38.41q (Rigaku Corporation)
[43] Sheldrick G M 2015 Crystal structure refinement with SHELXL *Acta Crystallogr.* C **71** 3–8
[44] Kohn W and Sham L J 1965 Self-consistent equations including exchange and correlation effects *Phys. Rev.* **140** A1133–8
[45] Becke A D 1988 Density-functional exchange-energy approximation with correct asymptotic behavior *Phys. Rev.* A **38** 3098–100
[46] Lee C, Yang W and Parr R G 1988 Development of the Colle-Salvetti correlation-energy formula into a functional of the electron density *Phys. Rev.* B **37** 785–9
[47] Becke A D 1993 Density-functional thermochemistry. III. The role of exact exchange *J. Chem. Phys.* **98** 5648–52
[48] Weigend F and Ahlrichs R 2005 Balanced basis sets of split valence, triple zeta valence and quadruple zeta valence quality for H to Rn: design and assessment of accuracy *Phys. Chem. Chem. Phys.* **7** 3297
[49] Grimme S 2006 Semiempirical GGA-type density functional constructed with a long-range dispersion correction *J. Comput. Chem.* **27** 1787–99
[50] Grimme S, Antony J, Ehrlich S and Krieg H 2010 A consistent and accurate ab initio parametrization of density functional dispersion correction (DFT-D) for the 94 elements H-Pu *J. Chem. Phys.* **132** 154104
[51] Grimme S, Ehrlich S and Goerigk L 2011 Effect of the damping function in dispersion corrected density functional theory *J. Comput. Chem.* **32** 1456–65
[52] Caldeweyher E, Bannwarth C and Grimme S 2017 Extension of the D3 dispersion coefficient model *J. Chem. Phys.* **147** 034112
[53] Frisch M J *et al* 2019 Gaussian 16 revision C.01
[54] Neese F 2012 The ORCA program system *Wiley Interdiscip. Rev.-Comput. Mol. Sci.* **2** 73–78
[55] Neese F 2017 Software update: the ORCA program system, version 4.0 *Wiley Interdiscip. Rev.-Comput. Mol. Sci.* **8** e1327
[56] Neese F An ab initio, DFT and semiempirical SCF-MO package
[57] Zhurko G and Zhurko D 2015 Chemcraft graphical software for visualization of quantum chemistry computations (available at: www.chemcraftprog.com)
[58] Rams-Baron M, Błażytko A, Jurkiewicz K, Lodowski P, Książek M, Kusz J and Paluch M 2024 Dataset from the analysis of solid-state dielectric, structural, and DFT data for phenylene rotors with fluorine atom(s) *RepOD, V1* (https://doi.org/10.18150/UQAPHK)

Supplementary Material

Image of the solid-state rotary motion encoded in the dielectric response

Marzena Rams-Baron[1*], Alfred Błażytko[1], Karolina Jurkiewicz[1], Piotr Lodowski[2], Maria Książek[1], Joachim Kusz[1], Witold Mozga[3], Marta Fordymacka[3], Mahshid Teymouri[3], Julia Krzywik[3], Marian Paluch[1,2]

[1]*August Chełkowski Institute of Physics, University of Silesia in Katowice, 75 Pulku Piechoty 1, 41-500 Chorzow, Poland*

[2]*Institute of Chemistry, University of Silesia in Katowice, Szkolna 9, 40-006 Katowice, Poland*

[3]*TriMen Chemicals Sp. z o.o., Al. Piłsudskiego 141, 92-318 Łódź, Poland*

*corresponding autor: marzena.rams-baron@us.edu.pl

1. Supplementary Methods

1.1 General Information

All substrates and reagents were purchased from Angene Chemical. Dry solvents: tetrahydrofuran (THF), dichlomethane (DCM), N,N-dimethylformamide (DMF), dimethylsulphoxide (DMSO), acetonitrile (ACN), methanol (MeOH) and ethyl acetate (EtOAc) were obtained commercially and used directly without additional treatment.

Nuclear Magnetic Resonance (NMR) spectra were acquired on a Bruker 400 or Bruker 700 instrument. For ^{1}H NMR and $^{13}C\{^{1}H\}$ NMR, chemical shifts were reported in the scale relative to the residual signal of solvent ($CHCl_3$) as an internal reference. For ^{19}F NMR, $CFCl_3$ was used as the external reference with chemical shift at 0 ppm.

UPLC analyses were run on a Waters Aquity separation module with an Aquity PDA eλ detector equipped with a Kinetex Biphenyl column 50 × 2.1mm, 1.7 µm; flow 0.8 mL/min; gradient 3-97% of acetonitrile in water over 3 min, then 1.5min of 97% acetonitrile (both mobile phases contained an addition of 0.04% of formic acid). Electrospray ionization (ESI) mass spectra were obtained with Waters SQ detector 2. M-Ph was analyzed using ACQUITY UPLC BEH C18 Column, 130Å, 1.7 µm, 2.1 mm X 50 mm with the same gradient and apparatus.

High-resolution mass spectrometry (HRMS) measurements were performed using Synapt G2-Si mass spectrometer (Waters) equipped with an ESI source and quadrupole-Time-of- Flight mass analyser. The mass spectrometer was operated in the positive ion detection mode. The optimized source parameters were: capillary voltage 3.0 kV, cone voltage 30 V, source temperature 120°C, desolvation gas (nitrogen) flow rate 600 L/h with the temperature 350°C, nebulizer gas pressure 6.5 bar.To ensure accurate mass measurements, data were collected in centroid mode, and mass was corrected during acquisition using leucine encephalin solution as an external reference, Lock-SprayTM, (Waters Corp., Milford, MA,USA), which generated reference ion at m/z 556.2771 Da ($[M+H]^+$) in positive ESI mode. The results of the measurements were processed using the MassLynx 4.1 software (Waters).

1.2 Synthesis

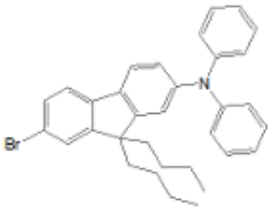

(7-Bromo-9,9-dibutyl-9H-fluoren-2-yl)-diphenylamine was prepared in 54% yield (2.60 g) starting from commercially available 2-bromo-7-iodo-9H-Fluorene, (5.00 g, 13.4 mmol) as yellow crystals according to the literature procedure [[1]].

^{1}H NMR (400 MHz, $CDCl_3$) δ 7.54 (d, J = 8.2 Hz, 1H), 7.51 – 7.40 (m, 3H), 7.28 (m, 4H), 7.13 (m, 5H), 7.09 – 6.99 (m, 3H), 1.93 – 1.78 (m, 4H), 1.20 – 1.02 (m, 4H), 0.73 (t, J = 7.3 Hz, 6H), 0.69 – 0.55 (m, 4H).

^{13}C {^{1} H} NMR (151 MHz, $CDCl_3$) δ 152.9, 151.7, 147.9, 147.6, 140.0, 135.0, 129.9, 129.2, 126.0, 124.0, 123.4, 122.7, 120.4, 120.1, 119.0, 55.3, 39.90, 26.0, 23.0, 13.9.

LCMS (ESI+) m/z: Calc. for $C_{33}H_{34}BrN$ 524.5; Found $(M + H)^+$ 525.7.

(9,9-Dibutyl-7-phenylethynyl-9H-fluoren-2-yl)-diphenylamine (M-Ph)

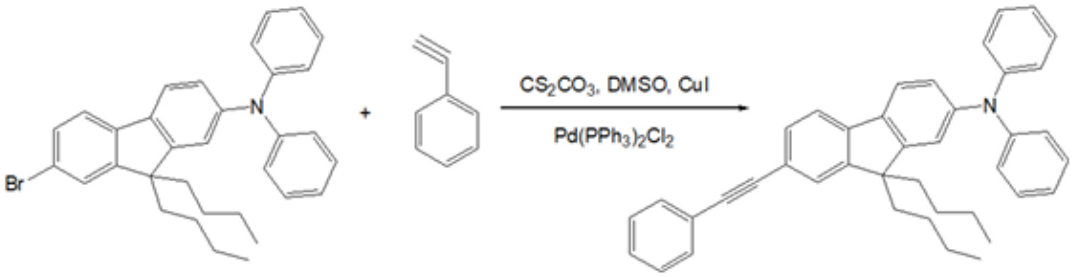

(7-Bromo-9,9-dibutyl-9H-fluoren-2-yl)-diphenylamine (2.0 g, 3.8 mmol, 1.0 equiv) was dissolved in DMSO (20 mL) in a 250 mL three neck flask then Cs_2CO_3 (3.10 g, 9.53 mmol, 2.5 equiv) and phenylacetylene (467.15 mg, 4.57 mmol, 1.2 equiv) were added into the solution. Air was removed by vacuum pump and the reaction mixture was degassed by introducing argon. After degassing, CuI (72.56 mg, 0.38 mmol, 0.1 equiv) and $Pd(PPh_3)_2Cl_2$ (53.51 mg, 0.076 mmol, 0.02 equiv) were added to the flask sequentially under argon. The reaction mixture was heated to 100°C and stirred under argon. Progress of the reaction was monitored by TLC and LCMS. After 3 hours the substrates were consumed and the mixture cooled to room

temperature, then water (200 mL) was added to the flask along with EtOAc (200 mL). Phases were separated and the organic layer was washed twice by water and brine then dried over Na_2SO_4. After the solvents were removed under reduced pressure, the crude product was purified by silica gel column chromatography using neat hexane as eluent. Crystallization from DCM/MeOH gave the pure product as yellow crystals (1.30 g, 62% yield).

^{1}H NMR (400 MHz, $CDCl_3$) δ 7.60 (m, 4H), 7.56 – 7.47 (m, 2H), 7.44 – 7.34 (m, 3H), 7.29 (m, 4H), 7.17 (m, 5H), 7.05 (m, 3H), 1.91 (pd, J = 13.3, 5.8 Hz, 4H), 1.21 – 1.04 (m, 4H), 0.82 – 0.57 (m, 10H).

^{13}C {^{1}H} NMR (151 MHz, $CDCl_3$) δ 152.5, 150.7, 147.9, 147.6, 141.3, 135.4, 131.6, 130.8, 129.2, 128.4, 128.1, 125.8, 124.0, 123.5, 123.3, 122.7, 120.7, 120.5, 119.0, 119.0, 90.7, 89.3, 55.1, 40.0, 26.0, 23.0, 13.9.

LCMS (ESI+) m/z: Calc. for $C_{41}H_{39}N$ 545.3; Found $(M + H)^+$ 545.6.

HRMS (ESI+) m/z: Calc. for $C_{41}H_{40}N$ 546.3161; Found $(M + H)^+$ 546.3149

N-{7-[(3-fluorophenyl)ethynyl]-9,9-dibutyl-9H-fluoren-2-yl}-N,N-diphenylamine (M-meta-F)

(7-Bromo-9,9-dibutyl-9H-fluoren-2-yl)-diphenylamine (2.5 g, 4.77 mmol, 1.0 equiv) was dissolved in a mixture of DMSO (20 mL) and THF (2 mL) in a 250 mL three neck flask then Cs_2CO_3 (4.65 g, 14.3 mmol, 3.0 equiv) and 3-fluorophenylacetylene (859 mg, 7.15 mmol, 1.5 equiv) were added into the solution. Air was removed by vacuum pump and the reaction mixture was degassed by introducing argon. After degassing, CuI (90.6 mg, 0.477 mmol, 0.1 equiv) and $Pd(PPh_3)_2Cl_2$ (100 mg, 0.143 mmol, 0.03 equiv) were added to the flask sequentially under argon. The reaction mixture was heated to 60°C and stirred under argon. Progress of the reaction was monitored by TLC and LCMS. When the substrates were consumed and the mixture cooled to room temperature, then water (200 mL) was added to the flask along with DCM (200 mL).

Phases were separated and the organic layer was washed twice by water and brine then dried over Na_2SO_4. After the solvents were removed under reduced pressure, the crude product was purified by silica gel column chromatography using neat hexane as eluent. Product crystallized upon standing and was washed with ACN to give yellowish crystals (2.3 g, 85% yield).

^{1}H NMR (400 MHz, $CDCl_3$) δ 7.60 (m, 2H), 7.55 – 7.45 (m, 2H), 7.36 (m, 2H), 7.28 (m, 5H), 7.16 (m, 5H), 7.06 (m, 4H), 1.99 – 1.79 (m, 4H), 1.20 – 1.01 (m, 4H), 0.74 (t, J = 7.3 Hz, 6H), 0.65 (dd, J = 18.5, 11.5 Hz, 4H).

^{19}F NMR{^{1} H} (377 MHz, $CDCl_3$) δ -112.39.

^{13}C NMR{^{1} H} (101 MHz, $CDCl_3$) δ 163.7, 161.2, 152.5, 150.7, 147.9, 147.8, 141.7, 135.3, 130.9, 123.0, 129.9, 129.2, 127.5, 127.4, 125.9, 124.1, 123.3, 122.8, 120.8, 120.0, 119.1, 118.9, 118.4, 118.2, 115.5, 115.3, 91.6, 88.0, 55.1, 40.0, 26.0, 23.0, 13.9.

LCMS (ESI$^+$) m/z: Calc. for $C_{41}H_{38}FN$ 563.3; Found $(M + H)^+$ 564.6.

HRMS (ESI$^+$) m/z: Calc. for $C_{41}H_{39}FN$ 564.3067; Found $(M + H)^+$ 564.3058

N-{7-[(2-fluorophenyl)ethynyl]-9,9-dibutyl-9H-fluoren-2-yl}-N,N-diphenylamine (M-*ortho*-F)

(7-Bromo-9,9-dibutyl-9H-fluoren-2-yl)-diphenylamine (4 g, 7.63 mmol, 1.0 equiv) was dissolved in a mixture of DMF (50 mL) and THF (10 mL) in a 250 mL three neck flask, then Cs_2CO_3 (6.2 g, 19.1 mmol, 2.5 equiv) was added and argon was bubbled through the solution for 15 minutes. CuI (160 mg, 0.84 mmol, 0.11 equiv) and $Pd(PPh_3)_2Cl_2$ (160 mg, 0.23 mmol, 0.03 equiv) were added to the flask and argon was again bubbled for 5 minutes, then 2-fluorophenylacetylene (1.36 g, 11.4 mmol, 1.5 equiv) was added into the solution. The reaction mixture was refluxed for two hours under argon. Progress of the reaction was monitored by TLC and LCMS. As the substrates were consumed the mixture was taken into water (200 mL)

and shaken with EtOAc (200 mL) and hexane (50 mL). Phases were separated and the organic layer was washed twice by water and brine then dried over Na_2SO_4. After the solvents were removed under reduced pressure, the crude product was purified by silica gel column chromatography using neat hexane as eluent. After evaporating to dryness the product crystallized upon standing to give pure yellowish crystals (3.3 g, 76% yield).

^{1}H NMR (700 MHz, $CDCl_3$) δ 7.61 (dd, J = 7.8, 0.4 Hz, 2H), 7.60 – 7.56 (m, 1H), 7.55 (dd, J = 7.8, 1.4 Hz, 1H), 7.51 (d, J = 0.9 Hz, 1H), 7.36 – 7.31 (m, 1H), 7.30 – 7.25 (m, 4H), 7.18 – 7.13 (m, 7H), 7.05 (ddd, J = 7.1, 2.1, 1.2 Hz, 3H), 1.97 – 1.82 (m, 4H), 1.19 – 1.03 (m, 4H), 0.74 (t, J = 7.4 Hz, 6H), 0.71 – 0.61 (m, 4H).

^{19}F {^{1} H} NMR (235 MHz, $CDCl_3$) δ -110.95.

^{13}C{^{1} H} NMR (101 MHz, $CDCl_3$) δ 163.8, 161.3, 152.5, 150.7, 147.9, 147.7, 141.7, 135.4, 133.4, 130.9, 129.8, 129.8, 129.2, 125.9, 124.0, 123.2, 122.7, 120.8, 120.1, 119.0, 118.9, 115.7, 115.5, 112.3, 112.1, 95.8, 82.5, 55.1, 40.0, 26.0, 23.0, 13.9.

LCMS (ESI$^+$) m/z: Calc. for $C_{41}H_{38}FN$ 563.3; Found $(M + H)^+$ 564.5.

HRMS (ESI$^+$) m/z: Calc. for $C_{41}H_{39}FN$ 564.3067; Found $(M + H)^+$ 564.3060.

N-{7-[(2,3-difluorophenyl)ethynyl]-9,9-dibutyl-9H-fluoren-2-yl}-N,N-diphenylamine (M-2F)

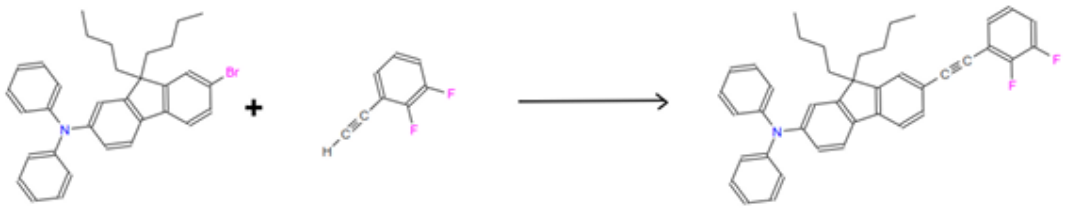

(7-Bromo-9,9-dibutyl-9H-fluoren-2-yl)-diphenylamine (5.4 g, 10.3 mmol, 1.0 equiv) was dissolved in a mixture of DMF (50 mL) and THF (10 mL) in a 250 mL three neck flask, then Cs_2CO_3 (8.4 g, 25.8 mmol, 2.5 equiv) was added and argon was bubbled through the solution for 15 minutes. CuI (200 mg, 1.1 mmol, 0.11 equiv) and $Pd(PPh_3)_2Cl_2$ (210 mg, 0.3 mmol, 0.03 equiv) were added to the flask and argon was again bubbled for 5 minutes, then 2,3-difluorophenylacetylene (3.58 g, 20.6 mmol, 2 equiv) was added into the solution. The reaction

mixture was refluxed for three hours under argon. Progress of the reaction was monitored by TLC and LCMS. As the substrates were consumed the mixture was taken into water (200 mL) and shaken with EtOAc (200 mL) and hexane (50 mL). Phases were separated and the organic layer was washed twice by water and brine then dried over Na_2SO_4. After the solvents were removed under reduced pressure, the crude product was purified by silica gel column chromatography using neat hexane as eluent. After evaporating to dryness the product crystallized upon standing to give yellowish crystals (4.0 g, 67% yield, 96% purity).

^{1}H NMR (400 MHz, $CDCl_3$) δ 7.58 (m, 3H), 7.51 (s, 1H), 7.37 – 7.24 (m, 5H), 7.21 – 7.12 (m, 6H), 7.12 – 6.99 (m, 4H), 2.00 – 1.80 (m, 4H), 1.20 – 1.04 (m, 4H), 0.74 (t, J = 7.3 Hz, 6H), 0.71 – 0.58 (m, 4H).

^{19}F{^{1} H} NMR (377 MHz, $CDCl_3$) δ -134.57, -134.62, -136.88, -136.94.

^{13}C{^{1} H} NMR (101 MHz, $CDCl_3$) δ 152.6, 152.0, 151.9, 150.7, 149.6, 149.5, 149.4, 147.9, 142.0, 135.0, 131.2, 129.3, 128.2, 128.2, 125.9, 124.1, 124.0, 123.2, 122.8, 120.8, 119.7, 119.1, 118.86, 117.3, 117.1, 114.4, 97.0, 55.1, 40.0, 26.0, 23.0, 13.9.

LCMS (ESI$^+$) m/z: Calc. for $C_{41}H_{38}FN$ 581.3 Found $(M + H)^+$ 582.4

HRMS (ESI$^+$) m/z: Calc. for $C_{41}H_{39}FN$ 582.2972 Found $(M + H)^+$ 582.2964

References:

(1) Zheng, Q.; He, G. S.; Lu, C.; Prasad, P. N. Synthesis, Two- and Three-Photon Absorption, and Optical Limiting Properties of Fluorene-Containing Ferrocene Derivatives. J. Mater. Chem. **2005**, 15 (34), 3488. https://doi.org/10.1039/b508005c.

2. Supplementary figures

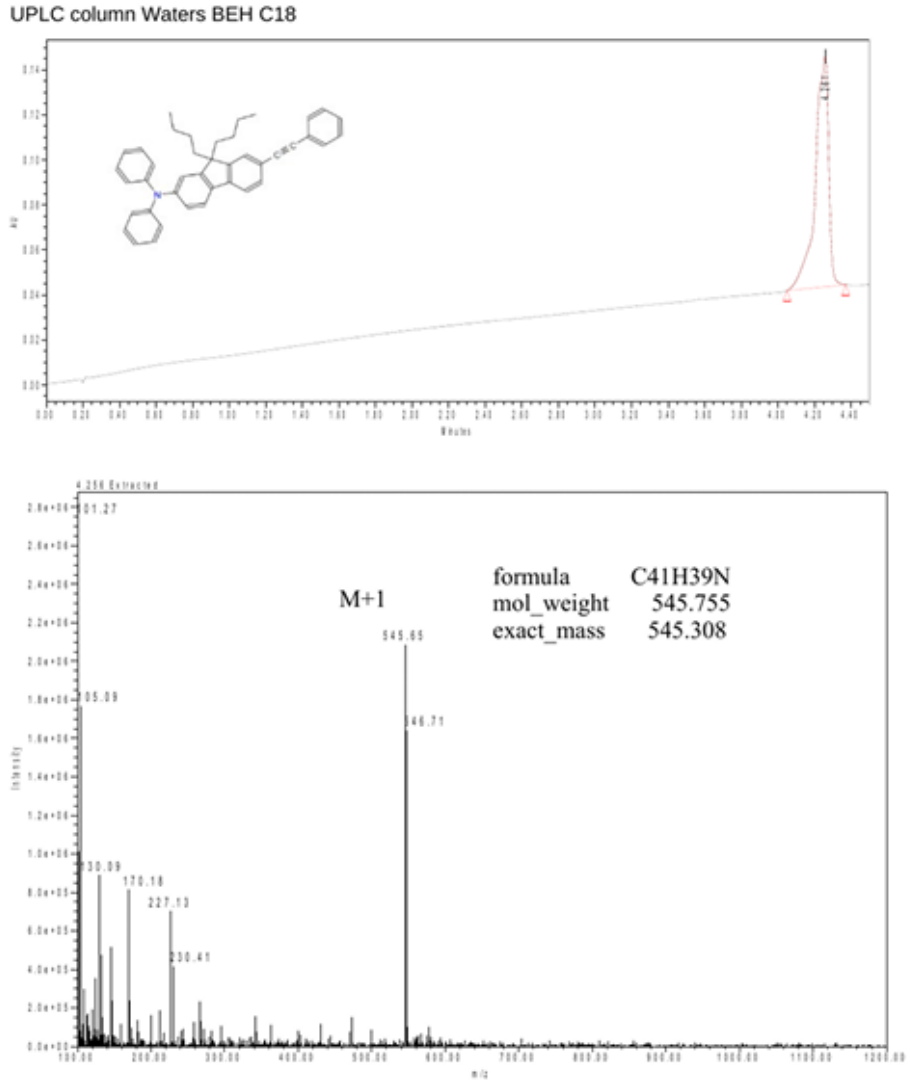

Figure S1 LC-MS analysis of **M-Ph**

Single Mass Analysis
Tolerance = 5.0 PPM / DBE: min = -1.5, max = 60.0
Element prediction: Off
Number of isotope peaks used for i-FIT = 9

Monoisotopic Mass, Even Electron Ions
144 formula(e) evaluated with 1 results within limits (all results (up to 1000) for each mass)
Elements Used:
C: 0-60 H: 0-70 N: 0-5 F: 0-3

240709_5415_posB 16 (0.177) Cm (13:16-54:56)

TOF MS ES+
2.20e+006

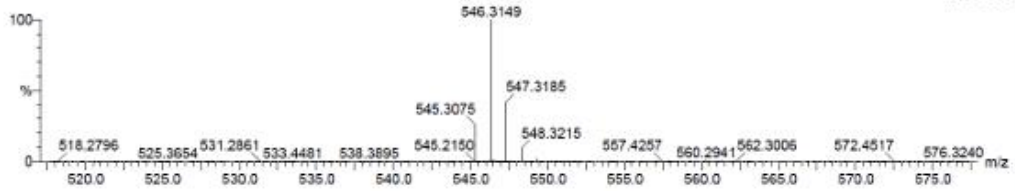

Minimum:				-1.5				
Maximum:		5.0	5.0	60.0				
Mass	Calc. Mass	mDa	PPM	DBE	i-FIT	Norm	Conf(%)	Formula
546.3149	546.3161	-1.2	-2.2	22.5	1358.9	n/a	n/a	C41 H40 N

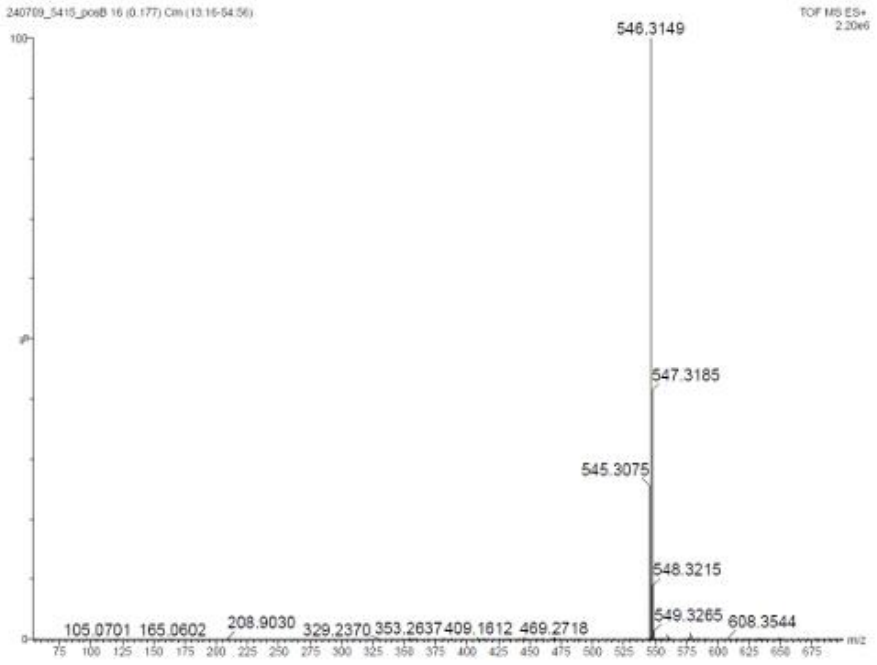

Figure S2 HRMS data of **M-Ph**

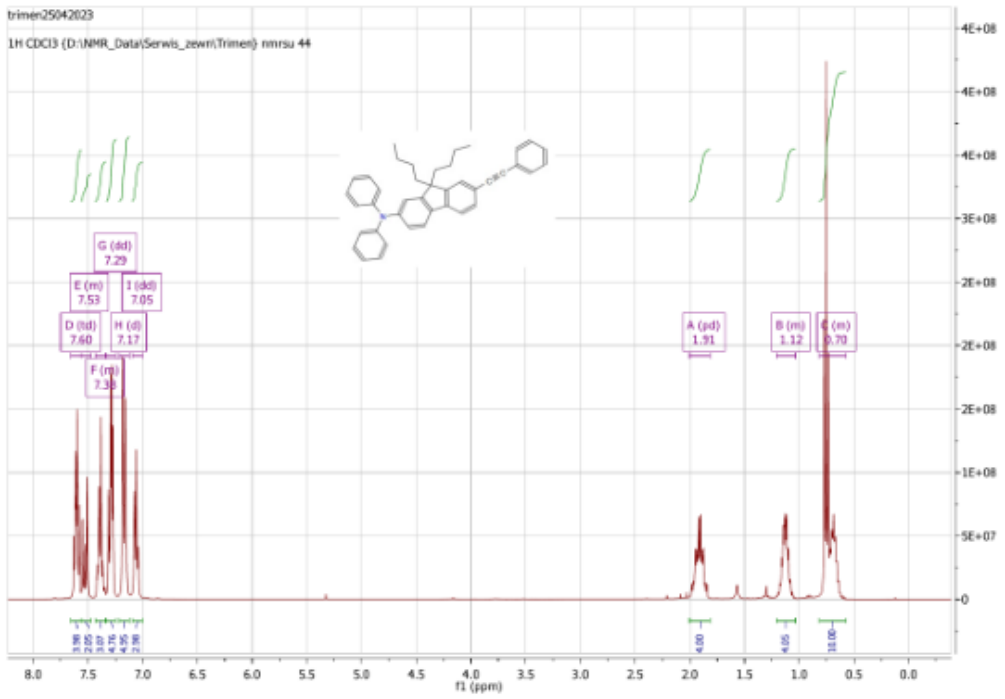

Figure S3 ^{1}H NMR spectrum of **M-Ph** in $CDCl_3$

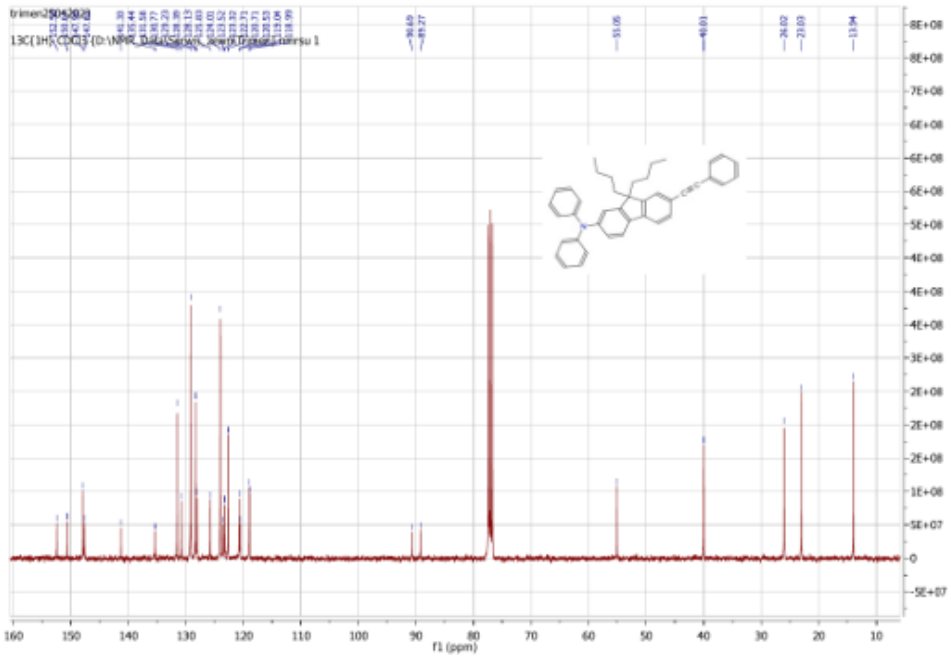

Figure S4 $^{13}C\{^{1}H\}$ NMR spectrum of **M-Ph** in $CDCl_3$

UPLC column Kinetex biphenyl

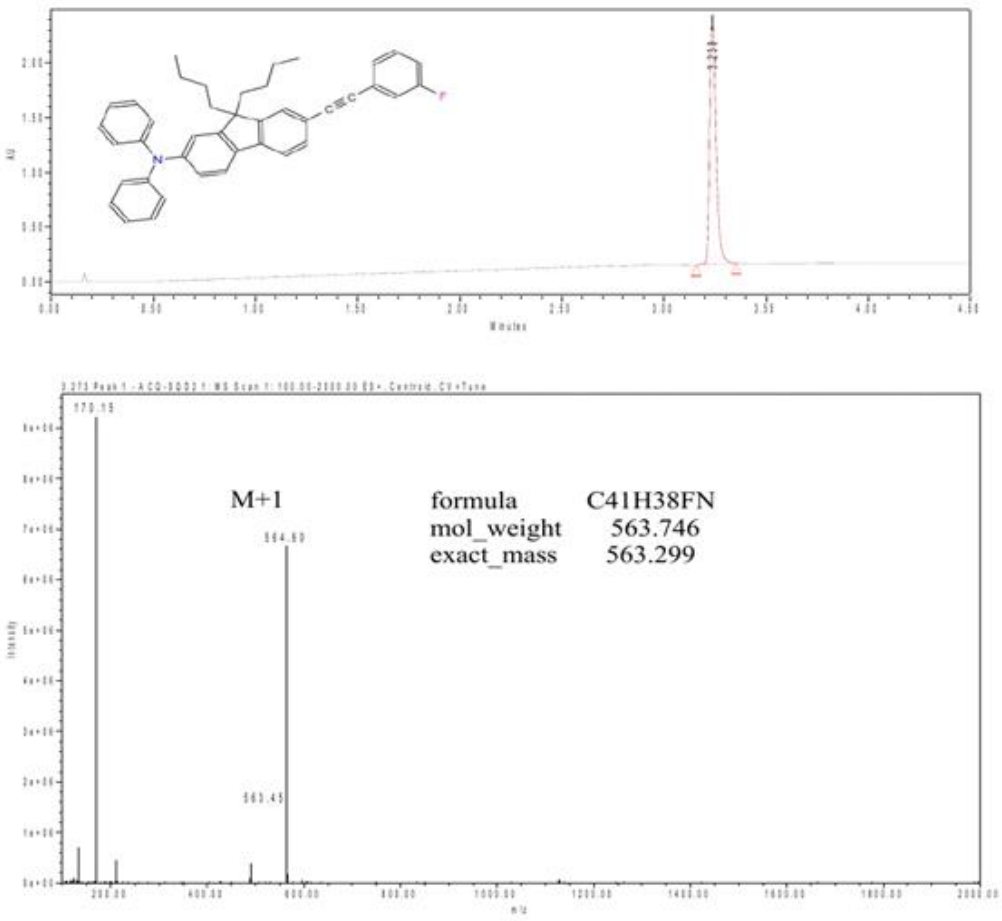

Figure S5 LC-MS analysis of **M-*meta*-F**

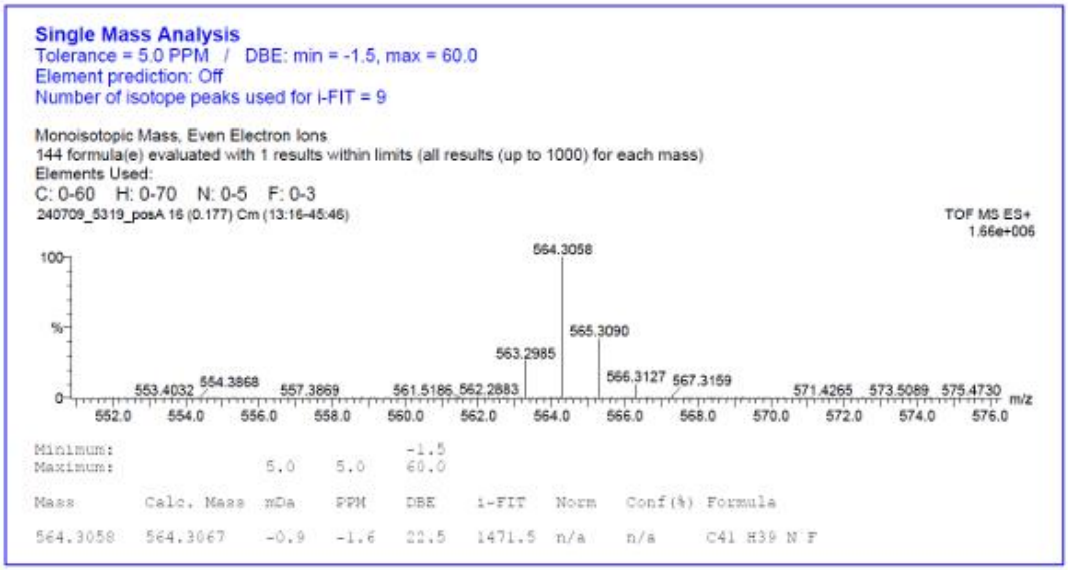

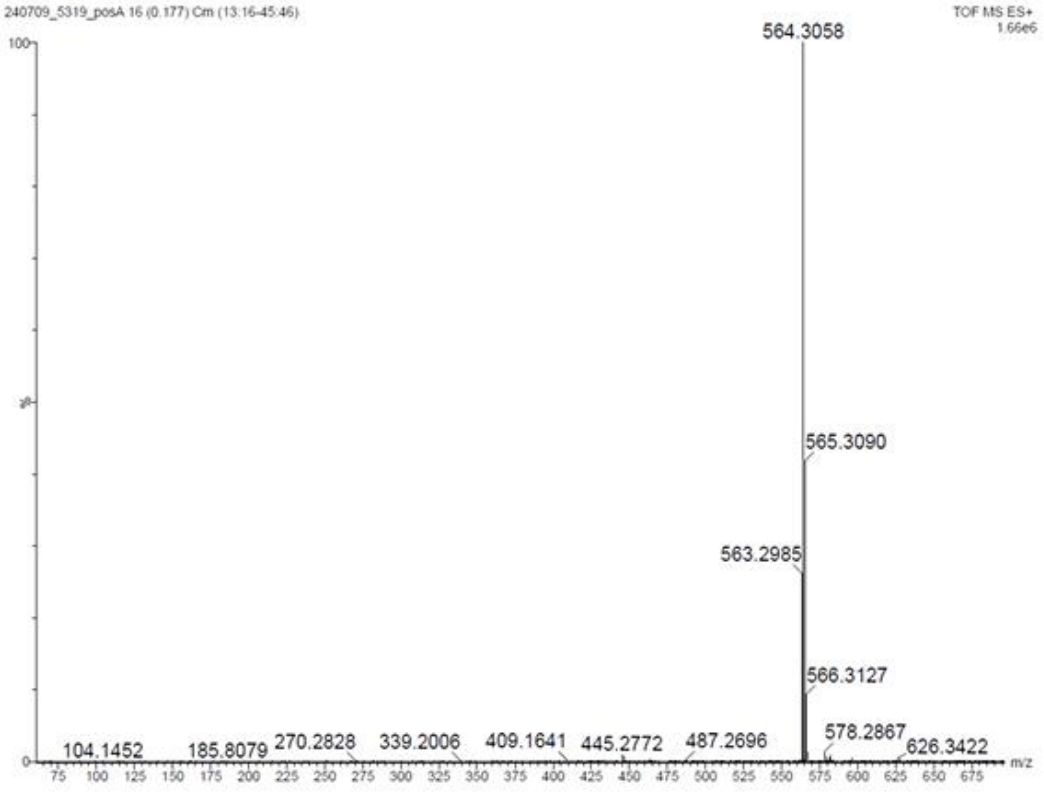

Figure S6 HRMS data for **M-*meta*-F**

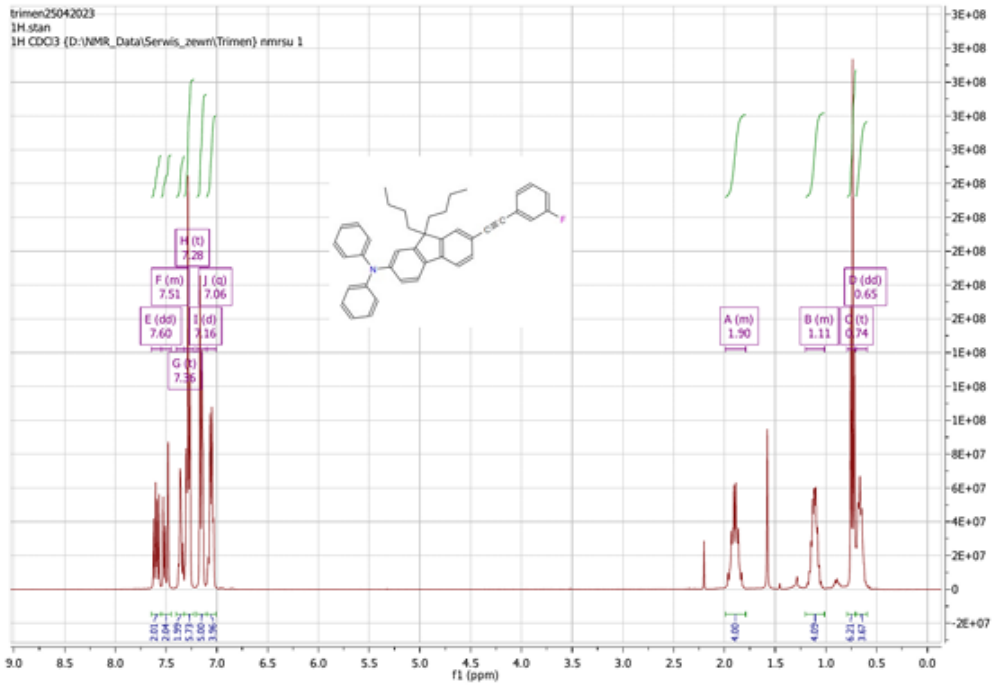

Figure S7 ^{1}H NMR spectrum of **M-*meta*-F** in $CDCl_3$

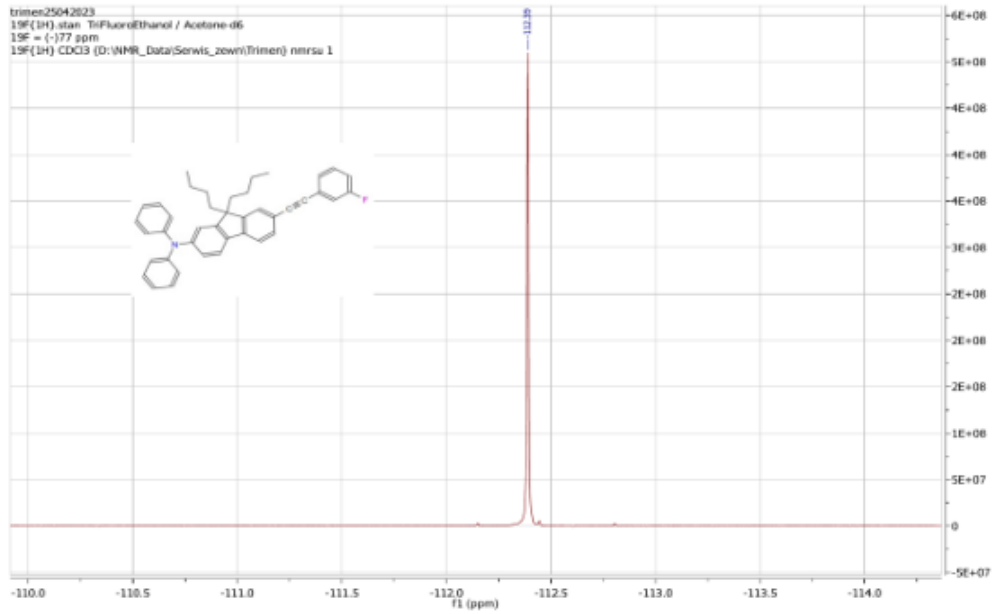

Figure S8 ^{19}F NMR spectrum of **M-*meta*-F** in $CDCl_3$

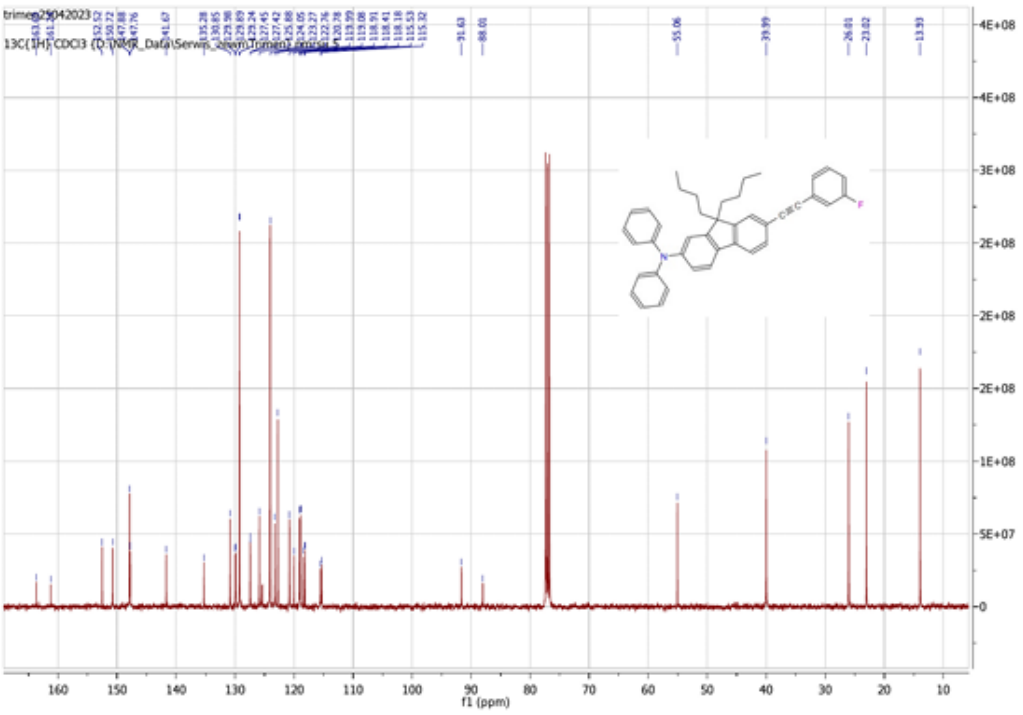

Figure S9 $^{13}C\{^{1}H\}$ NMR spectrum of **M-*meta*-F** in $CDCl_3$

UPLC column Kinetex biphenyl

UV

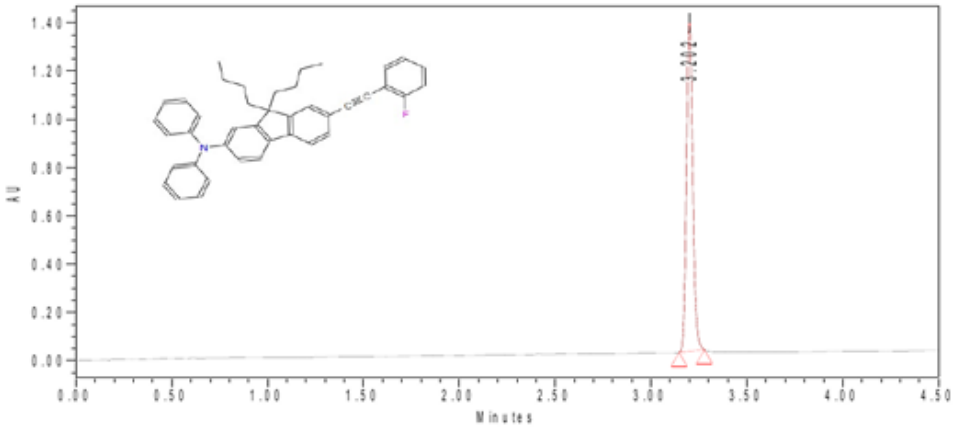

ES+

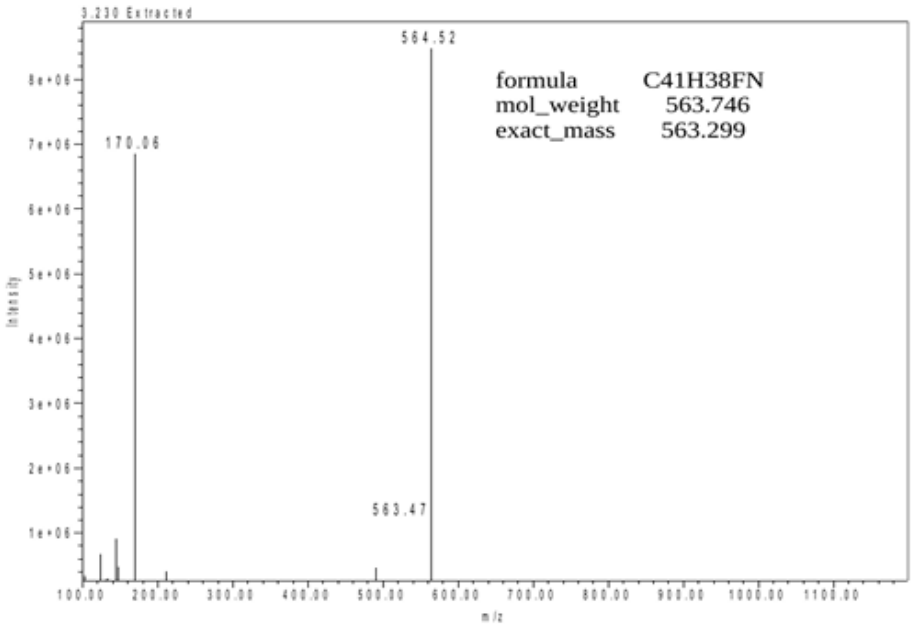

Figure S10 LC-MS analysis of **M-*ortho*-F**

Single Mass Analysis
Tolerance = 5.0 PPM / DBE: min = -1.5, max = 60.0
Element prediction: Off
Number of isotope peaks used for i-FIT = 9

Monoisotopic Mass, Even Electron Ions
144 formula(e) evaluated with 1 results within limits (all results (up to 1000) for each mass)
Elements Used:
C: 0-60 H: 0-70 N: 0-5 F: 0-3

240709_5308_posB 16 (0.177) Cm (14:16-62:64)

TOF MS ES+
3.13e+006

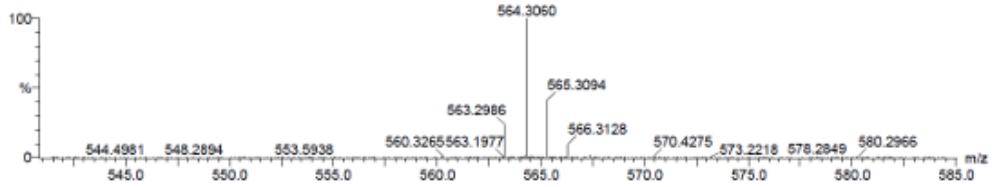

Minimum:				-1.5				
Maximum:		5.0	5.0	60.0				
Mass	Calc. Mass	mDa	PPM	DBE	i-FIT	Norm	Conf(%)	Formula
564.3060	564.3067	-0.7	-1.2	22.5	1199.1	n/a	n/a	C41 H39 N F

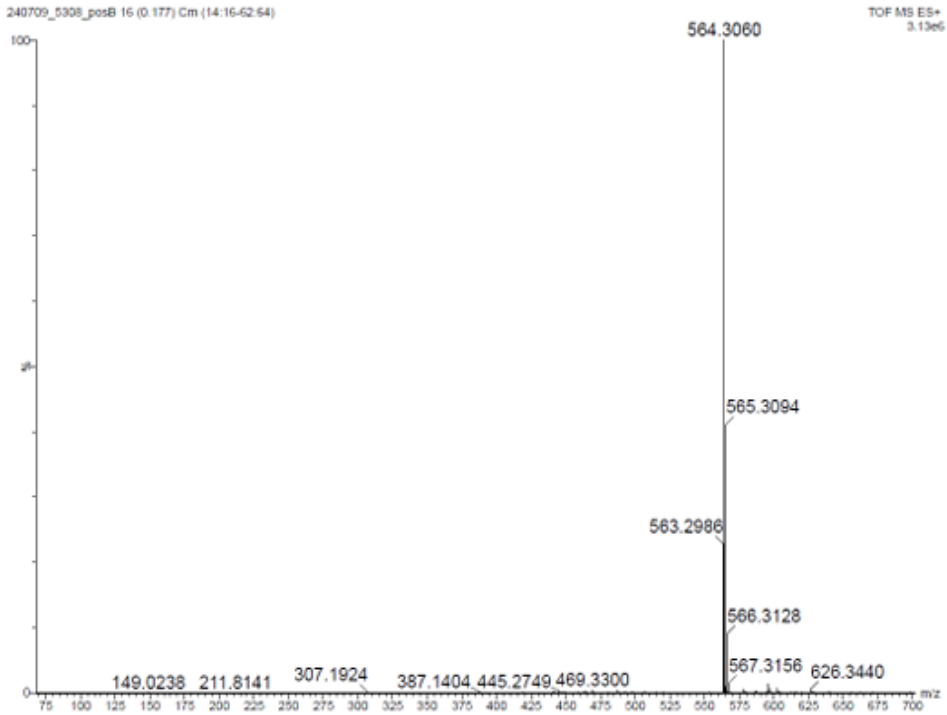

Figure S11 HRMS data for **M-*ortho*-F**

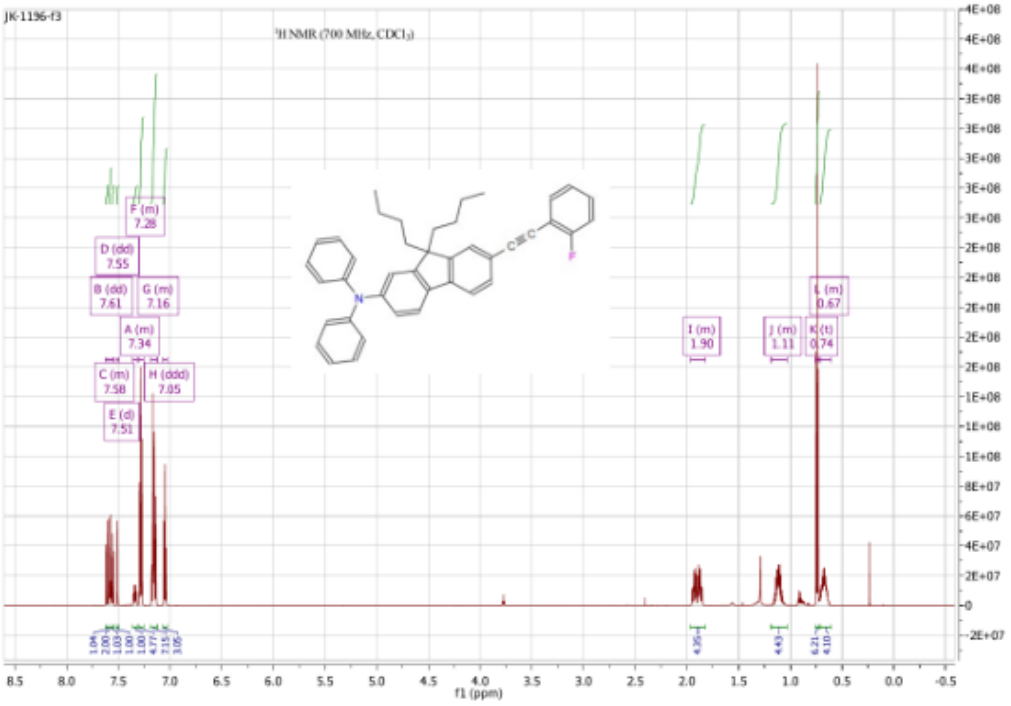

Figure S12 ^{1}H NMR spectrum of **M-*ortho*-F** in $CDCl_3$

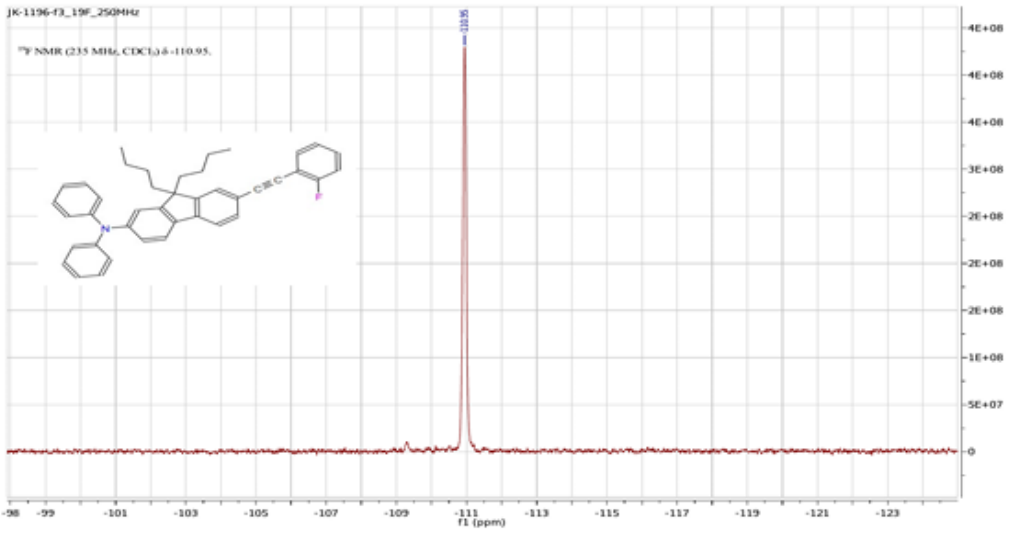

Figure S13 ^{19}F NMR spectrum of **M-*ortho*-F** in $CDCl_3$

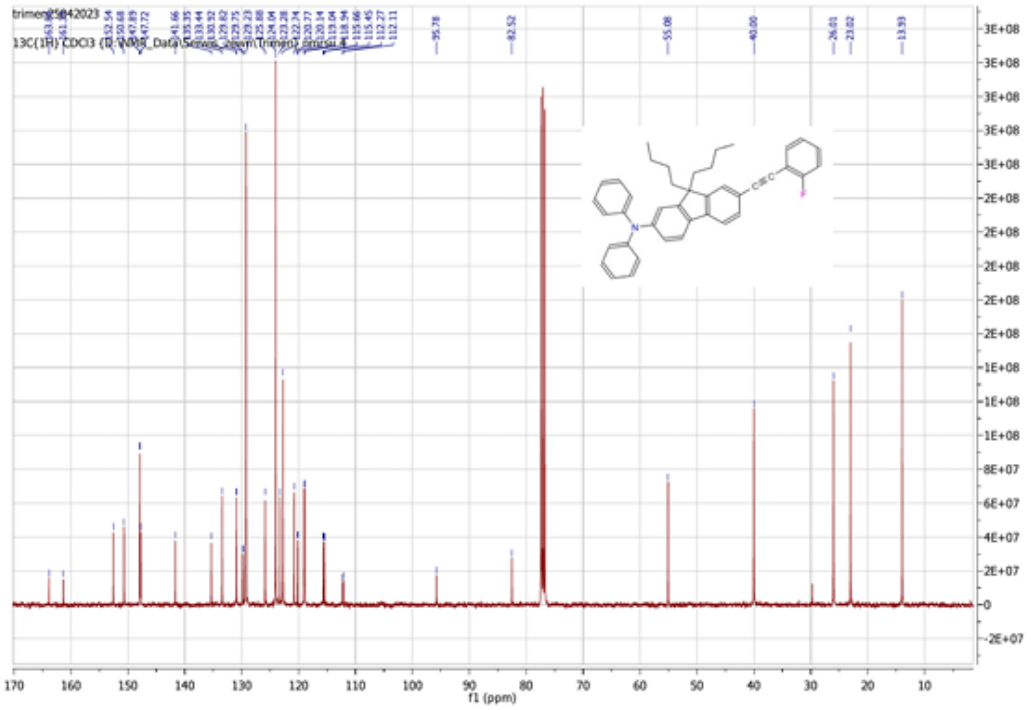

Figure S14 $^{13}C\{^{1}H\}$ NMR spectrum of **M-*ortho*-F** in $CFCl_3$

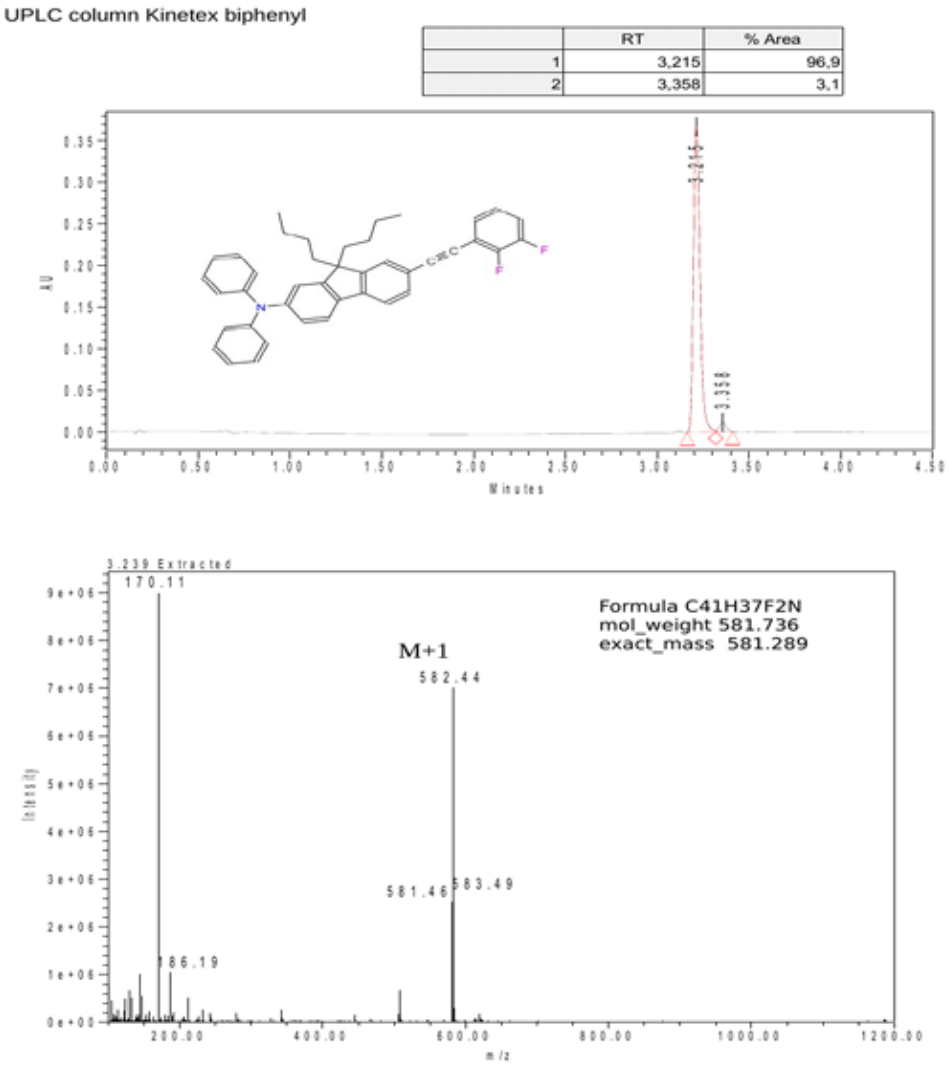

Figure S15 LC-MS analysis of **M-2F**

Single Mass Analysis
Tolerance = 5.0 PPM / DBE: min = -1.5, max = 60.0
Element prediction: Off
Number of isotope peaks used for i-FIT = 9

Monoisotopic Mass, Even Electron Ions
144 formula(e) evaluated with 1 results within limits (all results (up to 1000) for each mass)
Elements Used:
C: 0-60 H: 0-70 N: 0-5 F: 0-3
240709_5318_posB 16 (0.177) Cm (13:16-58:61)

TOF MS ES+
2.33e+006

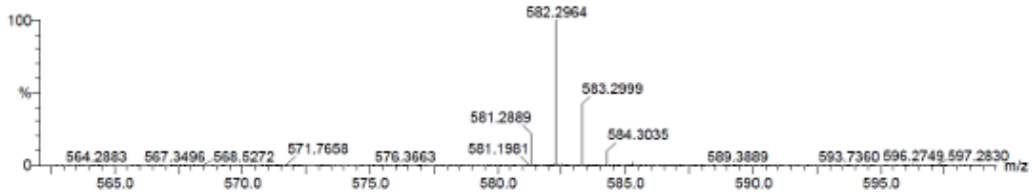

Minimum:				-1.5				
Maximum:		5.0	5.0	60.0				
Mass	Calc. Mass	mDa	PPM	DBE	i-FIT	Norm	Conf(%)	Formula
582.2964	582.2972	-0.8	-1.4	22.5	1344.6	n/a	n/a	C41 H38 N F2

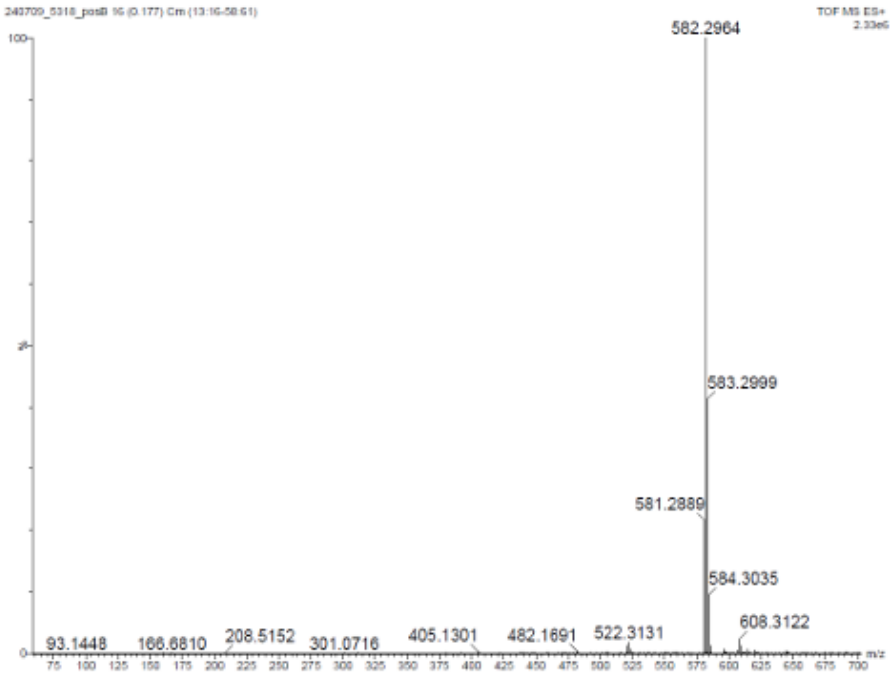

Figure S16 HRMS analysis of **M-*2*F**

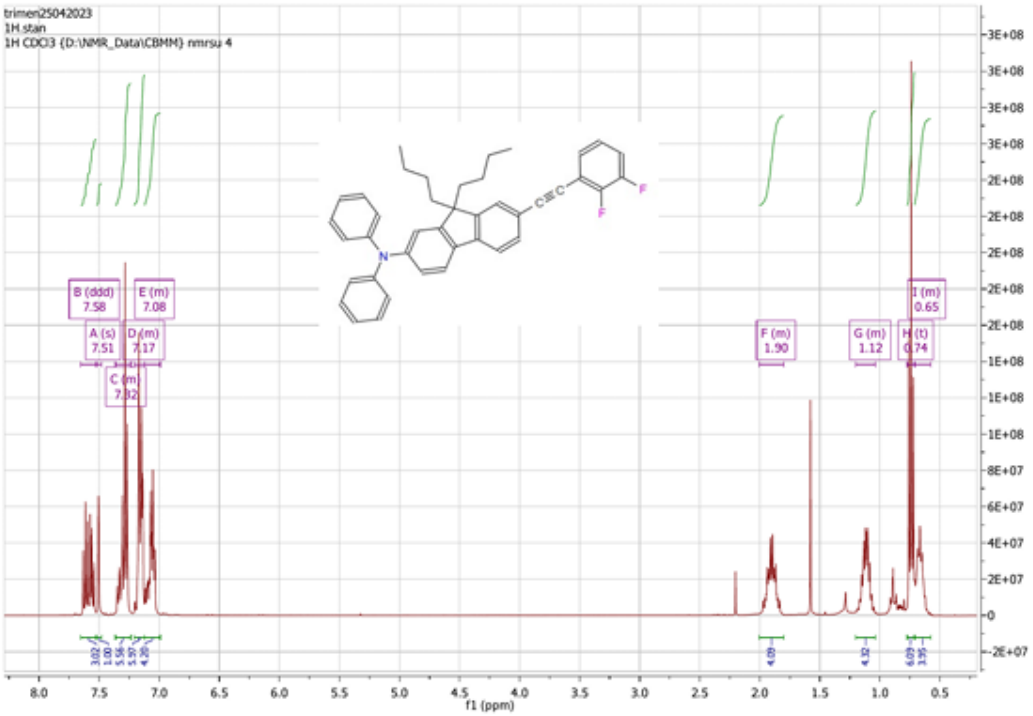

Figure S17 ^{1}H NMR spectrum of **M-*2F*** in $CDCl_3$

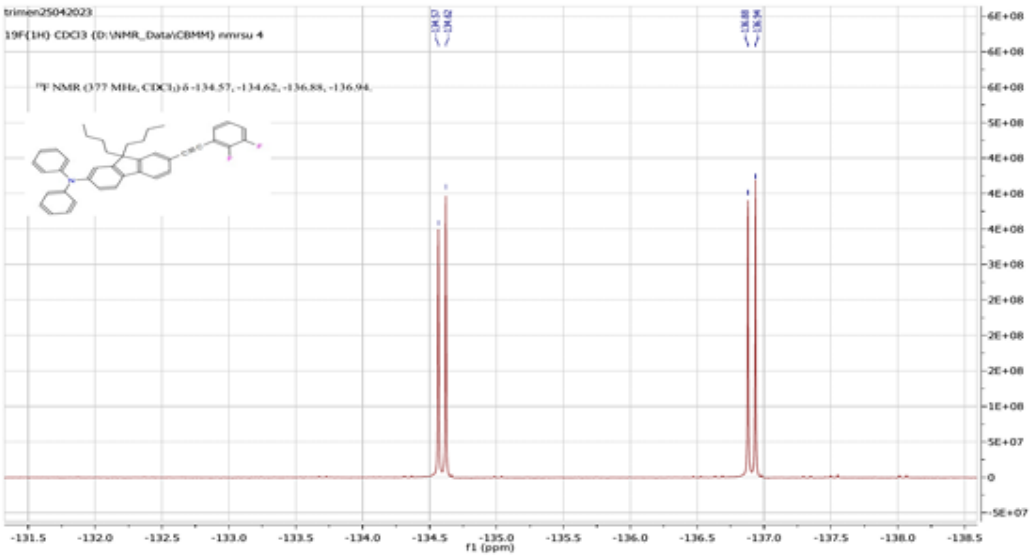

Figure S18 ^{19}F NMR spectrum of **M-*2F*** in $CDCl_3$

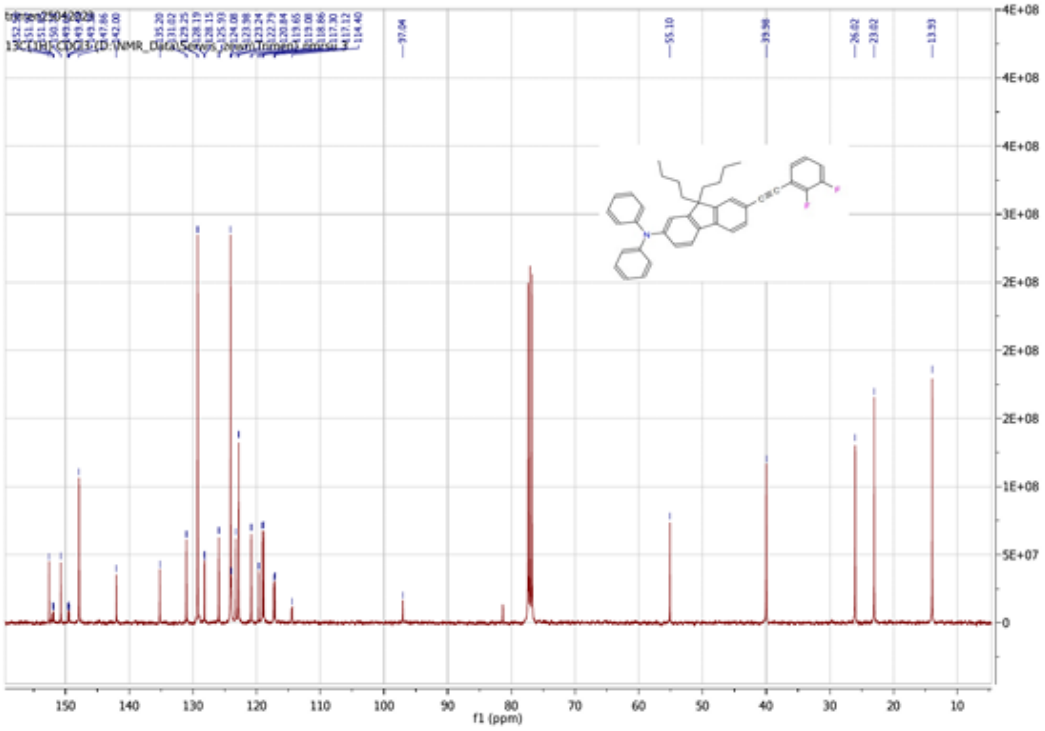

Figure S19 ^{13}C NMR spectrum of **M-*2*F** in $CDCl_3$

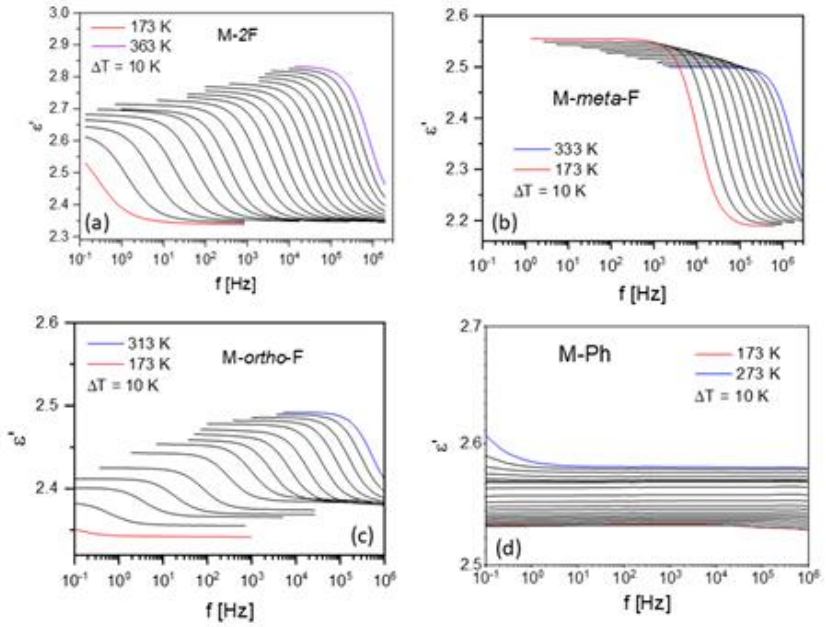

Figure S20 ε'(f) data for sizable crystals with polar rotors (a-c) and for non-polar reference (d)

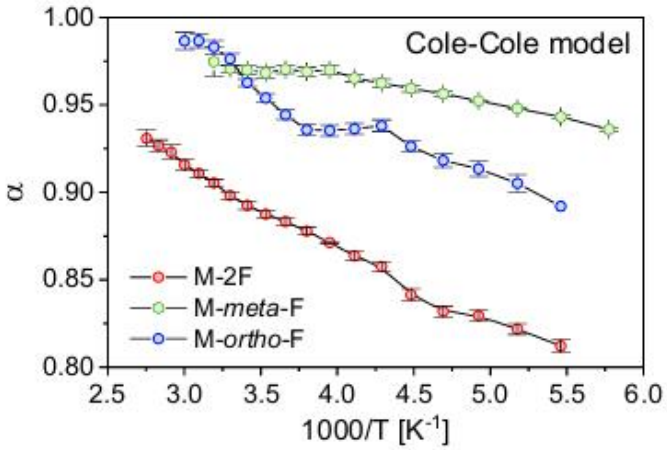

Figure S21 The temperature evolution of shape parameter α from Cole-Cole model for crystals showing the decreasing value of α on cooling.

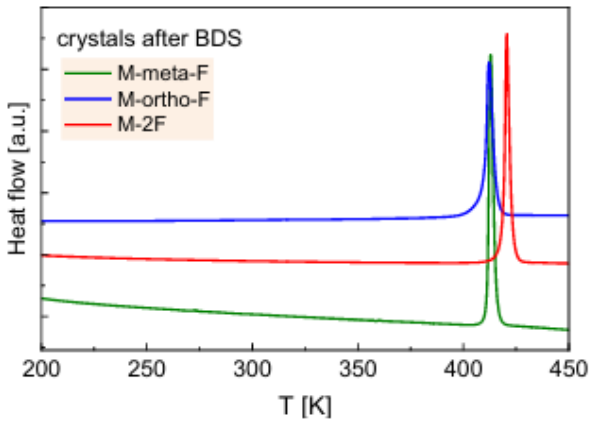

Figure S22 DSC thermograms for samples re-crystalized during BDS experiments measured after BDS data collection. Scans were done from 200 K. Only calorimetric indication for melting was found.

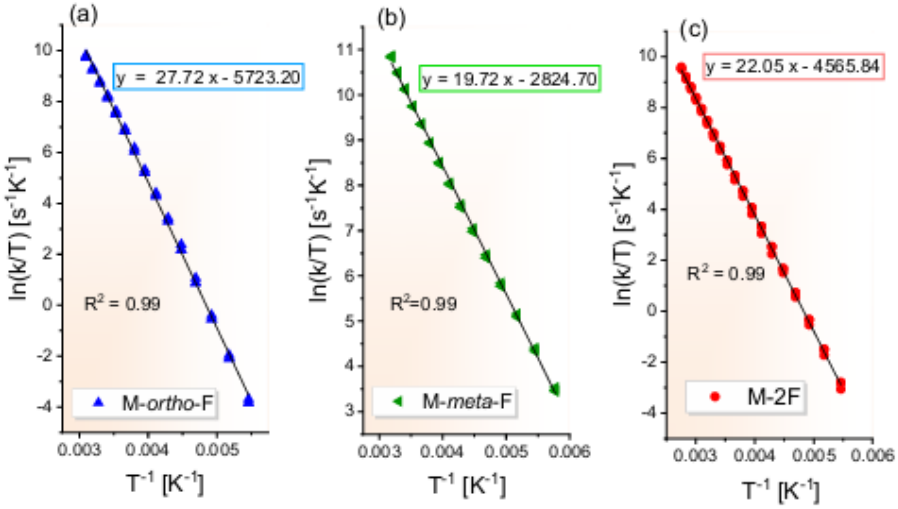

Figure S23 The kinetic data used in Eyring analysis for M-*ortho*-F (a), M-*meta*-F (b), and M-2F (c). Relaxation rates $k = \tau^{-1}$ were determined from dielectric loss spectra for crystalline samples. Symbols correspond to experimental values from three independent experiments. Solid lines are linear fit functions. The slope and y-intercept values are presented.

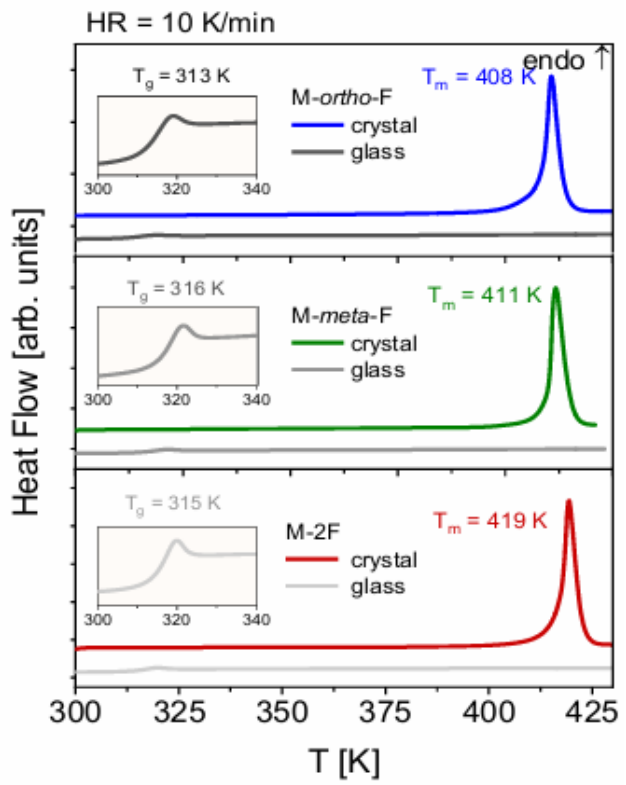

Figure S24 Thermal characterization of glassy and crystalline rotors. DSC scans registered during heating (heating rate HR = 10 K/min) of crystalline and glassy samples revealed a single thermal event corresponding to melting and glass transition, respectively. The inset magnifies the temperature range relevant to the glass transition event. Melting temperature T_m was determined as an onset of the peak, while the glass transition temperature T_g as the midpoint of the heat capacity increment. Thermograms were acquired using a Mettler Toledo DSC1STAR System equipped with a liquid nitrogen cooling accessory and an HSS8 ceramic sensor (a heat flux sensor with 120 thermocouples).

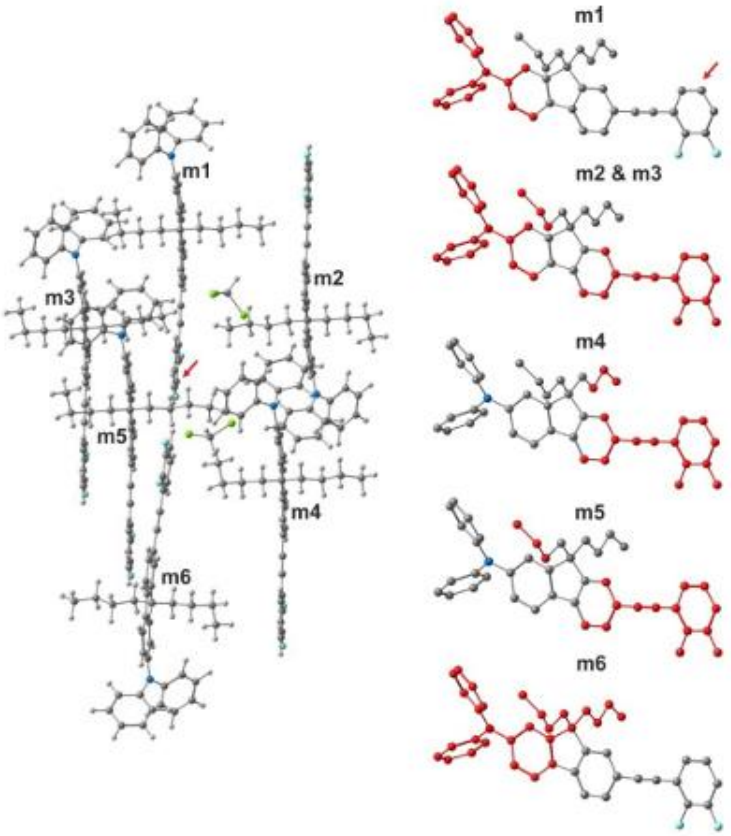

Figure S25 Left panel - the structure of the cluster model obtained from crystallographic data. The presented structure is for the M-2F isomer, analogous structures were isolated for the remaining M-*ortho*-F and M-*meta*-F isomers. Right panel - rules for simplifying the geometry of individual molecules included in the structural cluster model, which was used in the DFT calculations. The atoms marked in red have been removed and the free valencies of carbon atoms have been supplemented by hydrogen atoms. The red arrow marks the selected phenylene group, which is the rotor in the calculations.

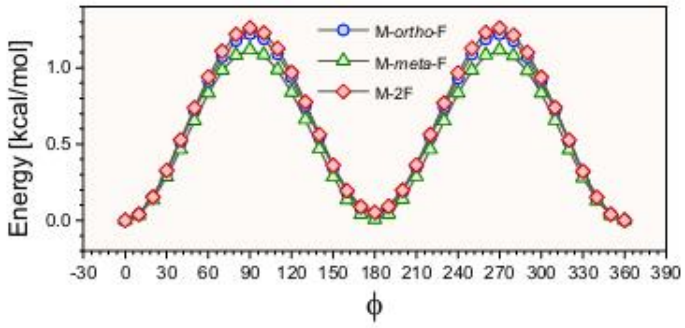

Figure S26 DFT calculated potential for isolated molecules

3. Supplementary Tables

Table S1. List of relaxation time values τ (s) as a function of temperature T (K) for crystalline rotators

M-*ortho*-F crystal						M-*meta*-F crystal						M-2F crystal					
Exp1		Exp2		Exp3		Exp1		Exp2		Exp3		Exp1		Exp2		Exp3	
T	τ	T	τ	T	τ	T	τ	T	τ	T	τ	T	τ	T	τ	T	τ
[K]	[s]	[K]	[s]	[K]	[s]	[K]	[s]	[K]	[s]	[K]	[s]	[K]	[s]	[K]	[s]	[K]	[s]
323.15	1.85E-07	323.15	1.85E-07	323.15	1.69E-07	313.15	6.11E-08	313.15	6.29E-08	313.15	6.36E-08	363.15	2.04E-07	363.15	1.88E-07	363.15	2.00E-07
313.15	3.09E-07	313.15	3.09E-07	313.15	2.86E-07	303.15	9.00E-08	303.15	9.42E-08	303.15	9.31E-08	353.15	3.10E-07	353.15	2.80E-07	353.15	2.88E-07
303.15	5.39E-07	303.15	5.39E-07	303.15	4.98E-07	293.15	1.34E-07	293.15	1.38E-07	293.15	1.39E-07	343.15	4.78E-07	343.15	4.30E-07	343.15	4.36E-07
293.15	9.85E-07	293.15	9.83E-07	293.15	8.96E-07	283.15	2.05E-07	283.15	2.08E-07	283.15	2.08E-07	333.15	7.58E-07	333.15	6.75E-07	333.15	6.82E-07
283.15	1.91E-06	283.15	1.91E-06	283.15	1.71E-06	273.15	3.20E-07	273.15	3.17E-07	273.15	3.16E-07	323.15	1.22E-06	323.15	1.08E-06	323.15	1.09E-06
273.15	3.97E-06	273.15	3.97E-06	273.15	3.52E-06	263.15	5.07E-07	263.15	4.98E-07	263.15	4.94E-07	313.15	2.04E-06	313.15	1.78E-06	313.15	1.79E-06
293.15	9.92E-07	263.15	8.95E-06	263.15	7.86E-06	253.15	8.29E-07	253.15	8.02E-07	253.15	7.98E-07	303.15	3.51E-06	303.15	3.03E-06	303.15	3.01E-06
283.15	1.92E-06	253.15	2.18E-05	253.15	1.93E-05	243.15	1.37E-06	243.15	1.34E-06	243.15	1.31E-06	293.15	6.15E-06	293.15	5.26E-06	293.15	5.26E-06
273.15	3.99E-06	243.15	5.69E-05	243.15	5.00E-05	233.15	2.35E-06	233.15	2.33E-06	233.15	2.19E-06	283.15	1.12E-05	283.15	9.46E-06	283.15	9.46E-06
263.15	8.99E-06	233.15	1.57E-04	233.15	1.40E-04	223.15	4.19E-06	223.15	4.16E-06	223.15	3.89E-06	273.15	2.11E-05	273.15	1.76E-05	273.15	1.76E-05
253.15	2.18E-05	223.15	5.07E-04	223.15	4.13E-04	213.15	7.76E-06	213.15	7.79E-06	213.15	7.24E-06	263.15	4.15E-05	263.15	3.38E-05	263.15	3.36E-05
243.15	5.67E-05	213.15	0.00196	213.15	0.00162	203.15	1.52E-05	203.15	1.53E-05	203.15	1.42E-05	253.15	8.68E-05	253.15	6.81E-05	253.15	6.75E-05
233.15	1.56E-04	203.15	0.00846	203.15	0.00734	193.15	3.10E-05	193.15	3.18E-05	193.15	2.97E-05	243.15	1.93E-04	243.15	1.47E-04	243.15	1.47E-04
223.15	5.07E-04	193.15	0.04173	193.15	0.03649	183.15	6.93E-05	183.15	7.16E-05	183.15	6.65E-05	233.15	4.51E-04	233.15	3.41E-04	233.15	3.39E-04
213.15	0.00195	183.15	0.2534	183.15	0.2167	173.15	1.81E-04	173.15	1.82E-04	173.15	1.69E-04	223.15	9.85E-04	223.15	8.43E-04	223.15	8.36E-04
203.15	0.00843											213.15	0.00269	213.15	0.00228	213.15	0.00226
193.15	0.04146											203.15	0.00838	203.15	0.00684	203.15	0.00684
183.15	0.2513											193.15	0.02899	193.15	0.02312	193.15	0.02297
												183.15	0.1155	183.15	0.08963	183.15	0.08935

Table S2. List of relaxation time values τ (s) as a function of temperature T (K) for glassy samples

M-*ortho*-F glass											
Exp1				Exp2				Exp3			
β		γ		β		γ		β		γ	
T [K]	τ[s]	T [K]	τ[s]	T [K]	τ[s]	T [K]	τ[s]	T [K]	τ[s]	T [K]	τ[s]
154.15	0.6806	154.15	1.63E-04	253.15	2.18E-07	223.15	6.35E-07	153.15	0.3624	153.15	1.51E-04
163.15	0.0827	163.15	4.40E-05	243.15	4.08E-07	213.15	1.01E-06	163.15	0.07841	163.15	3.96E-05
173.15	0.00954	173.15	1.35E-05	233.15	8.07E-07	203.15	1.36E-06	173.15	0.01165	173.15	1.39E-05
183.15	0.00114	183.15	5.39E-06	223.15	3.08E-06	193.15	2.50E-06	183.15	0.00195	183.15	5.95E-06
193.15	2.04E-04	193.15	2.63E-06	213.15	8.62E-06	183.15	4.79E-06	193.15	2.65E-04	193.15	2.61E-06
203.15	3.36E-05	203.15	1.54E-06	203.15	4.63E-05	173.15	1.29E-05	203.15	2.33E-05	203.15	2.05E-06
213.15	7.74E-06	213.15	9.79E-07	193.15	2.97E-04	163.15	3.97E-05	213.15	6.94E-06	213.15	1.05E-06
223.15	2.75E-06	223.15	5.96E-07	183.15	0.0018	153.15	2.13E-04	223.15	1.80E-06	223.15	9.67E-07
233.15	6.98E-07			173.15	0.01533			233.15	6.05E-07		
243.15	3.05E-07			163.15	0.1241			243.15	2.86E-07		
253.15	7.18E-08			153.15	1.316			253.15	1.47E-07		
M-*meta*-F glass											
Exp1				Exp2				Exp3			
β		γ		β		γ		β		γ	
T [K]	τ[s]	T [K]	τ[s]	T [K]	τ[s]	T [K]	τ[s]	T [K]	τ[s]	T [K]	τ[s]
163.15	0.03598	163.15	3.58E-05	213.15	6.94E-06	213.15	4.20E-07	213.15	9.55E-06	213.15	4.13E-07
173.15	0.00286	173.15	1.10E-05	203.15	2.54E-05	203.15	7.96E-07	203.15	2.08E-05	203.15	8.33E-07
183.15	3.66E-04	183.15	4.12E-06	193.15	5.20E-05	193.15	1.82E-06	193.15	8.50E-05	193.15	1.68E-06
193.15	6.80E-05	193.15	1.76E-06	183.15	3.66E-04	183.15	3.70E-06	183.15	5.41E-04	183.15	3.67E-06
203.15	2.07E-05	203.15	9.19E-07	173.15	0.00441	173.15	1.08E-05	173.15	0.00313	173.15	9.80E-06
213.15	7.17E-06	213.15	4.45E-07	163.15	0.0306	163.15	3.69E-05	163.15	0.03657	163.15	4.03E-05
				153.15	0.2923	153.15	1.52E-04	153.15	0.2539	153.15	1.57E-04
M-2F glass											
Exp1				Exp2				Exp3			

β		γ		β		γ		β		γ	
T [K]	τ[s]	T [K]	τ[s]	T [K]	τ[s]	T [K]	τ[s]	T [K]	τ[s]	T [K]	τ[s]
153.15	5.379	153.15	5.75E-04	213.15	1.86E-04	213.15	1.76E-06	213.15	1.39E-04	213.15	2.22E-06
158.15	3.289	158.15	3.86E-04	208.15	4.47E-04	208.15	2.44E-06	208.15	4.03E-04	208.15	2.38E-06
163.15	0.8895	163.15	1.26E-04	203.15	9.94E-04	203.15	3.38E-06	203.15	8.63E-04	203.15	3.42E-06
168.15	0.3216	168.15	7.13E-05	198.15	0.00223	198.15	4.50E-06	198.15	0.00206	198.15	4.61E-06
173.15	0.1269	173.15	4.53E-05	193.15	0.00516	193.15	6.71E-06	193.15	0.00508	193.15	6.72E-06
178.15	0.0452	178.15	2.38E-05	188.15	0.01176	188.15	9.92E-06	188.15	0.01138	188.15	9.67E-06
183.15	0.01699	183.15	1.61E-05	183.15	0.02927	183.15	1.51E-05	183.15	0.02058	183.15	1.39E-05
188.15	0.00813	188.15	1.18E-05	178.15	0.06378	178.15	2.20E-05	178.15	0.05844	178.15	2.22E-05
193.15	0.00276	193.15	7.63E-06	173.15	0.1633	173.15	3.76E-05	173.15	0.1369	173.15	3.48E-05
198.15	0.00132	198.15	5.16E-06	168.15	0.3553	168.15	5.79E-05	168.15	0.3012	168.15	5.39E-05
203.15	5.15E-04	203.15	3.79E-06	163.15	1.033	163.15	1.25E-04	163.15	0.7057	163.15	9.33E-05
208.15	2.36E-04	208.15	2.81E-06	158.15	2.236	158.15	2.16E-04	158.15	2.234	158.15	2.15E-04
213.15	1.43E-04	213.15	1.86E-06	153.15	5.983	153.15	6.69E-04	153.15	5.156	153.15	6.83E-04
M-Ph glass											
Exp1				Exp2				Exp3			
β		γ		β		γ		β		γ	
T [K]	τ[s]	T [K]	τ[s]	T [K]	τ[s]	T [K]	τ[s]	T [K]	τ[s]	T [K]	τ[s]
		143.15	4.57E-05			183.15	8.93E-07			183.15	9.91E-07
		148.15	2.28E-05			178.15	1.31E-06			178.15	1.32E-06
		153.15	1.23E-05			173.15	1.81E-06			173.15	1.86E-06
		158.15	7.44E-06			168.15	2.66E-06			168.15	2.75E-06
		163.15	4.32E-06			163.15	3.99E-06			163.15	4.03E-06
		168.15	2.81E-06			158.15	6.59E-06			158.15	6.71E-06
		173.15	1.72E-06			153.15	1.11E-05			153.15	1.11E-05
		178.15	1.11E-06			148.15	2.01E-05			148.15	1.93E-05
		183.15	7.40E-07			143.15	3.98E-05			143.15	3.52E-05

Table S3. Crystallographic data for M-*ortho*-F, M-*meta*-F and M-2F.

	M-*ortho*-F	**M-*meta*-F**	**M-2F**
CCDC number	2259776	2259777	2259778
Empirical formula	$C_{42}H_{40}Cl_2FN$	$C_{42}H_{40}Cl_2FN$	$C_{42}H_{39}Cl_2F_2N$
Formula weight	648.65	648.65	666.64
Temperature [K]	100		
Wavelength [Å]	0.71073		
Crystal system	Triclinic		
Space group	P-1		
Unit cell dimensions			
a [Å]	10.2978(12)	10.2028(4)	10.4518(3)
b [Å]	13.059(2)	13.0827(4)	13.0746(4)
c [Å]	13.941(3)	14.0212(5)	13.8290(5)
α [°]	74.923(14)	76.360(3)	74.578(3)
β [°]	84.309(12)	81.060(3)	83.388(3)
γ [°]	69.161(12)	69.155(3)	68.750(3)
Volume [$Å^3$]	1691.9(5)	1694.45(11)	1697.50(10)
Z	2		
Density (calculated) [Mg/m^3]	1.273	1.271	1.304
Absorption coefficient [mm^{-1}]	0.229	0.228	0.234
F(000)	684	684	700
Theta range for data collection [°]	3.320 to 36.089	3.145 to 36.527	3.057 to 36.449
Index ranges	$-16 \le h \le 16, -20 \le k \le 11, -22 \le l \le 22$	$-16 \le h \le 16, -18 \le k \le 21, -22 \le l \le 21$	$-17 \le h \le 12, -21 \le k \le 21, -22 \le l \le 22$
Reflection collected	24988	26311	26301
Independent reflections	14532 [R(int) = 0.0821]	15060 [R(int) = 0.0363]	15164 [R(int) = 0.0439]
Completeness to theta = 25.242° [%]	99.8	99.8	99.8
Refinement method	Full-matrix least-squares on F^2		
Data / restraints / parameters	14532 / 0 / 427	15060 / 6 / 455	15164 / 0 / 434
Goodness-of-fit on F^2	0.986	1.018	1.037
Final R indices [I>2σ(I)]	R1 = 0.0879, wR2 = 0.1812	R1 = 0.0626, wR2 = 0.1412	R1 = 0.0702, wR2 = 0.1822
R indices (all data)	R1 = 0.2142, wR2 = 0.2514	R1 = 0.0998, wR2 = 0.1662	R1 = 0.1064, wR2 = 0.2212
Largest diff. peak and hole	0.701 and -0.653	1.022 and -0.768	0.732 and -0.608

Table S4. DFT calculated values of energy barriers ΔE and asymmetries Δ for phenylene ring rotations in the crystalline state.

	I		II		Δ
	ϕ [°]	ΔE_I [kcal/mol]	ϕ [°]	ΔE_{II} [kcal/mol]	$\Delta E_I - \Delta E_{II}$ [kcal/mol]
			M1		
M-2F	60.0	10.3	240.0	8.8	1.5
M-ortho-F	60.0	9.3	240.0	8.2	1.1
M-meta-F	60.0	7.6	240.0	8.7	-1.1
			M2		
M-2F	60.0	9.5	240.0	7.3	2.2
M-ortho-F	60.0	7.8	240.0	7.5	0.3
M-meta-F	60.0	7.7	240.0	7.2	0.5
			M3		
M-2F	60.0	9.9	240.0	9.9	0.0
M-ortho-F	60.0	9.5	240.0	8.6	0.9
M-meta-F	40.0	6.8	240.0	8.8	-2.1

3.2 Artykuł A2

A2. A. Błażytko, M. Rams-Baron, M. Książek, J. Kusz, M. Matussek, J. Grelska & M. Paluch. Engineering of Rotational Dynamics via Polymorph Manipulation. The Journal of Physical Chemistry A, 128, 50 (2024)

Impact Factor z roku opublikowania: 2,7

Punkty ministerialne: 100

DOI: 10.1021/acs.jpca.4c04964

Mój wkład do tego artykułu polegał na przygotowaniu manuskryptu, zaplanowaniu badań, przeprowadzeniu eksperymentów za pomocą spektroskopii dielektrycznej i skaningowej kalorymetrii różnicowej oraz analizie wyników. Oświadczenia o wkładzie pozostałych współautorów zostały zamieszczone podrozdziale 3.4.

THE JOURNAL OF PHYSICAL CHEMISTRY A
A JOURNAL OF THE AMERICAN CHEMICAL SOCIETY

pubs.acs.org/JPCA
Article

Engineering of Rotational Dynamics via Polymorph Manipulation

Alfred Błażytko, Marzena Rams-Baron,* Maria Książek, Joachim Kusz, Marek Matussek, Joanna Grelska, and Marian Paluch

Cite This: J. Phys. Chem. A 2024, 128, 10758−10765
Read Online

ABSTRACT: We used dielectric spectroscopy to uncover the rotational dynamics of the fluorophenyl rotor in different polymorphs of two amphidynamic crystals with identical sizable cores. The rotor solid-state dynamics were investigated in various crystalline environments. We did not change the chemical structure of the crystal itself, but while maintaining the same atomic composition, we changed the arrangement of atoms in space by taking advantage of crystal polymorphism, providing an alternative approach to one based on searching for new, chemically different entities with desirable functionality. We demonstrated that via polymorph variation, we can efficiently improve rotor solid-state performance and reduce the rotational barrier height by 30%. Our findings advance the understanding of polymorph engineering as a prospective trend in amphidynamic crystal technology, which uses the phenomenon of crystal polymorphism to design crystals displaying applicable internal rotational dynamics.

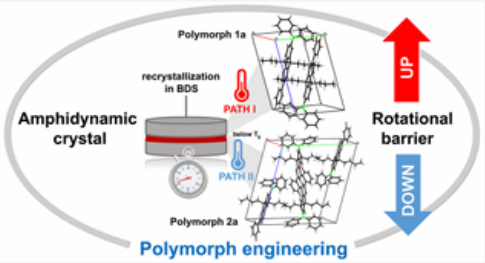

INTRODUCTION

Molecular machines are increasingly attracting the attention of scientists and engineers, as their research and design contribute to the development of innovative materials with applications in various scientific and technological fields.[1−4] One of the most rapidly developed types of molecular machines are molecular rotors, which are characterized by their ability to perform intramolecular rotational motions.[4−6]

In general, molecular rotation is a phenomenon involving the rotation of a molecule or a fragment of a molecule around its center of mass. Various molecular factors can affect the rotational behavior, including the molecular mass, shape of the molecule, or inter- and intramolecular interactions.[7−9] In addition, the rotational image will vary notably depending on the state of matter. For instance, in the liquid phase, molecules have a lot of freedom to perform rotational motion with the time scale of relaxation times reaching nanoseconds.[10−12] Liquid rotational dynamics are strongly temperature-dependent, so as the temperature decreases, a slowdown in molecular dynamics is observed. In some cases, it is possible to supercool the liquid and smoothly enter a disordered glassy state. In a glass, the whole molecule's motion reaches a laboratory-inaccessible time scale. Still, the mobility of molecular fragments can be experimentally observed (if the structure of the molecule and its environment allows it).[13] In other cases, liquid cooling can lead to crystal formation, where the mobility of molecules is precluded by a highly dense and well-ordered environment. Exceptions include plastic crystals, in which the centers of mass of the molecules are stationary, but the molecules can perform rotational movements.[7,12] Another exception is the so-called amphidynamic crystals. In such structures, the static part of the molecule (the stator) remains trapped in the crystal structure, while the mobile fragment (the rotor) exhibits some rotational freedom to perform rotary motions.[14−16]

The key direction of research on amphidynamic crystals and the first step to create new paradigms in molecular rotor engineering is identifying relationships between the crystal structure and the rotational barrier height. Up to now, researchers' efforts toward designing optimal rotational behavior have focused on examining newly synthesized compounds. An alternative unexplored area is to use polymorphic engineering for this purpose. It is unclear to what extent small changes in the arrangement of atoms in different polymorphs of one compound can affect the rotor performance. As such, crystal polymorphism in rotor engineering has not been fully utilized.

The leading and widely used technique in the study of rotation in crystals is nuclear magnetic resonance (NMR); this technique has some limitations, including a relatively small range of available relaxation times (about five decades).[17−21]

Received: July 24, 2024
Revised: November 13, 2024
Accepted: November 19, 2024
Published: December 5, 2024

https://doi.org/10.1021/acs.jpca.4c04964
J. Phys. Chem. A 2024, 128, 10758−10765

An alternative, increasingly used in polar rotor research, is broadband dielectric spectroscopy (BDS). It offers a much more comprehensive frequency range of up to 16 decades; thus, molecular mobility can be followed over a wide temperature range.[12,22] For an intriguing class of amphidynamic crystals with polar rotors, the BDS method is an effective and convenient tool for studying their internal dynamics in a crystalline environment.

Motivated by the lack of general guidelines indicating the role of crystal polymorphism on the rotor's performance in amphidynamic crystals, we used dielectric spectroscopy to investigate the internal rotational dynamics of two amphidynamic crystals with different polymorphs. We used two custom-designed systems containing a large, rigid stator and a fluorophenylene rotor rotating around a single carbon−carbon bond. We observed that depending on the applied crystallization protocol (involving different thermal steps), we could obtain distinct polymorphs of each compound. The combination of XRD and BDS methods allowed us to indicate how the polymorph variation impacts the rotational behavior of the fluorophenylene rotor in different crystal forms of two compounds. We believe that the results presented in this paper will advance the understanding of polymorph engineering as an emerging trend in amphidynamic crystal technology, which uses the phenomenon of crystal polymorphism to design crystals with useful intrinsic rotary dynamics.

Recently, we have proposed a new platform of crystalline molecular rotors with a sizable stator providing sufficient free volume for the solid-state rotation of a fluorophenylene unit.[23] We demonstrated that via internal rotation, the rotor can sample the immediate surroundings with high sensitivity to molecular-level changes that impact the rotation parameters.[23,24] These unique properties are determined by the presence of a fluorine atom, whose small size and electron-withdrawing nature allows for robust interaction with the rotor's surroundings via C−H···F−C contacts. Previously investigated molecules have an acetylene linker between the stator and rotor, allowing fast rotary motion of the fluorophenyl moiety to be achieved in a crystalline environment with a barrier of 25.3 kJ/mol. To realize our concept of obtaining different polymorphs of sizable crystals, here, we replace the previously used acetylene linker with a single bond, which, although it limits the freedom of rotation, allows us to obtain different polymorphs of amphidynamic crystals, which was a central point of the current research. The chemical structure of two investigated molecules, referred to as M-*meta*-F (with 1,3-fluorophenylene rotor) and M-*ortho*-F (with 1,2-fluorophenylene rotor), is shown in Figure 1. These isomers differ only in the position of the fluorine atom in the rotating unit. The fluorophenylene rotor is connected by a single bond to a large, rigid, nonpolar part of a molecule containing diphenylamine and fluorene with long alkyl chains attached.

MATERIALS AND METHODS

Materials. For our study, we used two structural isomers, i.e., M-*meta*-F (*N*-(7-(3-fluorophenyl)-9,9-tetrabutyl-9*H*-fluoren-2-yl)-*N*,*N*-diphenylamine) and M-*ortho*-F ((*N*-(7-(2-fluorophenyl)-9,9-tetrabutyl-9*H*-fluoren-2-yl)-*N*,*N*-diphenylamine). Both molecules were synthesized on request by TriMen Chemicals (Lodz, Poland) with a declared purity of >97%. The molecular mass of these compounds was M = 539.72 g/mol. Their structural formulas are presented in Figure 1a. Chemical characterization (^{1}H NMR, ^{13}C NMR, HRMS spectra) confirming the identity and purity of both compounds is presented in the Supporting Information (Figures S1−S6).

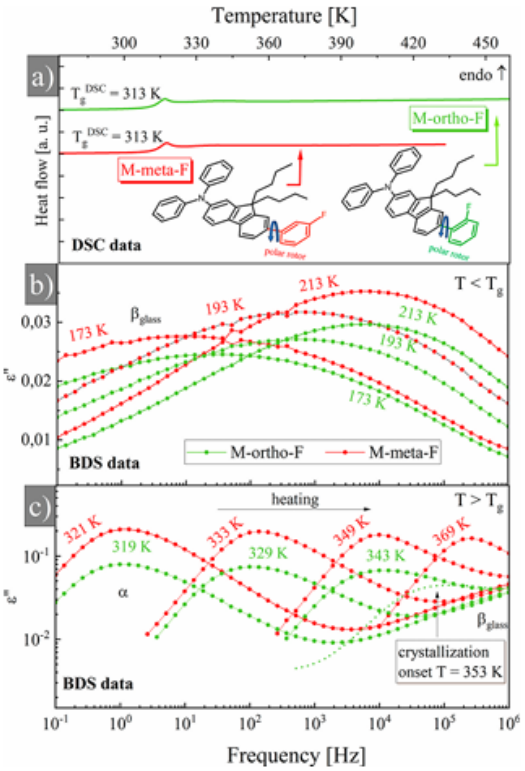

Figure 1. (a) Differential scanning calorimetry (DSC) thermograms measure on heating (10 K/min) of M-*meta*-F (red line) and M-*ortho*-F (green line). The chemical structures of both isomers are presented. Dielectric permittivity spectra $\varepsilon''(f)$ collected for M-*meta*-F (red color) and M-*ortho*-F (green) in the glassy (b) and supercooled liquid (c) states. Symbols denote experimental data while solid lines are fitting functions. A spectrum plotted with a dashed line was partially crystalline.

Differential Scanning Calorimetry. Thermal analysis was performed by using a Mettler-Toledo calorimeter equipped with a ceramic HSS8 sensor (heat flux sensor with 120 thermocouples) and a liquid nitrogen cooling system. Temperature and enthalpy calibrations were performed by using indium and zinc standards. The sample was placed in 40 μL aluminum vessels. Samples in the amorphous and crystalline states were tested at 253−463 K for M-*ortho*-F and 253−433 K for M-*meta*-F with a heating rate of 10 K/min. The melting temperatures were determined from the onset of the process, while the glass transition temperature was assessed from the midpoint of the heat capacity change.

Broadband Dielectric Spectroscopy. We performed dielectric measurements using a Novocontrol GMBH Alpha spectrometer. The Novocool Cryosystem system was responsible for temperature stabilization with an accuracy of 0.2 K. Most of the measurements were carried out in the frequency range from 10^{-1} to 3×10^6 Hz. For temperature-dependent measurements of M-*ortho*-F polymorphs, the range was

https://doi.org/10.1021/acs.jpca.4c04964
J. Phys. Chem. A 2024, 128, 10758−10765

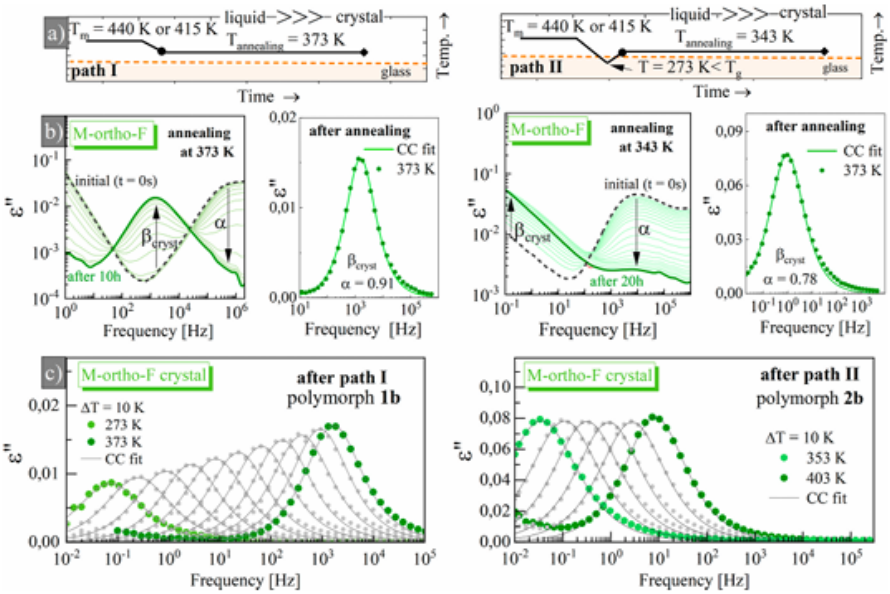

Figure 2. Look horizontally to see the BDS results for representative crystals of M-*ortho*-F after path I (first column) and after path II (second column). (a) Schematic representation of applied recrystallization protocol. (b) (Left panel) the progress of crystallization detected during isothermal annealing for selected polymorph. (Right panel) the effect of Cole−Cole (CC) fitting analysis with the value of corresponding α parameter. (c) Dielectric loss spectra collected for recrystallized samples showing the β_{cryst} processes at different temperatures. Similar data for M-*meta*-F can be found in the Supporting Information.

extended to 1×10^{-2} Hz. The sample in the amorphous state was placed between two stainless steel capacitor plates. A gap of 0.1 mm was provided by silica fibers. Dielectric loss spectra $\varepsilon''(f)$ were measured on heating from 173 to 383 K for M-*meta*-F and from 173 to 359 K for M-*ortho*-F. The temperature step was 5 K for $T < T_g$ and 2 K for $T > T_g$. To obtain crystalline forms of the investigated isomers, we recrystallized samples from the supercooled liquid. Samples annealing at $T_{annealing} > T_g$ was performed directly between the capacitor plates and the dielectric response was monitored as a function of time during this process. To obtain different polymorphic forms, we used two temperature protocols. The first involved heating the substance to T_m (T = 415 K and T = 440 K for M-*meta*-F and M-*ortho*-F, respectively), then cooling to $T_{annealing}$ = 373 K and isothermal recrystallization at this temperature. In contrast, the second protocol involved heating to T_m, cooling to 273 K, and heating to $T_{annealing}$ = 343 K. The obtained crystals were subsequently analyzed as a function of temperature in the range: 273−373 K (M-*ortho*-F polymorph **1b**), 353−403 K (M-*ortho*-F polymorph **2b**), 243−373 K (M-*meta*-F polymorph **1a**), and 203−373 K (M-*meta*-F polymorph **2a**).

Powder X-ray Diffraction. PXRD experiments were performed using a Rigaku-Denki D/MAX/RAPID II-R diffractometer equipped with a rotating silver anode and a two-dimensional image plate detector. The wavelength of the incident beam was 0.5608 Å. The samples were measured in glass capillaries. The two-dimensional diffraction pattern was corrected for background (subtracted empty capillary) and converted to a one-dimensional function of the diffraction intensity vs the scattering angle 2θ. The angular range covered by the experiment was 2−164°, but the range presented in the article was a range of 2−11° characterized by the occurrence of Bragg peaks.

Single-Crystal X-ray Diffraction. The single-crystal X-ray experiments were performed at 100 K. The data were collected using a SuperNova four-circle kappa diffractometer with an Atlas CCD detector (formerly Agilent Technologies, currently Rigaku Oxford Diffraction). For the integration of the collected data, the CrysAlis^{Pro} software was used.[25] The structures were solved using direct methods with the SHELXS-2013 software and the solutions were refined using the SHELXL-2019/2 program.[26] Crystal, data collection, and refinement details for the crystal structures are gathered in Table S2.

■ RESULTS AND DISCUSSION

First, we characterize the thermal properties of M-*meta*-F and M-*ortho*-F using DSC. Both isomers were found to be in the glassy state, as confirmed by the presence of a glass transition, visible as a step change in heat capacity on collected thermograms (Figure 1a). The glass transition temperatures, T_g, determined from the midpoint of heat capacity increment, are the same, i.e., $T_g = 313 \pm 1$ K for M-*meta*-F and M-*ortho*-F. The DSC measurements were performed with a heating rate of 10 K/min; no crystallization was observed under these conditions. Subsequently, the molecular dynamics of both isomers were investigated using the BDS method.

Figure 1b,c shows the representative dielectric loss spectra $\varepsilon''(f)$, collected at different temperatures for samples above and below T_g. In the glassy state (Figure 1b), molecular mobility is determined by secondary relaxations. In general terms, secondary relaxations may reflect the intramolecular dynamics of molecular fragments or the dynamics of an entire molecule. The latter called Johari−Goldstein (JG) relaxations

https://doi.org/10.1021/acs.jpca.4c04964
J. Phys. Chem. A 2024, 128, 10758−10765

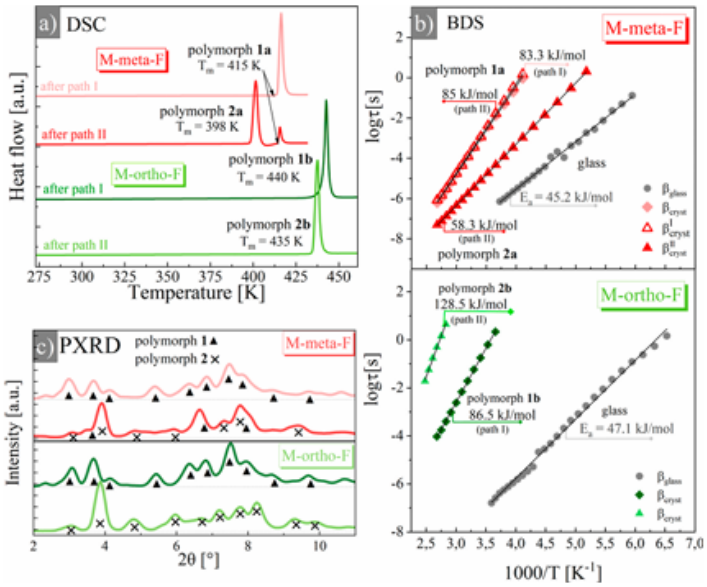

Figure 3. (a) Thermograms obtained on heating of recrystallized samples (10 K/min) obtained using different crystallization protocols (path I and path II) for M-*meta*-F (red lines) and M-*ortho*-F (green lines) isomers. (b) Relaxation map for different polymorphs and glass of M-*meta*-F and M-*ortho*-F. (c) Powder diffraction patterns of samples obtained using crystallization protocols like in diagram (a), symbols mark diffraction peaks which refer to polymorph **1** or **2**.

are frequently discussed as precursors of the cooperative dynamics associated with the glass transition.[27,28] In the case of molecular rotors, intramolecular relaxations are of greatest importance, as the focal point of research is a molecular fragment called the rotor, performing rapid rotations in the environment created by the rest of the molecule. In the studied molecules, internal rotation was accomplished with a fluorophenyl unit. Due to the presence of a fluorine atom, rotor mobility leads to dipole moment changes. Thus, in a glassy state, the rotation of the fluorophenyl unit contributes to the dielectric response as a secondary relaxation mode (non-JG), which we assigned as the β_{glass} process.[29,30] As shown in Figure 1b when the glassy sample is heated, the maximum of the β_{glass} process shifts toward higher frequencies. As the loss peak frequency is inversely related to the relaxation time, such behavior proves that the internal rotation of fluorophenylene units accelerates on heating. When the temperature reaches $T > T_g$, a higher amplitude $\varepsilon''(f)$ peak, α-process, appears on the spectrum (see Figure 1c). It corresponds to the structural relaxation process originating from the cooperative rearrangements of whole molecules and constitutes an intrinsic feature of supercooled liquids dynamics. One can see in Figure 1c that for the M-*ortho*-F at T = 353 K, a significant reduction in the $\varepsilon''(f)$ peak amplitude occurs. It denotes the ongoing crystallization. The drop in $\varepsilon''(f)$ peak amplitude is caused by the partial transformation of supercooled liquid into a crystalline phase where the whole molecule motions responsible for α-process are limited.

The observation of the recrystallization phenomena prompted us to perform time-dependent isothermal dielectric experiments to monitor the crystallization of the investigated isomers in situ. We applied two crystallization protocols intending to produce different polymorphs by cooling the melt to various temperatures. We expected that nucleation at different temperatures (i.e., near T_m and near T_g) would yield different polymorphic forms.[31−35] The overview of the two experimental protocols used in our study is shown in Figure 2a. The applied procedures include the following steps (i) melting the substance at $T = T_m$, cooling to $T_{anealing} > T_g$, (path I) and (ii) melting the substance at $T = T_m$, cooling to $T < T_g$, and subsequent heating to $T_{anealing} > T_g$ (path II). The main difference is the deeper cooling step and additional heating step in path II. The representative dielectric loss spectra $\varepsilon''(f)$ collected during sample annealing for M-*ortho*-F are presented in Figure 2b. Data for M-*meta*-F are shown in Figure S7 in the Supporting Information. The corresponding $\varepsilon'(f)$ data are shown in Figure S8.

As can be seen in Figure 2b, when the crystallization progresses, the α-process gradually disappears. Interestingly, when the crystallization was completed, the collected $\varepsilon''(f)$ spectra were not featureless, which would be expected if all mobile dipoles were frozen in the crystalline lattice. Instead, simultaneously with the disappearance of the α-peak, a new relaxation process appears in the dielectric response; see Figure 2b,c, assigned as β_{cryst}, which indicates that the internal rotation of the fluorophenylene unit is not suppressed in a crystalline state. The same effect was reported before for similar crystals with an acetylene linker.[24] Surprisingly, the pattern of the dielectric response depends on the applied crystallization protocol. For instance, for M-*meta*-F, the bimodal dielectric response was observed after path II, suggesting that a mixture of different polymorphs was formed (see a second column in Figure S7).

To confirm that the applied recrystallization protocols led to various polymorphic forms, we performed DSC measurements to characterize the melting points of the obtained crystals.

https://doi.org/10.1021/acs.jpca.4c04964
J. Phys. Chem. A 2024, 128, 10758−10765

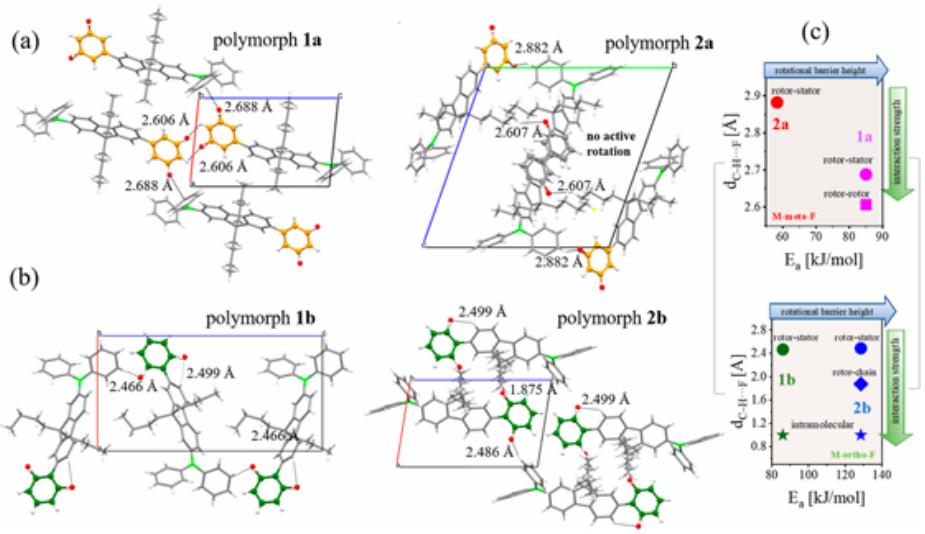

Figure 4. Packing geometry around the rotor with interatomic distances (in Å) for most relevant C−H···F contacts for M-*meta*-F (a) and M-*ortho*-F (b) polymorphs. The fluorophenylene units rotating in the crystalline interior are marked in orange (M-*meta*-F) or green (M-*ortho*-F). The unit cell axes are depicted. (c) Summary of results showing the relationship between the height of the rotational barrier, the number of possible interactions, and the distance between the donor and acceptor in the C−H···F contacts.

Figure 3a presents thermograms obtained on heating of samples recrystallized on a BDS using different protocols. All the curves show an endothermic process associated with crystal melting. For the M-*meta*-F, we identified two polymorphs with $T_m = 415 \pm 1$ K (assigned as polymorph **1a**) and $T_m = 398 \pm 1$ K (polymorph **2a**). The recrystallization procedure according to path I resulted in polymorph **1a**, while path II led to the appearance of a lower melting point polymorph **2a**, which after melting promptly recrystallized to polymorph **1a** when heated at 10 K/min. To demonstrate that polymorph **1a** is not formed postmelting of polymorph **2a** but was formed during thermal annealing in BDS, the sample was heated with a faster heating rate of 30 K/min (see Figure S10). Then, the recrystallization to polymorph **1a** can be avoided and two endothermic processes corresponding to the melting of polymorphs **1a** and **2a** can be distinguished. For the M-*ortho*-F, we obtained polymorph **1b** with $T_m = 440 \pm 1$ K following path I, and a lower melting point polymorph **2b** with $T_m = 435 \pm 1$ K after path II. The structural evidence for the presence of various polymorphs in samples recrystallized using different protocols is given in Figure 3c where PXRD patterns for each recrystallized sample are compared. The diffractograms of M-*meta*-F and M-*ortho*-F show sharp Bragg peaks characterizing the crystalline structures of the investigated samples. Patterns of samples obtained after path I and path II are characterized by clear differences, indicating that we are dealing with different crystalline forms. A closer analysis of the M-*meta*-F crystal obtained via path II confirms that the obtained sample is a mixture of two polymorphs **1a** and **2a**, with the majority of the second. That observation helps to explain the two melting points and bimodal dielectric response.

To probe the rotational dynamics for each crystal, we measured the dielectric loss spectra as a function of the temperature when the recrystallization process was completed. The collected $\varepsilon''(f)$ data are shown in Figures 2c and S7b. One can notice that $\varepsilon''(f)$ spectra collected for crystals are much narrower than those presented in Figure 1b,c. To determine the characteristic relaxation times for internal rotation of the fluorophenyl unit in crystals (β_{cryst} process), we fitted the $\varepsilon''(f)$ spectra depicted in Figures 2c and S7 using a CC function

$$\varepsilon^*(\omega) = \varepsilon_\infty + \frac{\Delta\varepsilon}{1 + (i\omega\tau)^\alpha}$$

where ε_∞ is the high-frequency permittivity, $\Delta\varepsilon$ is the dielectric strength, ω is the angular frequency, τ is the characteristic dielectric relaxation time, and α is a shape parameter which varies from 0 to 1 (for the Debye response with a single relaxation time).[36] For the M-*meta*-F crystal with the bimodal response, we applied two CC functions (see Figure S7a, second column). For all crystalline samples, the α parameter is close to unity at high T and decreases on cooling, reflecting a departure from the ideal Debye model in terms of peak broadening (see Figure S9). Referring to the nomenclature typical for glass-forming liquids, it is denoted that rotational heterogeneity increases as the temperature decreases. In structurally ordered crystals, such effects were linked with the diversity of dipole−dipole interactions in the case of polar rotors,[37] or temperature-dependent crystalline framework motion as was suggested for rotors in the metal−organic frameworks.[38]

The main outcome of CC analysis is presented in Figure 3b where the temperature dependence of characteristic relaxation times is shown. For all crystals, the relaxation times follow the linear Arrhenius relationship, allowing us to compare their rotational dynamic in terms of activation energy[39]

$$\tau = \tau_0 \exp\left(\frac{E_a}{kT}\right)$$

where τ_0 is the pre-exponential factor linked to attempt frequency, E_a is the activation energy, k is Boltzmann's

https://doi.org/10.1021/acs.jpca.4c04964
J. Phys. Chem. A 2024, 128, 10758−10765

constant, and T is the temperature (see Table S1 for fitting parameters). In all cases, the rotation barrier determined for the internal rotation of the fluorophenylene unit in the crystalline state was higher than that in the glassy state. This can be expected due to the lower density and larger free volume of glass compared to its crystalline counterpart. However, such regularity cannot be treated as a strict rule, as we recently showed for a rotor for which the barrier height in the crystal was halved.[24] Here, for the β_{glass} process, the E_a values were E_a = 45.20 ± 0.72 and E_a = 47.1 ± 0.58 kJ/mol for M-*meta*-F and M-*ortho*-F, respectively. For the β_{crys} process, the barrier height for the M-*meta*-F sample recrystallized using path I was equal to 83.32 ± 0.65 kJ/mol (polymorph **1a**). For the sample recrystallized according to path II, which is a mixture of two polymorphs, we obtained two E_a values. For a slower component with a smaller amplitude E_a = 85.00 ± 0.42 kJ/mol, while for a faster higher-amplitude component E_a = 58.26 ± 0.08 kJ/mol. One can note in Figure 3b that relaxation times obtained for polymorph **1a** and those corresponding to a slower component after path II overlap perfectly. Thus, we assigned a relaxation with a smaller amplitude to polymorph **1a** and a faster higher-amplitude component to polymorph **2a**. In the M-*ortho*-F process with E_a = 86.47 ± 0.08 kJ/mol after path I corresponds to polymorph **1b** while this with E_a = 128.49 ± 2.66 kJ/mol observed for the crystal after path II is assigned to polymorph **2b**. These results demonstrated that rotors in crystals obtained using different crystallization protocols revealed various solid-state rotational performances. Depending on the polymorph, the barrier height for the internal rotation of the fluorophenylene unit varied substantially, showing that polymorph variation is an effective approach to tailor the rotor properties in the amphidynamic crystals.

In our experiments, by maintaining the atomic composition in all tested samples and only modifying the packing arrangement, we created optimal conditions to identify the molecular factors determining the barrier height in each case. Single-crystal X-ray diffraction measurements provide precise structural information about each polymorph, which we could compare with BDS results. The crystallization protocols appear to be successful and allow us to grow single crystals of each polymorph suitable for structural analysis. In each sample, for most of the fluorophenyl units rotating in the crystalline interior, we observed that positional disorder and crystal refinement could be done only by assigning a fluorine location at two different sites, as shown in Figure 4 (F atoms are labeled in red) where packing geometry around the rotor and most relevant rotor-stator contacts are depicted (for thermal ellipsoid representation of structures see Figures S11−S14). For M-*meta*-F, polymorph **1a** and polymorph **2a** are packed in the same triclinic system with space group P-1 but the unit cell of polymorph **2a** has twice the volume of polymorph **1a** (see Table S2) and accommodates two molecules in the unit cell. The molecular arrangement and nature of intermolecular contacts vary among polymorphs. In polymorph **1a**, the M-*meta*-F molecules have an arrangement allowing both rotor−stator ($d_{C-H\cdots F}$ = 2.688 Å) and rotor−rotor ($d_{C-H\cdots F}$ = 2.606 Å) interactions, see Figure 4a. Regardless of the position of the rotating fluorine, the geometry of rotor surroundings allows the creation of C−H···F contacts with neighboring molecules, hindering the rotor's mobility. In polymorph **2a**, the situation is more complex. In the unit cell, we have two molecules in which the rotor is located in different packing surroundings. The first population of rotor molecules can interact with the alkyl chains ($d_{C-H\cdots F}$ = 2.607 Å), and in this case, no positional disorder for the fluorine location was found. It denotes that rotor mobility remains suppressed in a crystalline lattice. The second population of rotor molecules interacts with one of the phenylamine rings, but the strength of interactions is weaker than in polymorph **1a** due to the larger distance between interacting atoms ($d_{C-H\cdots F}$ = 2.882 Å). During rotation, such contacts can be avoided at some fluorine locations as structures related to 180° rotation are not equivalent in terms of their ability to create rotor−stator contacts. Consequently, the internal rotation in polymorph **2a** occurs with a lower barrier height.

For M-*ortho*-F, following path I, polymorph **1b** was created with an orthorhombic unit cell and space group $P2_12_12_1$; path II resulted in polymorph **2b** with a triclinic structure. Polymorph **1b** has a unit cell volume two times larger than polymorph **2b** (see Table S2 for details). Smaller rotational barriers had rotors moving in crystals with a larger volume of a unit cell; the same is true for M-*meta*-F polymorphs. The higher rotational barriers observed for M-*ortho*-F polymorphs in comparison to M-*meta*-F are due to the proximity of a fluorine atom to the stator's fluorene unit, which allows the formation of intramolecular rotor−stator contacts, restricting the rotor's mobility. The crystalline packing and pattern of relevant rotor−stator contacts for both polymorphs of M-*ortho*-F are shown in Figure 4b. For polymorph **1b**, in addition to intramolecular C−H···F interactions relevant for both M-*ortho*-F polymorphs (d_{intra} = 2.499 Å), intermolecular C−H···F contacts with one of the diphenylamine rings ($d_{C-H\cdots F}$ = 2.466 Å) affect rotor mobility. For polymorph **2b**, with the highest barrier detected, the molecular packing is different. During rotation, the fluorine atom can interact with one of the diphenylamine rings ($d_{C-H\cdots F}$ = 2.486 Å) but at the same time, the proximity of alkyl chains may hinder rotation, see the right panel in Figure 4b. Refined structures revealed some positional disorder for alkyl chains for polymorph **2b** in M-*ortho*-F. Since the terminal group of one of the alkyl chains can change its position, under certain conditions, a strong rotor-chain contact can emerge (with $d_{C-H\cdots F}$ = 1.875 Å), hindering rotation. Consequently, the largest barrier height discovered for this polymorph reflects the highest number of C−H···F contacts, allowing for developing rotor−stator interactions.

Our efforts to find a molecular justification for barrier height for the investigated fluorophenyl rotor have shown that the main factors are the interactions of fluorine with its immediate environment and differences in the pattern of C−H···F contacts determined by changes in the arrangement of atoms in individual crystal forms. It is apparent that the highest activation energy found for polymorph **2b** in M-*ortho*-F (E_a = 128.49 ± 2.66 kJ/mol) is related to the highest number of C−H···F interactions. The fewer rotor−stator contacts are created and the lower barriers are observed, as in the case of polymorph **2a** in M-*meta*-F with the lowest activation energy found (E_a = 58.26 ± 0.08 kJ/mol) and only one site favoring rotor−stator contacts. As shown in Figure 4c, the rotational barrier height correlates with the donor−acceptor distances of the involved C−H···F contacts. The proximity of the sizable core in the case of the M-*ortho*-F substitution, allowing the intramolecular C−H···F contacts, increased the barrier height compared to the *meta* isomer. The size of the unit cell is also important. For both isomers, the polymorph with lower activation energy had a larger unit cell. These results confirm

https://doi.org/10.1021/acs.jpca.4c04964
J. Phys. Chem. A 2024, 128, 10758−10765

the possibility of adjusting the internal dynamics of rotors via polymorph variation and show that the dynamics of a rotor in the crystalline interior can be effectively adjusted by finding a polymorph with optimal molecular arrangement limiting the possibility of rotor−stator interactions.

CONCLUSIONS

In summary, we designed two molecular rotors with fluorophenylene rotors embedded in sizable crystals using an approach reported previously. By playing with the temperature during the crystallization procedure, we obtained various forms of an amphidynamic crystal, where the rotor moves in distinct packing environments with different patterns of rotor−stator interactions. Finally, we demonstrated that polymorph variation allows for the improvement of rotor properties and a reduction in barrier height by 30%. Our findings demonstrated that exploring the polymorphs of newly tested compounds presents a promising approach to identifying optimal rotational performance. Such polymorph screening can become an integral part of the search for new amphidynamic crystals, as it represents an opportunity to significantly improve rotational properties without synthesizing a new chemical entity.

ASSOCIATED CONTENT

Data Availability Statement

CCDC 2353733−2353736 contain the Supporting Information crystallographic data for this paper. These data can be obtained free of charge from The Cambridge Crystallographic Data Centre via: www.ccdc.cam.ac.uk/data_request/cif.

Supporting Information

The Supporting Information is available free of charge at https://pubs.acs.org/doi/10.1021/acs.jpca.4c04964.

Chemical characterization of M-*meta*-F and M-ortho-F, dielectric investigation of crystallization on BDS, $\varepsilon'(f)$ data illustrating crystallization progress for all polymorphs, analysis of shape parameter α_{CC} as a function of temperature, thermogram of M-*meta*-F with heating rate 30 K/min, structures of all polymorphs in thermal ellipsoid representation, and fitting parameters and structural parameters for single crystals (PDF)

Crystallographic data for all investigated polymorphs (CIF)

AUTHOR INFORMATION

Corresponding Author

Marzena Rams-Baron − *August Chelkowski Institute of Physics, University of Silesia in Katowice, 41-500 Chorzow, Poland;* orcid.org/0000-0001-8808-8067; Email: marzena.rams-baron@us.edu.pl

Authors

Alfred Blażytko − *August Chelkowski Institute of Physics, University of Silesia in Katowice, 41-500 Chorzow, Poland;* orcid.org/0000-0003-4653-0421

Maria Książek − *August Chelkowski Institute of Physics, University of Silesia in Katowice, 41-500 Chorzow, Poland*

Joachim Kusz − *August Chelkowski Institute of Physics, University of Silesia in Katowice, 41-500 Chorzow, Poland*

Marek Matussek − *Institute of Chemistry, University of Silesia in Katowice, 40-006 Katowice, Poland*

Joanna Grelska − *August Chelkowski Institute of Physics, University of Silesia in Katowice, 41-500 Chorzow, Poland;* orcid.org/0000-0002-7001-4083

Marian Paluch − *August Chelkowski Institute of Physics, University of Silesia in Katowice, 41-500 Chorzow, Poland;* orcid.org/0000-0002-7280-8557

Complete contact information is available at: https://pubs.acs.org/10.1021/acs.jpca.4c04964

Author Contributions

A.B. (investigation, methodology, formal analysis, validation, writing−original draft); M. R.-B. (conceptualization, writing−review and editing, funding acquisition); M.K. (investigation); J.K. (investigation); M.M. (chemical characterization); J.G. (investigation); M.P. (conceptualization, supervision, writing−review and editing).

Notes

The authors declare no competing financial interest.

ACKNOWLEDGMENTS

This research was funded as a whole by the National Science Centre, Poland. Project no. 2021/41/B/ST5/00992. For Open Access, the author has applied a CC-BY public copyright license to any Author Accepted Manuscript (AAM) version arising from this submission.

REFERENCES

(1) Leigh, D. A. Die Genese der Nanomaschinen: der Chemie-Nobelpreis 2016. *Angew. Chem.* **2016**, *128* (47), 14722−14724.

(2) Koumura, N.; Zijlstra, R. W. J.; van Delden, R. A.; Harada, N.; Feringa, B. Light-driven monodirectional molecular rotor. *Nature* **1999**, *401*, 152−155.

(3) Fletcher, S. P.; Dumur, F.; Pollard, M. M.; Feringa, B. L. A Reversible, Unidirectional Molecular Rotary Motor Driven by Chemical Energy. *Science* **2005**, *310* (5745), 80−82.

(4) Tierney, H. L.; Murphy, C. J.; Jewell, A. D.; Baber, A. E.; Iski, E. V.; Khodaverdian, H. Y.; McGuire, A. F.; Klebanov, N.; Sykes, E. C. H. Experimental Demonstration of a Single-Molecule Electric Motor. *Nat. Nanotechnol.* **2011**, *6* (10), 625−629.

(5) Perego, J.; Bracco, S.; Negroni, M.; Bezuidenhout, C. X.; Prando, G.; Carretta, P.; Comotti, A.; Sozzani, P. Fast Motion of Molecular Rotors in Metal-Organic Framework Struts at Very Low Temperatures. *Nat. Chem.* **2020**, *12* (9), 845−851.

(6) Horinek, D.; Michl, J. Molecular Dynamics Simulation of an Electric Field Driven Dipolar Molecular Rotor Attached to a Quartz Glass Surface. *J. Am. Chem. Soc.* **2003**, *125* (39), 11900−11910.

(7) Brand, R.; Lunkenheimer, P.; Loidl, A. Relaxations and Fast Dynamics of the Plastic Crystal Cyclo-Octanol investigated by Broadband Dielectric Spectroscopy. *Phys. Rev. B* **1997**, *56* (10), R5713−R5716.

(8) Simpson, G. J.; García-López, V.; Daniel Boese, A.; Tour, J. M.; Grill, L. How to Control Single-Molecule Rotation. *Nat. Commun.* **2019**, *10* (1), 4631.

(9) Karlen, S. D.; Reyes, H.; Taylor, R. E.; Khan, S. I.; Hawthorne, M. F.; Garcia-Garibay, M. A. Symmetry and Dynamics of Molecular Rotors in Amphidynamic Molecular Crystals. *Proc. Natl. Acad. Sci. U.S.A.* **2010**, *107* (34), 14973−14977.

(10) Davies, D. B.; Matheson, A. J. Influence of Molecular Rotation on Some Physical Properties of Liquids. *Discuss. Faraday Soc.* **1967**, *43*, 216−222.

(11) Kim, J. M.; Baig, C. Precise Analysis of Polymer Rotational Dynamics. *Sci. Rep.* **2016**, *6* (1), 19127.

(12) Kremer, F.; Schonhals, A. *Broadband Dielectric Spectroscopy*; Springer: Berlin, Heidelberg, 2003.

(13) Kremer, F.; Loidl, A. *The Scaling of Relaxation Processes*; Springer, 2018.

(14) Vogelsberg, C. S.; Uribe-Romo, F. J.; Lipton, A. S.; Yang, S.; Houk, K. N.; Brown, S.; Garcia-Garibay, M. A. Ultrafast Rotation in an Amphidynamic Crystalline Metal Organic Framework. *Proc. Natl. Acad. Sci. U.S.A.* **2017**, *114* (52), 13613−13618.
(15) Gould, S. L.; Tranchemontagne, D.; Yaghi, O. M.; Garcia-Garibay, M. A. Amphidynamic Character of Crystalline MOF-5: Rotational Dynamics of Terephthalate Phenylenes in a Free-Volume, Sterically Unhindered Environment. *J. Am. Chem. Soc.* **2008**, *130* (11), 3246−3247.
(16) Liepuoniute, I.; Huynh, C. M.; Perez-Estrada, S.; Wang, Y.; Khan, S.; Houk, K. N.; Garcia-Garibay, M. A. Enhanced Rotation by Ground State Destabilization in Amphidynamic Crystals of a Dipolar 2,3-Difluorophenylene Rotator as Established by Solid State 2H NMR and Dielectric Spectroscopy. *J. Phys. Chem. C* **2020**, *124* (28), 15391−15398.
(17) Keeler, J. *Understanding NMR Spectroscopy*, 2nd ed.; John Wiley and Sons: West Sussex, 2010.
(18) Schurko, R. W. Ultra-Wideline Solid-State NMR Spectroscopy. *Acc. Chem. Res.* **2013**, *46* (9), 1985−1995.
(19) Albrand, J. P.; Taieb, M. C.; Fries, P. H.; Belorizky, E. NMR Study of Spectral Densities over a Large Frequency Range for Intermolecular Relaxation in Liquids: Pair Correlation Effects. *J. Chem. Phys.* **1983**, *78* (9), 5809−5815.
(20) Weigler, M.; Brodrecht, M.; Breitzke, H.; Dietrich, F.; Sattig, M.; Buntkowsky, G.; Vogel, M. 2H NMR Studies on Water Dynamics in Functionalized Mesoporous Silica. *Z. Phys. Chem.* **2018**, *232* (7−8), 1041−1058.
(21) Kubicki, D. J.; Stranks, S. D.; Grey, C. P.; Emsley, L. NMR Spectroscopy Probes Microstructure, Dynamics and Doping of Metal Halide Perovskites. *Nat. Rev. Chem* **2021**, *5* (9), 624−645.
(22) Roland, C. M.; Hensel-Bielowka, S.; Paluch, M.; Casalini, R. Supercooled Dynamics of Glass-Forming Liquids and Polymers under Hydrostatic Pressure. *Rep. Prog. Phys.* **2005**, *68* (6), 1405−1478.
(23) Rams-Baron, M.; Błażytko, A.; Jurkiewicz, K.; Lodowski, P.; Książek, M.; Kusz, J.; Mozga, W.; Fordymacka, M.; Teymouri, M.; Krzywik, J.; Paluch, M. Image of the Solid-State Rotary Motion Encoded in the Dielectric Response. *Rep. Prog. Phys.* **2024**, *87* (10), 108002.
(24) Rams-Baron, M.; Błażytko, A.; Książek, M.; Kusz, J.; Paluch, M. Internal Secondary Relaxation as a Dielectric Probe of Molecular Surroundings. *J. Phys. Chem. Lett.* **2024**, *15* (9), 2595−2600.
(25) *Rigaku Oxford Diffraction*, version 1.171.38.41; CrysAlisPro Software System, 2015. https://www.rigaku.com.
(26) Sheldrick, G. M. Crystal Structure Refinement with SHELXL. *Acta Crystallogr., Sect. C:Struct. Chem.* **2015**, *71*, 3−8.
(27) Ngai, K. L.; Paluch, M. Classification of Secondary Relaxation in Glass-Formers Based on Dynamic Properties. *J. Chem. Phys.* **2004**, *120* (2), 857−873.
(28) Ngai, K. L. Johari-Goldstein Secondary Relaxation in Methylated Alkanes. *Phys. Rev. B:Condens. Matter Mater. Phys.* **2005**, *71* (21), 214201.
(29) Błażytko, A.; Rams-Baron, M.; Paluch, M. The Influence of Molecular Shape on Reorientation Dynamics of Sizable Glass-Forming Isomers at Ambient and Elevated Pressure. *Sci. Rep.* **2024**, *14* (1), 887.
(30) Rams-Baron, M.; Yao, B.; Cheng, S.; Dulski, M.; Paluch, M. Complex Reorientation Dynamics of Sizable Glass-Formers with Polar Rotors Revealed by Dielectric Spectroscopy. *J. Phys. Chem. Lett.* **2021**, *12* (46), 11303−11307.
(31) Cruz-Cabeza, A. J.; Reutzel-Edens, S. M.; Bernstein, J. Facts and Fictions about Polymorphism. *Chem. Soc. Rev.* **2015**, *44* (23), 8619−8635.
(32) Llinàs, A.; Goodman, J. M. Polymorph Control: Past, Present and Future. *Drug Discovery Today* **2008**, *13* (5−6), 198−210.
(33) Gui, Y.; Huang, C.; Shi, C.; Stelzer, T.; Zhang, G. G. Z.; Yu, L. Polymorphic Selectivity in Crystal Nucleation. *J. Chem. Phys.* **2022**, *156* (14), 144504.
(34) Bernstein, J. Polymorphism - A Perspective. *Cryst. Growth Des.* **2011**, *11* (3), 632−650.
(35) Andronis, V.; Zografi, G. Crystal Nucleation and Growth of Indomethacin Polymorphs from the Amorphous State. *J. Non-Cryst. Solids* **2000**, *271*, 236−248.
(36) Cole, K. S.; Cole, R. H. Dispersion and Absorption in Dielectrics I. Alternating Current Characteristics. *J. Chem. Phys.* **1941**, *9* (4), 341−351.
(37) Schnabel, J.; Schulz, A.; Lunkenheimer, P.; Volkmer, D. Benzothiadiazole-Based Rotation and Possible Antipolar Order in Carboxylate-Based Metal-Organic Frameworks. *Commun. Chem.* **2023**, *6* (1), 161.
(38) Liu, Z.; Wang, Y.; Garcia-Garibay, M. A. Rotational Dynamics of an Amphidynamic Zirconium Metal-Organic Framework Determined by Dielectric Spectroscopy. *J. Phys. Chem. Lett.* **2021**, *12* (24), 5644−5648.
(39) Cicerone, M. T.; Ediger, M. D. Enhanced Translation of Probe Molecules in Supercooled O-Terphenyl: Signature of Spatially Heterogeneous Dynamics? *J. Chem. Phys.* **1996**, *104* (18), 7210−7218.

https://doi.org/10.1021/acs.jpca.4c04964
J. Phys. Chem. A 2024, 128, 10758−10765

Supporting Information

Engineering of Rotational Dynamics via Polymorph Manipulation

Alfred Błażytko[1], Marzena Rams-Baron[1]*, Maria Książek[1], Joachim Kusz[1], Marek Matussek[2], Joanna Grelska[1], Marian Paluch[1]

[1]*August Chelkowski Institute of Physics, University of Silesia in Katowice, 75 Pulku Piechoty 1, 41- 500 Chorzow, Poland*
[2]*Institute of Chemistry, University of Silesia in Katowice, Szkolna 9, 40-006 Katowice, Poland*
*corresponding author: marzena.rams-baron@us.edu.pl

1. Chemical characterization of compounds

M-meta-F

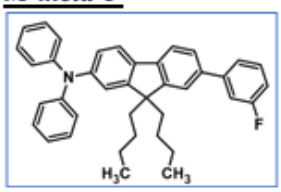

^{1}H NMR (500 MHz, Acetone-d_6) δ: 7.85 – 7.75 (m, 3H), 7.69 (dd, *J* = 7.9, 1.7 Hz, 1H), 7.62 – 7.58 (m, 1H), 7.55 – 7.48 (m, 2H), 7.35 – 7.29 (m, 4H), 7.23 – 7.20 (m, 1H), 7.15 – 7.10 (m, 5H), 7.08 – 7.02 (m, 3H), 2.16 – 1.93 (m, 4H), 1.17 – 1.04 (m, 4H), 0.74 – 0.66 (m, 10H). **^{13}C NMR** (126 MHz, $CDCl_3$) δ: 164.32, 162.37, 152.51, 151.52, 148.05, 147.47, 144.13, 144.07, 140.96, 138.01, 135.73, 130.29, 130.23, 129.28, 126.11, 124.01, 123.52, 122.79, 122.69, 121.31, 120.63, 119.54, 119.32, 114.09, 113.92, 113.89, 113.72, 55.19, 40.11, 26.17, 23.10, 13.99. **HRMS** (ESI): calcd. for $C_{39}H_{38}FN$ [M^+] 539.2988; found 539.2991.

M-ortho-F

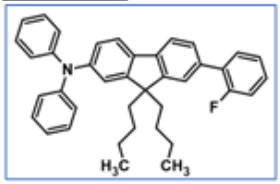

^{1}H NMR (500 MHz, Acetone-d_6) δ: 7.83 (d, *J* = 7.8 Hz, 1H), 7.77 (d, *J* = 8.1 Hz, 1H), 7.65 – 7.55 (m, 3H), 7.46 – 7.39 (m, 1H), 7.35 – 7.24 (m, 6H), 7.23 – 7.20 (m, 1H), 7.14 – 7.02 (m, 7H), 2.00 – 1.92 (m, 4H), 1.16 – 1.07 (m, 4H), 0.75 – 0.68 (m, 10H). **^{13}C NMR** (126 MHz, $CDCl_3$) δ: 160.91, 158.94, 152.54, 150.84, 148.06, 147.34, 140.56, 135.91, 133.73, 130.86, 130.84, 129.75, 129.65, 129.24, 128.71, 128.65, 127.86, 127.84, 124.40, 124.37, 123.95, 123.54, 123.52, 123.49, 122.61, 120.56, 119.36, 119.10, 116.31, 116.12, 55.12, 39.99, 26.14, 23.07, 13.95. **HRMS** (ESI): calcd. for $C_{39}H_{38}FN$ [M^+] 539.2988; found 539.2991.

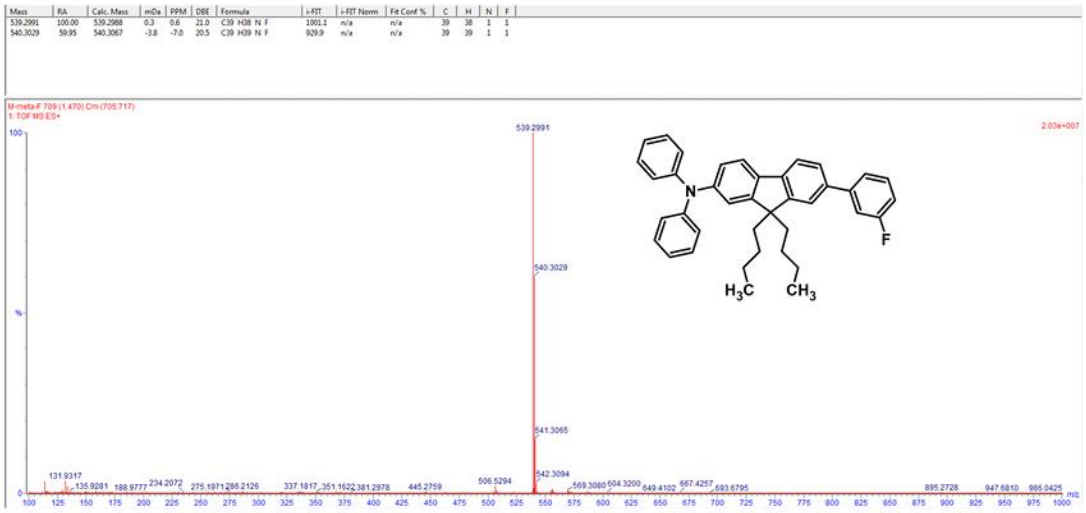

Figure S1: HRMS spectrum of M-meta-F

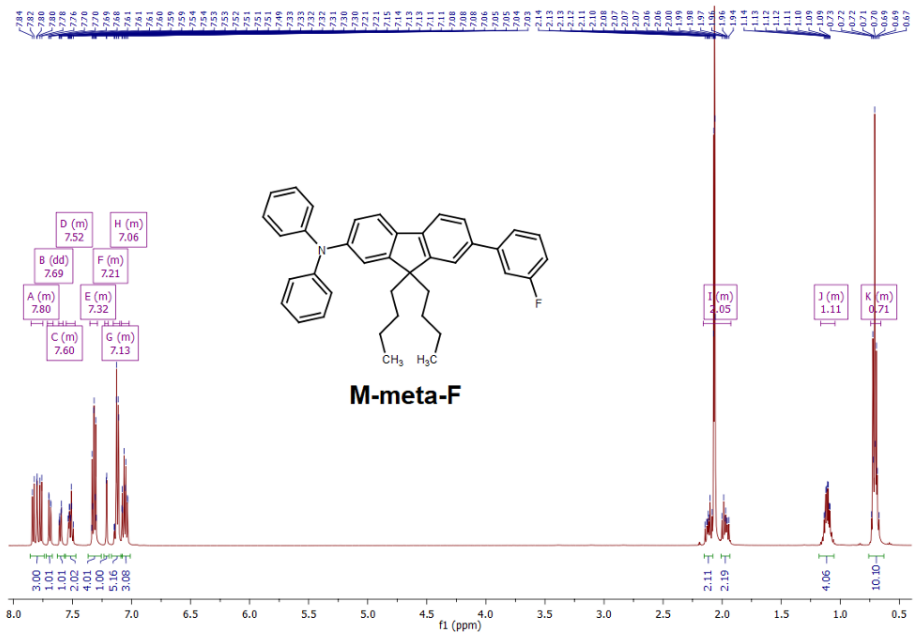

Figure S2: ^{1}H NMR spectrum of M-meta-F

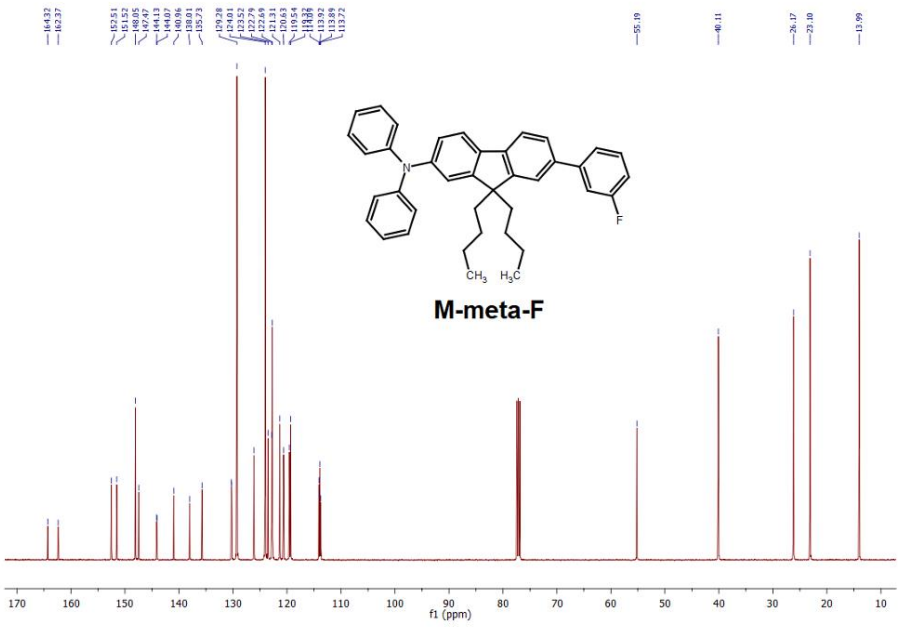

Figure S3: ^{13}C NMR spectrum of M-meta-F

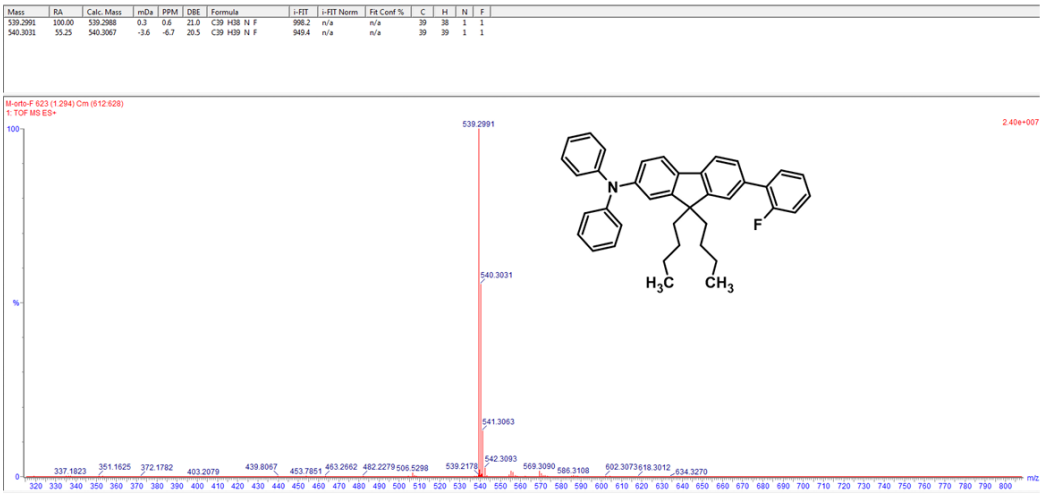

Figure S4: HRMS spectrum of M-ortho-F

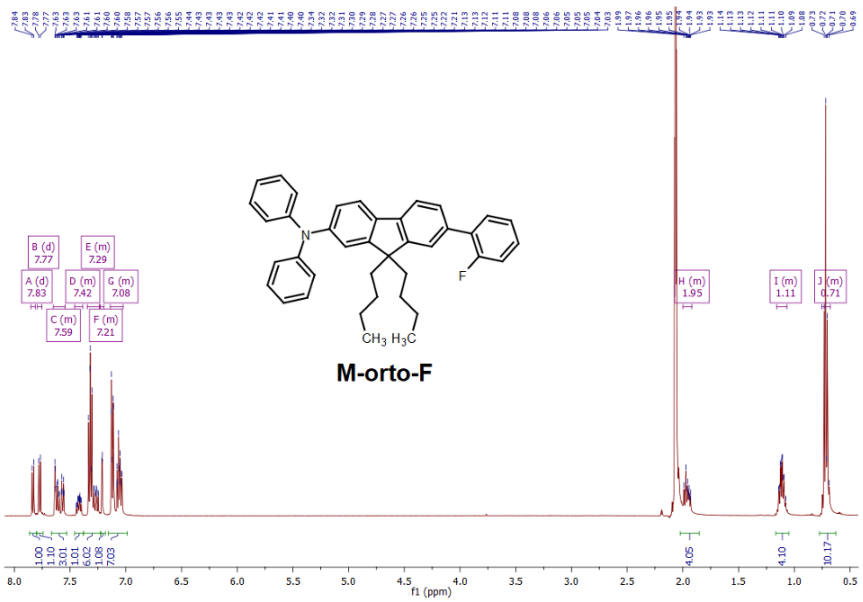

Figure S5: [1]H NMR spectrum of M-ortho-F

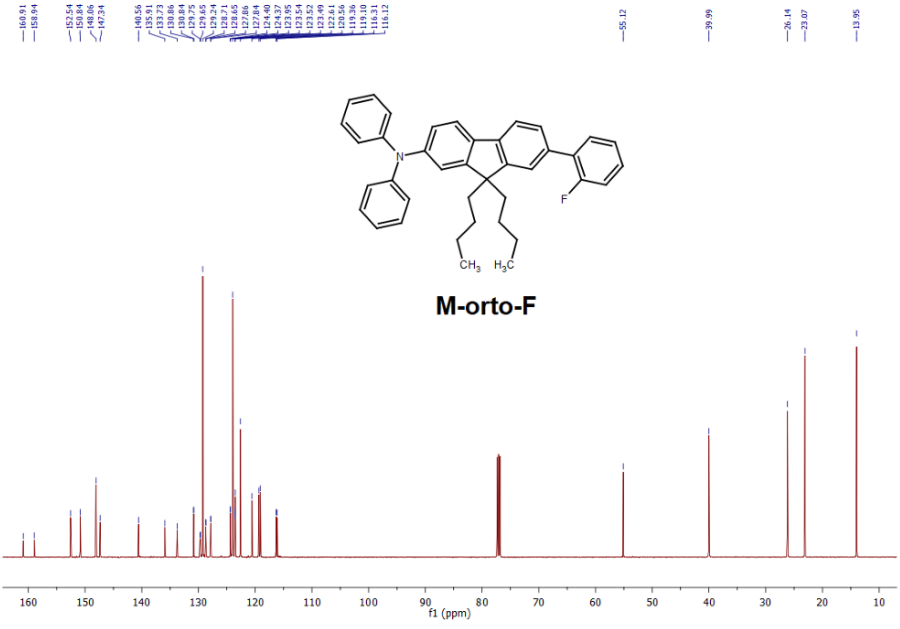

Figure S6: [13]C NMR spectrum of M-ortho-F

2. Supporting graphics and tables

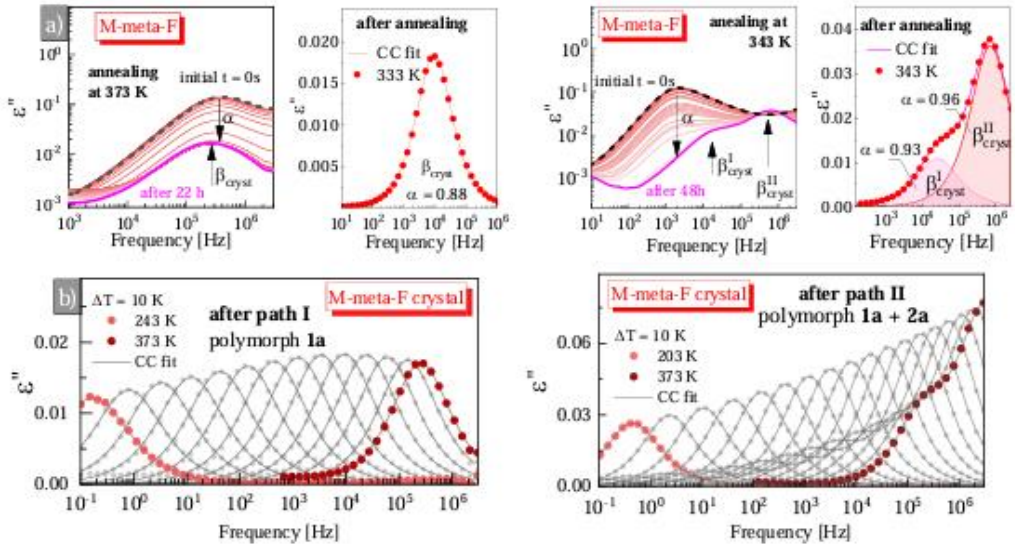

Figure S7: a) The progression of crystallization for not presented in main text M-meta-F polymorphs. Right column show selected spectrum with Cole-Cole function and shape parameters. b) Dielectric spectra showing the obtained β_{cryst} processes at different temperatures.

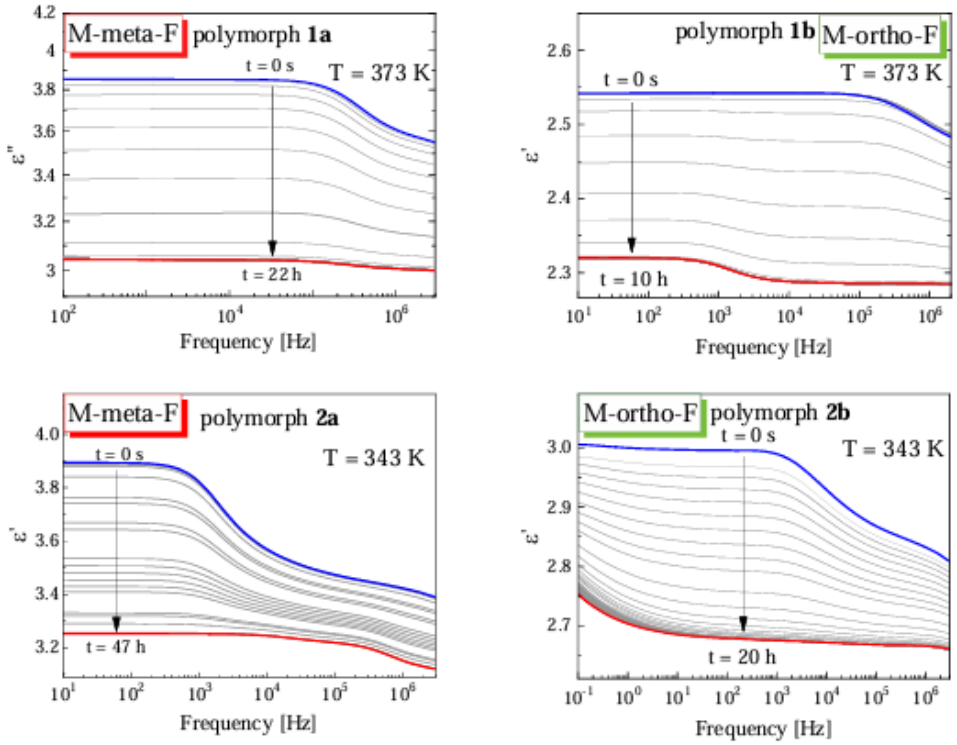

Figure S8: ε' data for crystallization progress of all polymorphs.

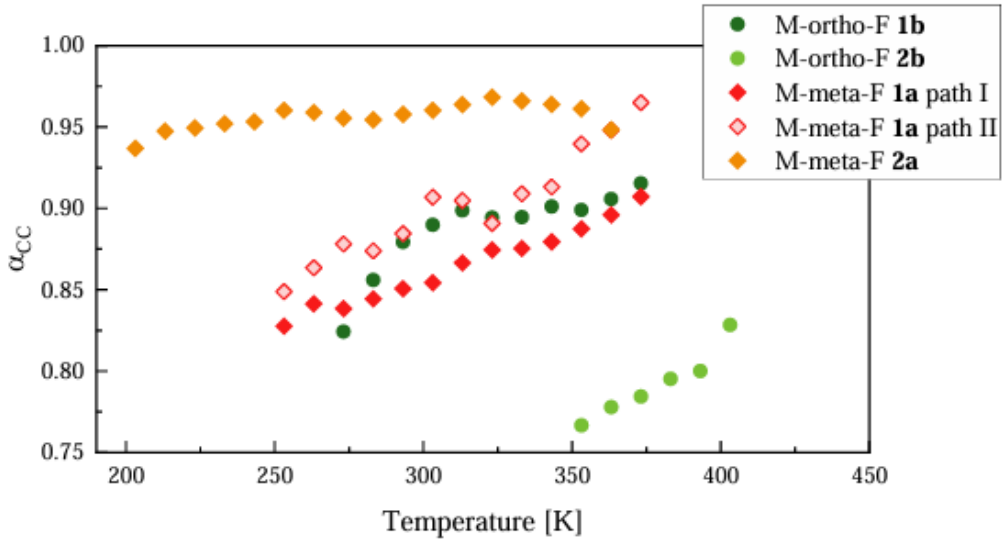

Figure S9: Changes in the shape parameter α of the CC function as a function of temperature.

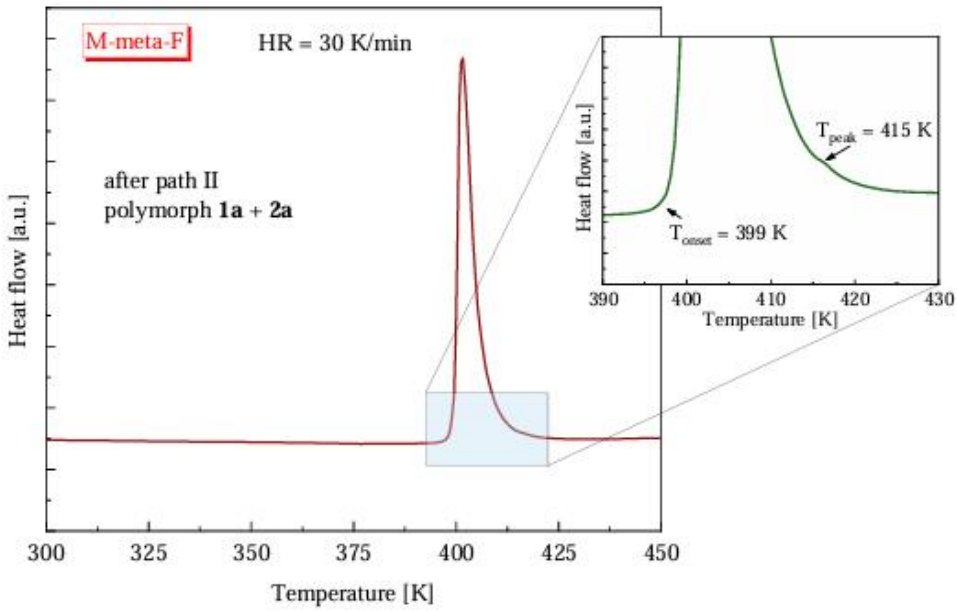

Figure S10: Thermogram obtained on heating of recrystallized M-meta-F after path II with 30 K/min heating rate.

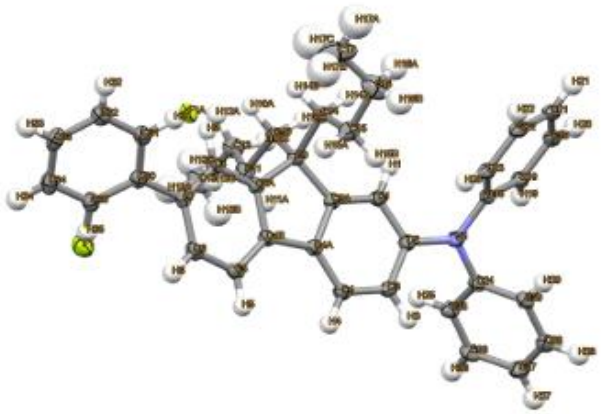

Figure S11: M-ortho-F polymorph **1b** structure in thermal ellipsoid representation.

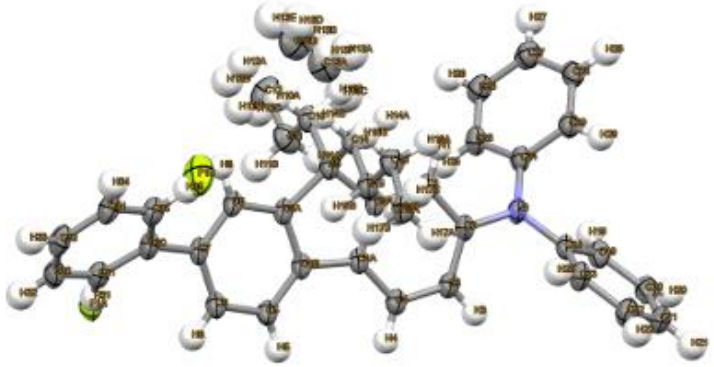

Figure S12: M-ortho-F polymorph **2b** structure in thermal ellipsoid representation.

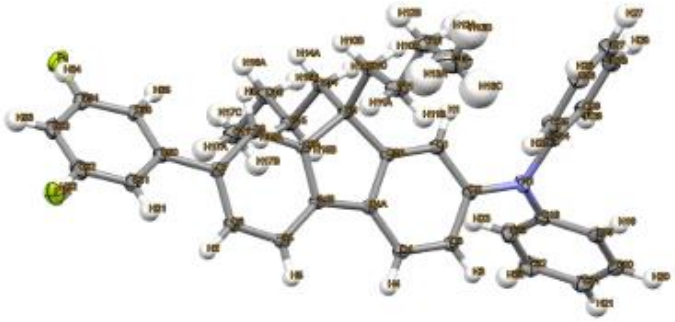

Figure S13: M-meta-F polymorph **1a** structure in thermal ellipsoid representation.

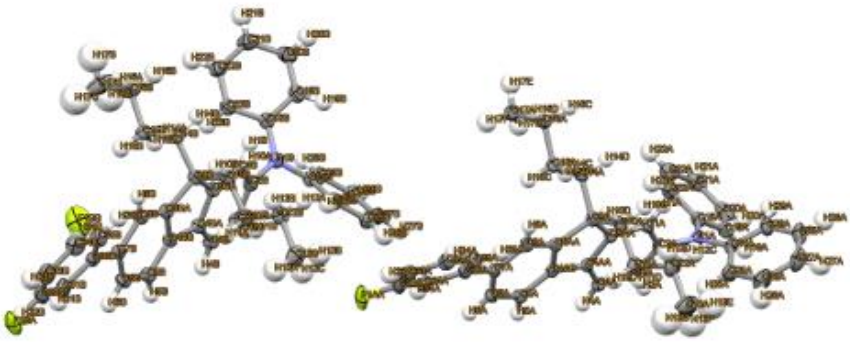

Figure S14: M-meta-F polymorph **2a** structure in thermal ellipsoid representation.

Table S1: Fit parameters of Arrhenius function for glasses and crystals.

		E_a [kJ/mol]	logτ [s]
M-meta-F	Glass	45.20 ± 0.72	-14.98 ± 0.18
	Polymorph **1a** path I	83.32 ± 0.65	-17.85 ± 0.11
	Polymorph **1a** path II	85.00 ± 0.42	-18.06 ± 0.07
	Polymorph **2a**	58.26 ± 0.08	-15.48 ± 0.01
M-ortho-F	Glass	47.10 ± 0.58	-15.61 ± 0.15
	Polymorph **1b**	86.47 ± 0.08	-16.16 ± 0.52
	Polymorph **2b**	128.49 ± 2.66	-18.32 ± 0.37

Table S2: Structural parameters of obtained single crystals of M-meta-F and M-ortho-F.

	M-meta-F		**M- -F**	
	polymorph 1a	**polymorph 2a**	**polymorph 1b**	**polymorph 2b**
CCDC	2353733	2353734	2353736	2353735
T/K	100			
Chemical formula	$C_{39}H_{38}FN$			
Formula Mass	539.70			
Wavelength/Å	0.71073		1.54184	
Crystal system	Triclinic		Orthorhombic	Triclinic
Space group	P -1		P 2_1 2_1 2_1	P -1
Z	2	4	4	2
Unit cell dimensions				
a/Å	9.2598(2)	10.1561(3)	10.7172(2)	9.1595(9)
b/Å	12.6652(4)	17.1667(4)	13.3801(3)	12.6777(12)
c/Å	14.3895(4)	18.3720(4)	20.9751(5)	14.2485(9)
α/°	72.700(3)	107.171(2)	90	104.837(7)
β/°	89.726(2)	97.397(2)	90	93.252(7)
γ/°	71.324(2)	97.617(2)	90	109.944(9)
Unit cell volume/Å^3	1518.72(8)	2985.28(13)	3007.77(12)	1484.4(2)
F(000)	576	1152	1152	576
D_x /Mg m^{-3}	1.180	1.201	1.192	1.207
μ /mm^{-1}	0.072	0.073	0.559	0.566
Theta range for data collection/º	2.958 to 36.357	2.951 to 36.534	3.919 to 73.720	3.250 to 73.673
Range of *h*, *k*, *l*	$-15 \le h \le 13$ $-20 \le k \le 20$ $-23 \le l \le 21$	$-16 \le h \le 16$ $-27 \le k \le 23$ $-21 \le l \le 30$	$-13 \le h \le 13$ $-16 \le k \le 14$ $-21 \le l \le 26$	$-11 \le h \le 10$ $-10 \le k \le 15$ $-17 \le l \le 17$
No. of measured reflections	23308	45564	19730	8491
No. of independent reflections	13469	26507	5905	5229
R_{int}	0.0292	0.0405	0.0330	0.0427
Data / restraints / parameters	13469 / 0 / 382	26507 / 0 / 754	5905 / 0 / 382	5229 / 0 / 393
Goodness-of-fit on F^2	1.035	1.022	1.047	1.054
Final R_1 values ($I > 2\sigma(I)$)	0.0551	0.0584	0.0343	0.0910
Final $wR(F^2)$ values ($I > 2\sigma(I)$)	0.1396	0.1370	0.0823	0.2562
Final R_1 values (all data)	0.0829	0.1016	0.0383	0.1031
Final $wR(F^2)$ values (all data)	0.1648	0.1729	0.0850	0.2822
Largest diff. peak and hole/eÅ^3	0.569 and -0.273	0.494 and -0.309	0.214 and -0.188	0.414 and -0.454

3.3 Artykuł A3

A3. A. Błażytko, M. Rams-Baron & M. Paluch. The influence of molecular shape on reorientation dynamics of sizable glass-forming isomers at ambient and elevated pressure. Scientific Reports, 14, 887 (2024).

Impact Factor z roku opublikowania: 4.1

Punkty ministerialne: 140

DOI: 10.1038/s41598-023-50894-8

Mój wkład do tego artykułu polegał na przygotowaniu manuskryptu, zaplanowaniu badań, przeprowadzeniu eksperymentów za pomocą spektroskopii dielektrycznej oraz skaningowej kalorymetrii różnicowej oraz analizie wyników. Oświadczenia o wkładzie pozostałych współautorów zostały zamieszczone w podrozdziale 3.4.

scientific reports

OPEN

The influence of molecular shape on reorientation dynamics of sizable glass-forming isomers at ambient and elevated pressure

Alfred Błażytko, Marzena Rams-Baron✉ & Marian Paluch

We used dielectric spectroscopy to access the molecular dynamics of three isomers with a structure based on a sizable, partially rigid, and non-polar core connected to a polar phenylene unit differing in the position of the polar group, and, consequently, the direction and magnitude of the dipole moment to address the question how unique molecular properties, in particular large size and elongated shape, affect the dynamics. The position of the polar group differentiates the molecular shape and isomer's anisotropy and leads to different thermal and dynamic properties of the isomers. The shape of permittivity loss spectra was governed by magnitudes of the longitudinal and transverse components of dipole moment to a large extent. For para isomer with negligible traverse component of dipole moment, the narrowest loss peak was found while for meta isomer, the bimodal loss peak was observed at high temperatures. Its shape evolved on cooling limiting the possibility of individual mode separation near glass transition where the dynamics were more cooperative. High-pressure dielectric studies showed that sizable isomers were characterized by the pronounced sensitivity of glass transition temperature, T_g, to compression. Observed high activation volumes, such as 735 cm^3/mol at T_g for para isomer, were found to correlate with the length scale of dynamic cooperativity. The number of dynamically correlated molecules depended on molecular shape and varied among isomers while the determined values were much smaller than that reported for other glass-forming liquids. We discussed here the obtained results in the context of the specific properties of the systems studied showing the overriding role of anisotropy.

The study of molecular mobility is important in many areas of science and engineering, including materials science, physics, and chemical engineering. It can provide insight into the physical and chemical properties of materials and can help to design and optimize materials for specific applications. Broadband dielectric spectroscopy (BDS) is one of the most common techniques for molecular dynamics examination with a longstanding tradition of studying supercooled liquids and glasses. What constantly attracts researchers' attention to glass-forming materials is the spectacular evolution of dynamic properties covering 15 orders of magnitude in a relatively small temperature range between the melting and glass transition temperatures, providing unique opportunities to study the fascinating and still not fully understood effects related to the cooperative phenomenon of liquid-to-glass transition.

To study the reorientation dynamics using the BDS method, the molecule must exhibit a non-zero value of the dipole moment[1]. The case of anisotropic glass-forming molecules is of particular interest because the longitudinal and transverse components of the dipole moment can contribute to the dielectric response to a different extent. In contrast, for small and symmetrical particles with isotropic shapes, such differences are expected to be negligible. Most anisotropic glass-forming molecules investigated to date host rod-shaped, disc-shaped, or bent-core structures that can form liquid crystalline phases. The importance of molecular shape in determining their mesogenic and dielectric properties has been well recognized[2]. In the vast majority of these materials the dipole moment was directed along the long molecular axis, making the longitudinal component of a dipole moment a main probe of molecular motion. On the other hand, very few studies have concentrated on the role of anisotropy in the dielectric response of disordered systems. Consequently, our understanding of how the

August Chełkowski Institute of Physics, University of Silesia in Katowice, 75 Pułku Piechoty 1, 41-500 Chorzow, Poland. ✉email: marzena.rams-baron@us.edu.pl

longitudinal and transverse components of dipole moment sample different aspects of reorientations in such anisotropic glass-formers is still incomplete.

Recently, unusual dielectric behavior at a high temperature was reported for anisotropic glass formers with a sizable core[3]. When most supercooled liquids at high temperatures revealed a narrow and symmetric Debye-like dielectric loss peak which broadened on cooling, a representative of sizable molecules showed the bifurcation of the main loss peak at high temperatures. This behavior has been interpreted as a manifestation of individual aspects of the motion of a sizable and anisotropic molecule, which can reorient along short and long axes on different time scales. Of course, this result raises the question of how exactly the dielectric response i.e. bimodal peak shape is connected to molecular properties of sizable glass-formers.

It is generally agreed that as the glass transition is approaching, the character of molecular motions becomes more cooperative[4]. The independent reorientations observed at high temperatures, evolve on cooling towards cooperative behavior where the motion of molecules depends strongly on their neighborhood. Therefore, as the temperature increases towards the melting temperature the shape of dielectric spectra, sensitive to dynamic heterogeneity, can uncover some individual features of molecular motion whose discrimination near T_g is unattainable. On the other hand, molecular dynamics, structure, and properties (also cooperativity) of glass-forming materials can be also effectively tuned by varying the pressure at a constant temperature. By performing dielectric studies at elevated pressure, it is possible to determine the activation volume characterizing the sensitivity of reorientation dynamics to compression[5]. Its value depends on the size of the reorienting unit, but in the case of isomers with identical molecular weights, any differences may shed more light on the importance of anisotropy and molecular shape. In the case of molecules with elongated shapes, the application of pressure can provide additional information to understand better the eventual separation of time scales of relaxations associated with long and short axes reorientation and differences in pressure sensitivity of particular modes. Additionally, the relation between activation volume and cooperativity length scale for structural relaxation was reported[6] which validity is interesting to check in the context of unusual properties found for sizable glass-formers in the previous studies[3,7].

A first indication of the bimodal dielectric response of sizable glass formers was given in ref.[3]. In our considerations, the term sizable glass formers refers to molecules with a molecular weight above 600 g/mol that have multiple rigid ring-containing structures and exhibit unique dielectric properties e.g. large value of pre-exponential factor of a Vogel–Fulcher–Tammann (VFT) law used to describe the temperature dependence of an α relaxation process originated from reorientation around shorter molecular axis[3]. Here, we investigated other representatives of sizable glass-formers with a structure based on the same concept of an anisotropic, partially rigid, and sizable non-polar core containing various heterocyclic structures and aliphatic chains connected to a polar phenylene unit, see Fig. 1. As a linker between polar and non-polar segments, we used an acetyl bridge, unlike in the previous paper[3]. The linker modification allows us to increase the system anisotropy in comparison to sizable glass-formers investigated before. We used a trifluoromethyl group, $-CF_3$, to introduce the dipole moment to the investigated molecules. It was variously attached to the phenyl ring at the ortho, meta, or para positions. This approach provided us with isomers with a well-defined direction of the dipole moment vector and different molecular shapes – more elongated in comparison to those studied in ref.[3], suitable for further systematic dielectric studies of their reorientation dynamics.

The main goal of the current work was to address the question of how differences in molecular shapes among isomers will impact the spectral properties revealed in dielectric investigations at ambient and elevated pressure in thermodynamic conditions corresponding to a supercooled liquid state. To facilitate understanding of the complex reorientation dynamics above the T_g, we analyzed and discussed data collected below T_g, where the relaxation pattern also depends on the position of the $-CF_3$ group attached to the rotating phenyl ring. Our calorimetric and dielectric studies revealed many differences in thermal and relaxation properties between isomers which were largely due to differences in the molecular shapes. At the same time, certain characteristic features, common to all isomers were identified. Namely, high-pressure studies showed that all isomers revealed pronounced sensitivity of reorientation dynamics to compression as indicated by very high values of activation volumes and pressure coefficients of T_g. A particularly important result of this work was the observation of complex dielectric response for a meta isomer at high temperatures and at elevated pressure which we attributed to reorientation along the long and short molecular axes whose time scales decouple as the degree of intermolecular cooperativity decreases. In addition, we examined the degree of heterogeneity near the glass transition and confirmed the validity of a relation between the correlation radius and the activation volume reported for other glass-forming materials[8]. We discussed the obtained results in the context of the specific properties of isomers studied—their large size, substantial stiffness of sizable cores, and elongated shape. We have shown the overriding role of anisotropy which we identified as a pivotal feature determining the dynamic properties of the studied isomers.

Results and discussion

Thermal characterization

Figure 2 shows thermograms measured on heating of crystalline (top panel) and vitrified (bottom panel) isomers of sizable molecules. On thermograms recorded for crystalline samples only one endothermic process was observed (top panel), which corresponds to the melting of the crystalline material. The highest melting temperature, T_m, was found for meta-CF_3, i.e. $T_m = 438$ K. The para and ortho isomers melt at $T_m = 435$ K and $T_m = 403$ K, respectively. The T_m value observed for ortho-CF_3 was found to be significantly lower in comparison to other isomers, which may indicate the presence of weaker bonds in the crystal structure of the ortho isomer[5].

A step change in heat capacity, indicating the glass transition phenomenon, was observed on each thermogram recorded on heating of vitrified samples. The exact temperature values at the midpoint of the glass transition

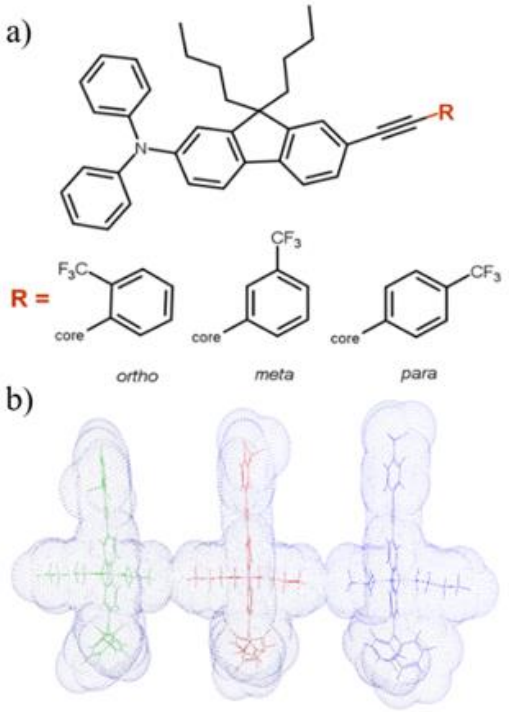

Figure 1. (**a**) The chemical structure of the studied isomers. (**b**) Geometrically optimized structures through the AM1 semi-empirical method. Starting from the left: ortho-CF_3, meta-CF_3, and para-CF_3 are presented. Symbolic mesh shows the van der Waals volume of the molecules. The drawing was created using Vega ZZ software.

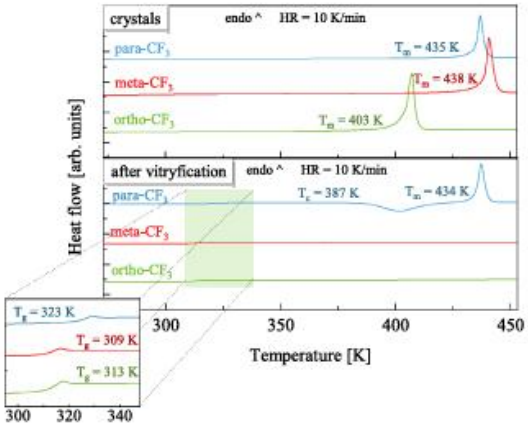

Figure 2. Thermograms showing thermal processes observed during heating of crystalline (upper panel) and vitrified (lower panel) samples. The inset magnifies the glass transition region.

were determined using temperature-modulated differential scanning calorimetry (TMDSC). The highest value of the glass transition temperature, T_g, was found for para-CF_3 i.e., $T_g^{TMDSC} = 323$ K. The ortho and meta isomers show the glass transition at $T_g^{TMDSC} = 313$ K and $T_g^{TMDSC} = 309$ K, respectively. Several factors can affect the glass transition temperature, such as differences in molecular structure (molecular weight, polarity, shape) and the ability to form intermolecular bonds[9–12]. The studied isomers have the same mass and atomic composition. However, due to the differences in the position of the CF_3 group, the shape of a molecule and the strength of intermolecular interactions can vary among isomers.

The thermogram registered for para-CF_3, besides the glass transition feature, shows an additional process at $T_c = 387$ K attributed to non-isothermal crystallization. The lowest physical stability of vitrified para-CF_3 among investigated isomers is related to its higher symmetry facilitating the formation and growth of crystals. As shown on several low-molecular-weight liquid pairs (like p-xylene and m-xylene, or benzene and toluene), those showing greater symmetry had a greater tendency to recrystallize[13,14].

Reorientation dynamics at ambient pressure

To characterize the reorientation dynamics and compare the properties of particular isomers at ambient pressure we performed first the dielectric measurements at temperatures corresponding to the supercooled liquid state. Figure 3 shows the frequency dependence of the imaginary part of complex permittivity, ε"(f), at various temperatures. The prominent process well-resolved on all recorded ε"(f) spectra is a structural relaxation peak (denoted also as α-relaxation) corresponding to the cooperative reorientation of the molecules and directly related to the glass transition. For anisotropic elongated systems, such neighbor-dependent molecular rearrangement can occur via long or short axes reorientations. On cooling the structural relaxation peak maximum shifts toward lower frequencies manifesting a growing time-scale required for molecular reorientation as the temperature decreases towards the glass transition. In contrast to meta-CF_3 and ortho-CF_3, the amplitude of α-relaxation for para-CF_3 started decreasing at T = 367 K. Such behavior denotes the onset of crystallization and is consistent with the behavior revealed in DSC studies indicating recrystallization of the para-CF_3 sample when heated above T_g. When liquid–crystal transformation progresses on heating, para-CF_3 molecules that constitute the crystal

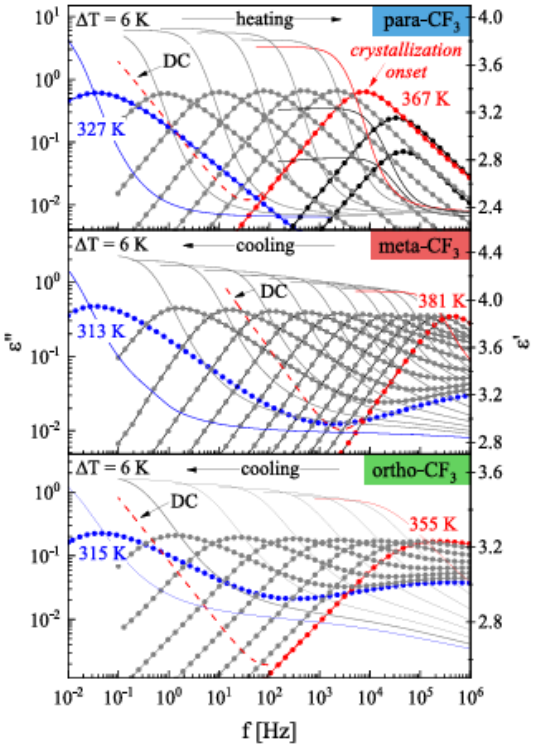

Figure 3. The dielectric response of para-CF_3, meta-CF_3, and ortho-CF_3 at ambient pressure. The solid lines represent the real part of dielectric permittivity ε' (right axis), while the dotted lines indicate the imaginary part of the permittivity ε" (left axis). In the case of para-CF_3 black color was used to distinguish partially recrystallized spectra. The dc-conductivity has been removed from the spectra, except one illustrating the magnitude of dc contribution (dashed red line).

lattice lose the ability to reorient. As a consequence, the decreasing number of mobile dipoles is accompanied by a drop in the α-peak amplitude[15].

To get more detailed information about the relaxation properties of the isomers studied, the data presented in Fig. 3 were fitted using the Havrilik–Negami (HN) function with the dc-conductivity term:

$$\varepsilon^* = \frac{\sigma}{\varepsilon_0 \omega} + \varepsilon_\infty + \frac{\Delta\varepsilon}{(1 + (i\omega\tau_{HN})^\alpha)^\beta}$$

where $\sigma/\varepsilon_0\omega$ defines the dc-conductivity contribution, ε_∞ is the high-frequency permittivity limit, $\Delta\varepsilon$ is dielectric strength, ω is the angular frequency, τ_{HN} corresponds to the Havriliak-Negami relaxation time, and the exponents α and β are the shape parameters[16]. The outcome of the fitting procedure for representative spectra selected for each isomer is shown in the right panels of Fig. 4.

For meta and ortho isomers, apart from the main structural relaxation peak, the additional contribution from the secondary relaxation denoted as the β-process was distinguishable in the high-frequency part of the spectrum. Although the maximum of β-process was far outside the experimental window its presence was included in the right panel of Fig. 4 to make the comparison among isomers clearer. The main experimental peak was satisfactorily fitted with a single HN function for para-CF_3 and ortho-CF_3 isomers, while for the meta-CF_3, such an approach was insufficient. In the case of meta isomer, a strong shape asymmetry evolved on heating, indicating bifurcation of the primary process at high temperatures, required two HN functions. These two processes began to merge on cooling, and a single HN function could reasonably parametrize the ε"(f) data for meta-CF_3 at temperatures below T = 340 K. A similar pattern of behavior was observed previously and attributed to various aspects of the motion of molecules with identical anisotropic sizable cores[3]. Due to their elongated shape, two molecular axes can be distinguished, relative to which the molecular reorientation can occur. Depending on whether the motion concerns the short or long axis, inertia impacts the reorientation to varying degrees. The link between the moment of inertia about the principal axes of the molecule, I, and the relaxation time about the same axes is hidden in the square-root relationship of the pre-exponential factor[17] $\tau_0 \sim (2\pi I/k_B T)^{0.5}$ in a function describing the nonlinear temperature behavior of relaxation times. Thus in the case of elongated molecules, reorientation with respect to the short axis is expected to be slower than reorientation about the longer axis being observed at higher frequencies[3]. The detection of mentioned aspects of reorientation depends on the presence of appropriate components of the dipole moment vector. A schematic illustration of each isomer with an indication of the components of the dipole moment vector is shown in the inset of Fig. 4. The presented values of the dipole moment, μ, were calculated using the AM1 semi-empirical method. For para-CF_3 the calculated value was the highest, i.e. μ = 5.67 D, for the meta-CF_3 μ = 4.48, and for the ortho-CF_3 μ = 2.68 D. Variations in the magnitude of μ were reflected in the magnitude of dielectric strength $\Delta\varepsilon \sim N\mu^2$, where N is the number of mobile dipoles,

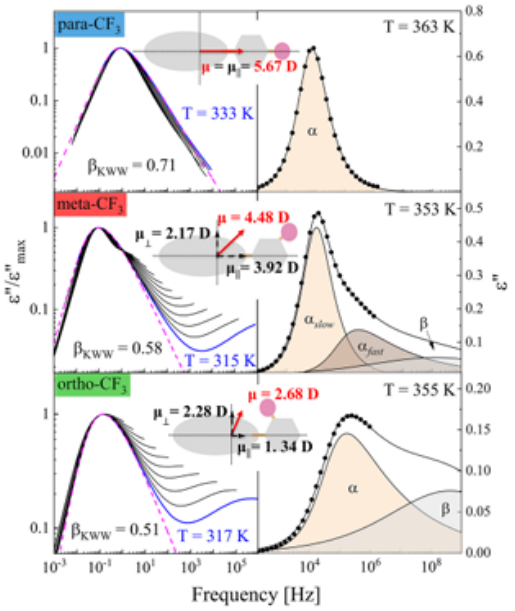

Figure 4. Left panel: Masterplots (superimposition of spectra on selected ones) with the applied KWW function (dashed line). The insets of each plot show a schematic representation of the molecule and dipole moment vectors with dipole moment values in parallel and perpendicular axes. Right panel: Example spectrum with HN fit function for para-CF_3 and meta-CF_3, and with HN and CD fit functions for ortho-CF_3.

as shown in Fig. 3, which was the lowest for ortho isomer. The dipole moment vector in the case of the para-CF_3 was directed parallel to the long axis (the perpendicular component was negligibly small), so the movement of a molecule relative to the short axis dominated the dielectric response. In the case of meta-CF_3 and ortho-CF_3, the dipole moment components parallel and perpendicular to the long molecular axis probe all reorientation aspects. So, both modes contribute to the dielectric response. If, due to the different impact of inertia effects, their time scales were different, we should be able to distinguish them in the dielectric response. The effect should be more pronounced at high temperatures where the mobility is less cooperative. This is particularly evident in the dielectric spectrum of the meta-CF_3, where two relaxation processes were observed at high temperatures. We assigned them as α_{fast} (long axes reorientation probed by perpendicular component of μ) and α_{slow} (short axes reorientation probed by a parallel component of μ). In the case of the ortho isomer, such a clear indication was not found. This can be related to the much smaller magnitude of the parallel component of the dipole moment vector in ortho-CF_3 (see illustration in inset to Fig. 4). Then the long-axis reorientations dominate the dielectric response and may cover the slower contribution to the α process. Nevertheless, both contributions will affect the width of the main relaxation peak in ortho-CF_3 leading to its broadening.

To quantify the differences in the spectral shapes in terms of the frequency distribution of relaxation times between isomers, we created so-called masterplots by horizontally superimposing spectra recorded at different temperatures. The obtained masterplots depicted in Fig. 4 (left panel) showed significant differences in the shape of the loss peak between isomers. To quantitatively describe these differences, we applied a one-sided Fourier transform of the Kohlraush-Williams-Watt (KWW) function[18,19]:

$$\Phi(t) = exp\left[-\left(\frac{t}{\tau_\alpha}\right)^{\beta_{KWW}}\right]$$

where β_{KWW} is a stretching parameter that takes values from 0 to 1, where a value of 1 indicates a narrow and symmetric α-relaxation peak (as in the Debye process); and the more β_{KWW} value approaches 0, the broader and more asymmetric the process is. The β_{KWW} value is commonly used to quantify dynamic heterogeneity, reflected in the frequency dispersion of relaxation times. The case of meta and ortho isomers investigated herein is unconventional because the shape of the dielectric loss peak results from two different reorientation modes, which, however, are indistinguishable near T_g. Thus, the significance of the β_{KWW} parameter is not entirely the same as in the case of isotropic systems in which the dipole moment reflects the reorientation of the entire molecule. A possible approach for molecules investigated herein could be treating β_{KWW} value as a measure of the distribution of relaxation times resulting from individual contributions of distinct modes. Each isomer has a different α-relaxation shape regarding the frequency distribution of relaxation times reflected in distinct β_{KWW} values established for dielectric spectra collected close to T_g. For para-CF_3 $\beta_{KWW} = 0.71$ at $T = 333$ K, for meta-CF_3 $\beta_{KWW} = 0.58$ at $T = 315$ K, and for ortho-CF_3 $\beta_{KWW} = 0.51$ at $T = 317$ K. The highest β_{KWW} value in the case of the para isomer indicates the smallest distribution of relaxation times. The smallest degree of dynamic heterogeneity can be explained by the fact that in para-CF_3 the dipole moment samples one type of motion, i.e., short axes reorientation. In contrast, for the ortho and meta isomers, the apparent broadening is due to two relaxation modes contributing to the main loss peak.

The next step was to find out the temperature dependence of relaxation times attributed to molecular reorientation. In particular, it was interesting to see differences in the time scale of reorientation along particular axes for the meta-CF_3. Relaxation times τ_α, τ_{slow} and τ_{fast} were determined from HN fit using the following formula[1]:

$$\tau = \tau_{HN}\left[sin\left(\frac{\pi\alpha}{2+2\beta}\right)\right]^{-1/a}\left[sin\left(\frac{\pi\alpha\beta}{2+2\beta}\right)\right]^{1/a}$$

Figure 5 shows how the characteristic relaxation times evolve in a non-linear manner with temperature in the supercooled liquid phase. Such behavior can be parametrized by the Vogel–Fulcher–Tammann (VFT) function:

$$\tau_\alpha = \tau_0 exp\left(\frac{DT_0}{T - T_0}\right)$$

where $\tau_0 \sim (2\pi I/k_B T)^{0.5}$ is the pre-exponential factor depending on I according to Bauer expression[17], D determines the deviation from Arrhenius behavior, and T_0 is the so-called ideal glass temperature[20–22]. The value of fitting parameters τ_0, D, and T_0 are shown in Table 1. From the extrapolation of the VFT function to $\log\tau_\alpha = 2$, the glass transition temperature, T_g^{BDS}, was determined as a temperature corresponding to a relaxation time of 100 s.

For the para-CF_3 isomer, the glass transition temperature was $T_g^{BDS} = 322 \pm 2$ K, for meta-CF_3 $T_g^{BDS} = 308 \pm 1$ K, and ortho-CF_3 $T_g^{BDS} = 310 \pm 1$ K. The T_g values obtained from BDS and TMDSC were in very good agreement. In the case of the meta-CF_3, the growing cooperativity of molecular dynamics on cooling is manifested in the course of VFT curves for α_{slow} and α_{fast} processes that merge when the T_g is reached. The closer to T_g, the more difficult is to distinguish the different aspects of meta-CF_3 motion. A similar effect related to the vanishing bimodal character of the loss spectra due to the cooperativity onset was observed recently by Blochowicz et al. for lower molecular-weight liquids[23]. To describe the temperature dependence of relaxation times for the ortho-CF_3 with physically reliable parameters, we used two VFT functions. The limits of their applicability were determined from the Stickel analysis[24]. For meta-CF_3 and para-CF_3 the values of pre-exponential factor obtained from the free VFT fit of $\tau_\alpha(1000/T)$ data meet the criterion $\tau_\alpha > 10^{-12}$ s, previously reported for other representatives of sizable glass-formers and identified as a characteristic feature of their dynamics[3].

To compare the temperature behavior of the relaxation times for all isomers, an Angell plot was created where the logarithm of relaxation times, τ_α, τ_{slow} and τ_{fast}, were depicted versus normalized temperature T_g/T, see

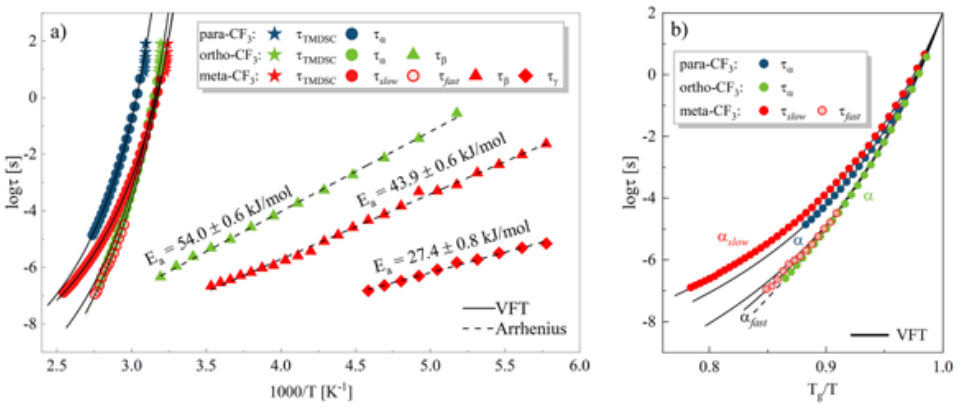

Figure 5. (**a**) Temperature dependence of relaxation times τ_α or τ_{slow} (closed circles) and τ_{fast} (open circles for meta-CF_3) of three structural isomers: para-CF_3 (blue), meta-CF_3 (red), and ortho-CF_3 (green). The asterisk denotes relaxation times determined from TMDSC. The solid line corresponds to the VFT fit function with fitting parameters denoted in Table 1. (**b**) Angel plot.

	T_m (K)	T_c (K)	T_g^{TMDSC} (K)	T_g^{BDS} (K)	β_{KWW}	m	VFT parameters		
							$\log\tau_0$ (s)	D	T_0 (K)
para-CF_3	435	387	323	322 ± 2	0.70	99 ± 12	− 12.31 ± 0.12	5.58 ± 0.14	275.56 ± 0.73
meta-CF_3	438	–	309	308 ± 1	0.58	92 ± 5	− 11.77 ± 0.03	5.59 ± 0.05	262.02 ± 0.27
						102 ± 23[a]	− 16.05 ± 0.29[a]	9.12 ± 0.45[a]	252.78 ± 1.79[a]
ortho-CF_3	403	–	313	310 ± 1	0.51	100 ± 8	− 16.53 ± 0.11	9.71 ± 0.17	252.85 ± 0.57

Table 1. Calorimetric and dielectric parameters characterizing dynamics of investigated isomers at ambient pressure conditions. [a]Value for the α_{fast} process.

panel b Fig. 5. The comparison of their course indicated interesting relationships. It seems that the character of temperature changes reflects the mechanism of reorientations dominating the dielectric response. For the α_{fast}-process in meta-CF_3 and α-process in ortho-CF_3, very similar behavior was observed. It supports our previous claim that long-axis reorientations determine the reorientation dynamics of ortho-CF_3 to a large extent. Based on the VFT function, the fragility coefficient m was determined. The m value refers to the rate at which structural relaxation times deviate from a linear relationship as T_g is reached[25]. Fragile glass-formers are characterized by a rapid rate of change, while strong substances are characterized by the opposite. To determine the fragility we used the following formula[26,27]:

$$m = \left.\frac{d\log\tau_\alpha}{d\left(T_g/T\right)}\right|_{T=T_g}$$

The calculated m values were relatively similar for all isomers studied. For para isomer $m = 99$. A similar value was found for the α_{slow}-process in meta-CF_3, i.e. $m = 92$. For the α-process in ortho isomer and α_{fast} in meta-CF_3 slightly higher values were found, i.e. for, $m = 100$ and $m = 102$, respectively. Referring to a frequently used classification of glass-forming materials as strong ($m \geq 30$), intermediate ($30 < m < 100$), and fragile ($100 \leq m$)[25], the sizable molecules studied herein can be considered as moderately fragile glass-forming molecules. It is worth noting that higher fragility values were observed for modes identified with reorientation around the long axis.

Glassy dynamics at ambient pressure

Below T_g, the dielectric response of isomers was dominated by secondary relaxations. This term covers a diversified class of relaxation processes involving molecular fragments or side-group motion as well as intermolecular processes with connections to structural relaxation and glass transition called Johari-Goldstein (JG) relaxations[28–30].

Playing with the substitution of the polar $-CF_3$ group attached to the phenyl ring (Ph-ring) allowed us to indicate with high certainty the molecular origin of the prominent secondary relaxation assigned as β-process. By adding a polar group to the Ph-ring, we have intentionally labeled it and made its internal rotation the dominant contribution to the dielectric response below T_g. Accordingly, we could relate the strong β-relaxation to the internal rotation of the Ph-ring substituted with the polar $-CF_3$ group. The only exception was the para

isomer, in which the dipole moment was directed along the long molecular axis (see Fig. 4a) and did not change during the internal rotation of the Ph–CF_3 unit. Consequently, the corresponding β-process was not visible in the dielectric response of para-CF_3 (see inset in Fig. 6a).

The dielectric loss spectra collected for an ortho isomer (Fig. 6c) below T_g revealed a single secondary β-relaxation related to the internal rotation of the Ph–CF_3 unit with activation energy of $E_a = 54.0 \pm 0.6$ kJ/mol determined from Arrhenius law. For the meta-CF_3 the rotation of the Ph–CF_3 unit was faster and associated with a lower activation barrier, i.e. $E_a = 43.9 \pm 0.6$ kJ/mol. In comparison to ortho-CF_3, the internal rotation in the meta-CF_3 was less coupled to the motion of the rest of the molecule. The proximity of a sizable core hindered the Ph–CF_3 dynamics in the orto isomer. Interestingly, in the vicinity of T_g, the time scale of internal rotation in ortho-CF_3 agrees with the predictions of the Coupling Model (CM). The use of CM is a common way to approximate the Johari-Goldstain (JG) secondary relaxation time identified with intermolecular dynamics and connections to the glass transition[31]. In Fig. 6b, c a vertical arrow indicates the primitive relaxation frequency $f_0 = 1/2\pi\tau_0$ corresponding to the primitive relaxation time τ_0, a precursor of structural relaxation according to CM. We calculated τ_0 as $\tau_0 = (\tau_c)^{1-\beta_{KWW}}(\tau_\alpha)^{\beta_{KWW}}$ using $\tau_c = 2$ ps, and τ_α and β_{KWW} determined for spectra collected above T_g and depicted in Fig. 6a, c[31]. For the ortho isomer, the position of the β-process at T = 317 K corresponded well with CM predictions showing that the Ph-CF_3 motion is coupled with the dynamics of the rest of the molecule. In the meta isomer, the rotating unit was more distant from the sizable core, thus less coupled with core dynamics, and the compliance with the CM predictions was not so good. The agreement between the time scale of primitive relaxation of CM and the β-process provided important information about the sensitivity of Ph-CF_3 rotational dynamics to the molecular environment. The relevance of intermolecular contributions may result from the presence of fluorine in the rotating fragment, which can interact with hydrogen atoms in its vicinity during rotation. Thus, close to T_g the rotation of the Ph-CF_3 unit will be not independent, but due to intermolecular contacts, will be sensitive to the molecular environment and a liquid-to-glass transition.

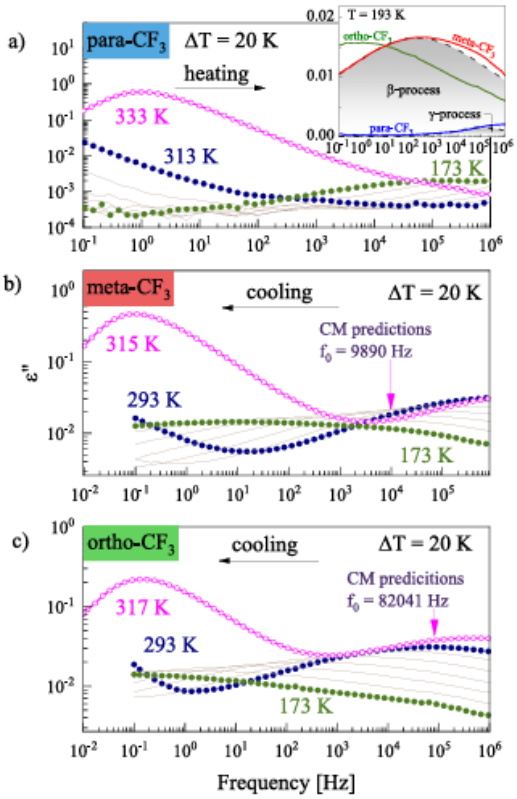

Figure 6. The representative dielectric loss spectra that we recorded for para-CF_3 (**a**), meta-CF_3 (**b**), and ortho-CF_3 (**c**) in the vicinity and below T_g. For meta and ortho isomers the parameters τ_α and β_{KWW} determined from the presented ε''(f) data above T_g were used to calculate f_0 (marked with arrow). Inset in panel (**a**) shows a comparison of the loss spectra for glasses at T = 193 K, along with the marked contributions from β and/or γ relaxations (dashed lines) determined from Cole–Cole fits to ε''(f) data for meta-CF_3.

In the case of meta-CF_3, in addition to the β-process, we identified a faster secondary relaxation visible in the loss spectra recorded at low temperatures with $E_a = 27.4 \pm 0.8$ kJ/mol, denoted as γ-process (see Fig. 5a). Interestingly, γ-relaxation was also apparent in the loss spectra collected for para-CF_3 (see inset to Fig. 6a), but its presence was not evidenced in the dielectric response of ortho-CF_3. The rapid secondary γ-relaxation can be related to alkyl chains, whose dynamics in the case of the ortho isomer might be inhibited by the proximity of the bulky $-CF_3$ group. In the para isomer, the γ-process was the fastest, which prevented its detailed analysis in the considered temperature range.

Also noteworthy is the nature of the temperature dependence of relaxation times which vary depending on the molecular origin of a given relaxation mode. In the case of reorientation along different molecular axes, the corresponding relaxation times (α_{slow} and α_{fast} in meta-CF_3) separate at high temperatures where the motions are more independent, and merge on cooling. For the β-process opposite behavior was found since it separates systematically from structural relaxation on cooling as the temperature decreases towards T_g.

Reorientation dynamics at elevated pressure

In the next stage of our study, we investigated how the isomer's reorientation dynamics can be affected by elevated pressure. Isothermal dielectric measurements were carried out for several temperatures, i.e. 353 K, 358 K, 363 K for para-CF_3, 341 K, 351 K, 361 K for meta-CF_3, and 343 K, 351 K, 365 K for ortho-CF_3. The left panel of Fig. 7 shows representative dielectric loss spectra for one isotherm for each isomer.

With increasing pressure, the α-relaxation process shifts toward lower frequencies, as it is observed during isobaric cooling when dynamics slows down when glass transition is approaching. To analyze the data, we used the HN model as before. The pressure dependence of relaxation times for all isotherms is presented in the right panel of Fig. 7. The nonlinear pressure behavior of characteristic relaxation times could be described by the pressure variant of the VFT function (so-called pVFT)[32]:

$$\tau = \tau_0 exp\frac{D_p P}{P_0 - P}$$

where τ_0 is the relaxation time at ambient pressure, P_0 is the pressure of the ideal glass, and D_p is a parameter depending on the pressure fragility of the material. The fitting parameters of the pVFT function are depicted in Table 2.

By extrapolating the pVFT function to $\log\tau = 2$, the pressure value corresponding to the glass transition at a given temperature was determined (see Table 2). The sensitivity of glass transition temperature to compression is a characteristic feature of a given material. To characterize it, the pressure coefficient of T_g was introduced[5]. For isomers studied herein the applied pressure significantly influenced the glass transition temperature. The T_g(P) relationship for all isomers, visualized in Fig. 8 had a linear character. In such a case the dT_g/dP parameter i.e. pressure coefficient of T_g can be estimated from the slope of a linear function[33]. The ortho and meta isomers were characterized by almost identical values of dT_g/dP, i.e. $dT_g/dP = 0.326$ and $dT_g/dP = 0.332$ K/MPa, respectively, while the para isomer stands out among others with a higher value $dT_g/dP = 0.387$ K/MPa. It is worth noting that this is one of the highest values observed to date among non-polymeric glass-forming substances[5,34]. It means that sizable glass formers exhibit an especially pronounced sensitivity of T_g to compression.

Another important parameter that can be discerned from dielectric data collected as a function of pressure characterizing the pressure sensitivity of relaxation times is activation volume, $\Delta V^{\#}$. In general terms, the activation volume $\Delta V^{\#}$ is related to the local volume required for the molecular rearrangement of a relaxing unit. Within the framework of transition state theory, $\Delta V^{\#}$ is defined as the difference between the volumes occupied by a molecule in activated and inactive states[5]. It is therefore natural to assume that the value of $\Delta V^{\#}$ should reflect the size of the reorienting objects. Such regularity was illustrated in the past for a series of polyalcohols with increasing van der Waals radius (glycerol, threitol, xylitol, and sorbitol)[35]. For meta-CF_3 the bifurcation of the structural relaxation process, observed in ambient pressure studies at high T, was successfully observed for isotherm collected at $T = 361$ K. This allows us to examine the effect of pressure on both relaxations, α_{slow} and α_{fast}. We determined $\Delta V^{\#}$ value for α_{slow} and α_{fast} using the following formula:

$$\Delta V^{\#} = RT\left(\frac{dln\tau}{dP}\right)_T$$

where R is the gas constant and T is the temperature[5]. The pressure dependence of $\Delta V^{\#}$ for both modes in meta-CF_3 is presented in Fig. 9.

It may be surprising to see that a larger activation volume was found for the α_{fast}-process identified previously with the long-axis reorientations. When considering a single rod-like molecule, such rearrangements, intuitively, are regarded as less massive and less volumetric in comparison to short-axis reorientations. Therefore, we expected that in thermodynamic conditions, where particular relaxation modes can be detected, the motions relative to the short-axis would be characterized by a larger activation volume. The opposite behavior that we observed in the experiment can be understood if the molecules form an anisotropic cluster in which the short and long axes can be also distinguished. The larger activation volume for molecular rearrangements along the long axis can be explained when the molecules in the cluster are arranged parallel to each other and create an ellipsoid shape in which the long axis of the molecule becomes the short axis of the cluster. Then, the behavior illustrated in Fig. 9 can be rationalized. Our observation suggests that in the case of anisotropic objects, the activation volume may be a source of information about the morphology of relaxing clusters of dynamically correlated molecules. As the glass transition approaches during compression, a cooperatively relaxing cluster becomes larger and larger and its shape will change. So theoretically the change in activation volume could be

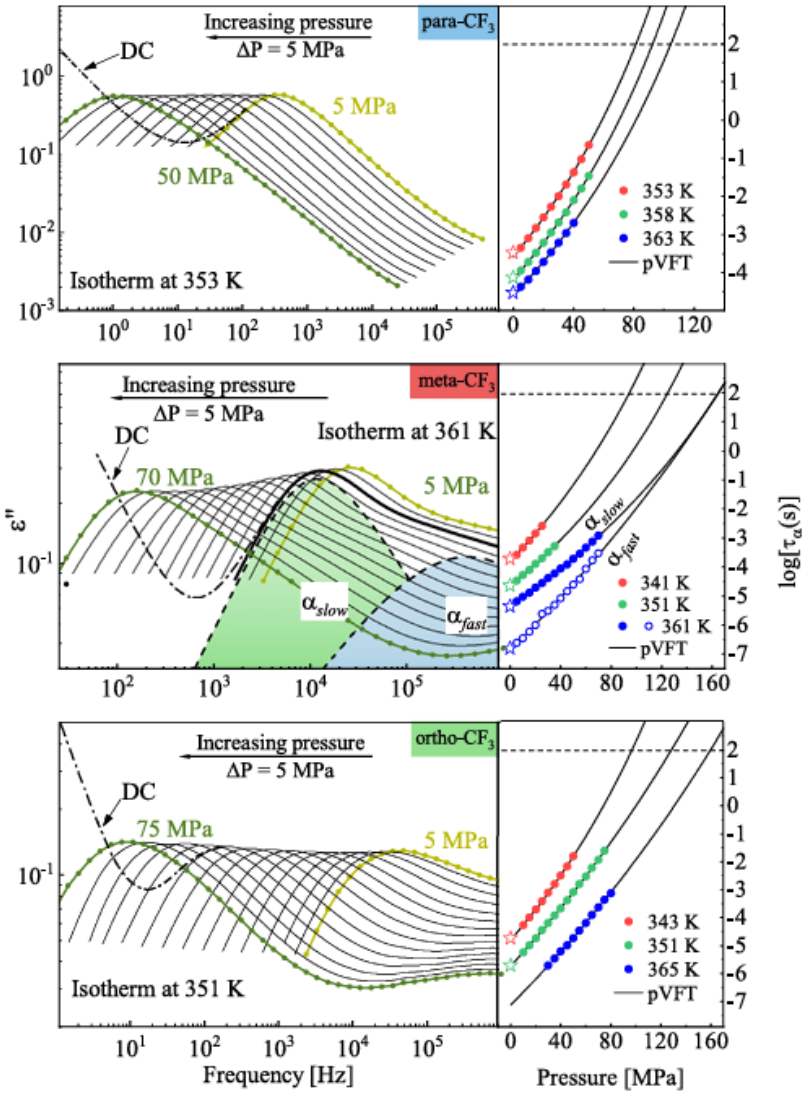

Figure 7. Left panel: representative dielectric loss spectra ε''(f) for selected isotherm measured during compression for indicated pressure ranges with the step of Δp = 5 MPa. The dc- conductivity was subtracted except for one spectrum which illustrates its impact. For meta-CF3 the contribution from α_{slow} and α_{fast} was indicated. Right panel: pressure dependence of relaxation times τ_α, τ_{slow} and τ_{fast} (only for meta-CF_3). Stars indicate τ_α from ambient pressure measurements. The solid line represents pVFT fit functions. The corresponding fitting parameters are shown in Table 2. The glass transition pressure P_g was determined for logτ = 2 as marked by a horizontal dashed line.

an indicator of the cluster morphology at least under certain thermodynamic conditions when the cooperativity onset is not too high. As the pressure increases, the number of cooperatively rearranging molecules will grow limiting our ability to separate different aspects of molecular motion and corresponding $\Delta V^{\#}$ values.

To compare the activation volume near the glass transition for all isomers we used the formula proposed by Paluch et al.[5,36]:

$$\Delta V^{\#} = 2.303R\left(\frac{dT_g}{dP}\right)m$$

	dT_g/dP (K/MPa)	$\Delta V^{\neq}$ (cm^3/mol)	T (K)	$log\tau_0$ (s)	D_P	P_0 (MPa)	P_g (MPa)
para-CF_3	0.387 ± 0.070	735	353	− 3.58 ± 0.01	12.29 ± 1.02	260.96 ± 14.94	81.5
			358	− 4.17 ± 0.01	12.03 ± 0.81	272.89 ± 14.94	92.5
			363	− 4.56 ± 0.02	12.51 ± 3.45	302.95 ± 71.85	104.6
meta-CF_3	0.332 ± 0.010	648	342	− 3.8 ± 0.01	16.17 ± 6.79	357.46 ± 138.6	94.3
			351	− 4.64 ± 0.01	12.87 ± 3.29	366.7 ± 84.23	124.8
			361	− 5.32 ± 0.01	12.31 ± 1.53	431.19 ± 44.87	160.8
				− 6.82 ± 0.03[a]	80.16 ± 8.63[a]	813.64 ± 69.89[a]	
ortho-CF_3	0.326 ± 0.011	624	341	− 4.79 ± 0.01	18.87 ± 1.53	366.16 ± 25.22	97.0
			353	− 5.73 ± 0.01	33.21 ± 2.54	680.47 ± 45.98	128.5
			361	− 7.13 ± 0.06	34.15 ± 11.61	757.74 ± 223.67	159.8

Table 2. Parameters determined from dielectric measurements at elevated pressure characterizing the reorientation dynamics of isomers—the pressure coefficient of glass transition (dT_g/dP), activation volume at T_g ($\Delta V^{\neq}$), fitting parameters of pVFT function ($log\tau_0$, D_P, P_0), the pressure value P_g corresponding to the glass transition at various T. [a]Determined for α_{fast} process.

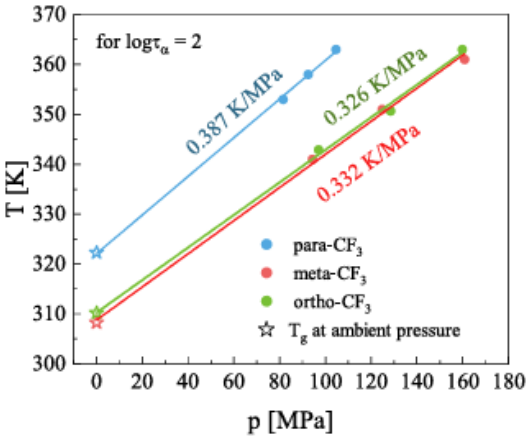

Figure 8. Pressure dependence of the glass transition temperature. Stars denote the T_g values obtained from isobaric BDS measurements at ambient pressure, while closed circles represent data from isothermal measurements at elevated pressure. The solid line indicates the linear fit function whose slope was used to determine the dT_g/dP value. The values of dT_g/dP for each isomer are depicted.

where R is the gas constant, dT_g/dP is the pressure coefficient of glass transition, and *m* is the fragility parameter determined from isobaric measurements (depicted in Table 1). Knowing that the activation volume calculated for reorientation relative to different molecular axes may yield different values, the choice of a formula allowing to determine $\Delta V^{\neq}$ directly in T_g seemed to be the most appropriate. Based on the assumption that individual modes merge in T_g, such an approach allowed us a reliable comparison of the properties of individual isomers. The calculated activation volumes $\Delta V^{\neq}$ at T_g for ortho-CF_3 and meta-CF_3 were similar, i.e. $\Delta V^{\neq} = 624$ cm^3/mol and $\Delta V^{\neq} = 648$ cm^3/mol, respectively. For para-CF_3 the highest value equal to $\Delta V^{\neq} = 735$ cm^3/mol was found. The much higher $\Delta V^{\neq}$ for para-CF_3 in comparison to other isomers can be due to the most elongated shape of para isomer as illustrated in Fig. 1. Interestingly, the elongation of the molecule caused by the substitution of the CF_3 group in the para position impacts the value of the $\Delta V^{\neq}$ near T_g to such a great extent. Taking into account the highly cooperative nature of molecular motion in the vicinity of T_g, the eventual lack of differences could be easily rationalized. Meanwhile, the observed distinct behavior of the para-CF_3 proves that the $\Delta V^{\neq}$ near T_g is still highly sensitive to molecular shape and degree of molecule elongation.

The above discussion regarding differences in dynamical behavior near T_g in the context of the activation volume and previous discussion about the limited possibility of distinguishing α_{slow} and α_{fast} modes in meta-CF_3 near T_g prompted us to further studies aimed at better understanding the cooperative nature of dynamics of sizable molecules. The concept of cooperatively rearranging regions (CRRs), was introduced by Adam and Gibbs to describe the relaxation behavior of molecules that can rearrange their configurations independently of the environment[4]. Such structural subunits increase on cooling (or during compression), so as the dynamics evolve towards the glass transition the number of molecules relaxing cooperatively increases. For the systems studied,

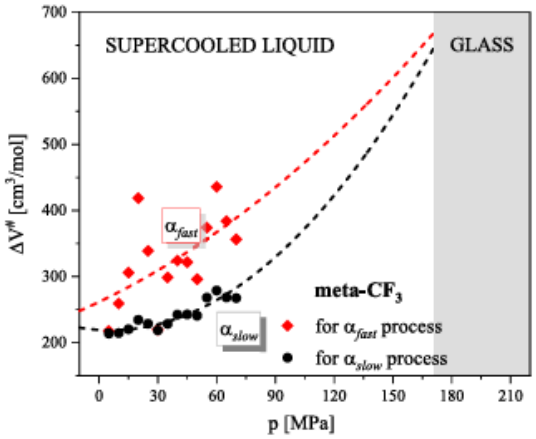

Figure 9. Pressure dependence of activation volume $\Delta V^{\#}$ for meta-CF_3 for isotherm collected at T = 361 K in the supercooled liquid state. Dashed lines represent the prediction of activation volumes in higher pressure.

the increasing degree of motion cooperativity observed on cooling is of great importance because the bimodal character of structural relaxation peak could be distinguished only at high temperatures and low pressures when the motion of molecules was more independent.

To calculate a number of dynamically correlated molecules near the glass transition we performed TMDSC measurements and used the approach proposed by Donth[37]. This method is based on the fluctuation–dissipation theorem, which, by studying enthalpy fluctuations, allows us to determine quantitatively the size of the cooperatively rearranging regions. The number of dynamically correlated molecules N_α^D at T_g was calculated using the following equation:

$$N_\alpha^D(T_g) = \frac{N_A\left(\frac{1}{C_p^{glass}} - \frac{1}{C_p^{liquid}}\right)}{M(\delta T)^2} k_B T_g^2$$

where N_A is Avogadro's number, C_p^{glass} and C_p^{liquid} are the heat capacity of glass and liquid at T_g, k_B is Boltzmann's constant, M is the molar mass, and δT is the average temperature fluctuation associated with the glass transition dynamics[38]. The results of TMDSC measurements are shown in Fig. 10. The ΔT range was determined by 16% and 84% of the value of the total difference in heat capacity between glass and liquid. To calculate δT, the value of ΔT was divided by 2.5 as our measurements were performed during heating. The calculated N_α^D values at T_g are summarized in Table 3. The highest number of dynamically correlated molecules was found for para-CF_3, i.e. $N_\alpha^D = 55$. For meta-CF_3 and ortho-CF_3 $N_\alpha^D = 44$ and $N_\alpha^D = 35$, respectively. The values obtained for studied isomers are much lower than those reported in the past for different classes of glass-forming liquids. The summary of

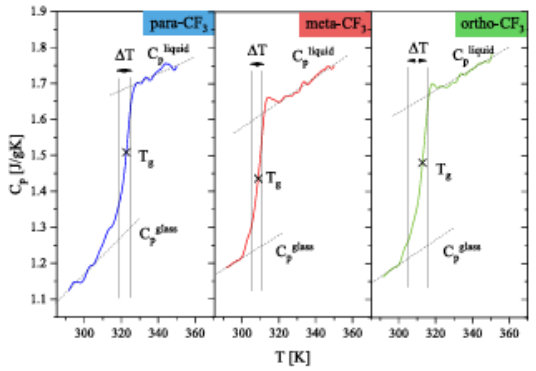

Figure 10. Temperature dependences of quasi-static specific heat capacity C_p for the investigated isomers used to calculate the $N_\alpha^D(T_g)$ using the Donth method.

	C_p^{glass} (J/g-K)	C_p^{liquid} (J/g-K)	T_g (K)	δT (K)	N_α^D	V_α (nm^3)	ξ (nm)
para-CF_3	1.34	1.68	323	1.97	55	48.89	3.81
meta-CF_3	1.24	1.60	309	2.30	44	39.21	3.54
ortho-CF_3	1.26	1.65	313	2.68	35	30,68	3.26

Table 3. Parameters used to calculate the number of dynamically correlated molecules N_α^D at T_g, according to the Donth approach and the values of N_α^D, the volume of correlated molecules V_α, and radius of correlation ξ determined at T_g for investigated isomers.

available data can be found in ref.[39] showing that reported values cover the range of 70 – 200 for van der Waals liquids and H-bonded liquids and 200 – 820 for polymers. The small values found for sizable isomers can be explained by their large size. Next to size, the molecular stiffness of sizable cores formed by multiple ring-based groups is probably important. It is interesting to note that the variations in N_α^D values apparently depend on the molecular shapes of investigated isomers with the highest N_α^D value for the most elongated isomer.

Knowing the number of dynamically correlated molecules, we could determine the occupied volume as $V_\alpha = N_\alpha^D M/\rho$ where ρ is a density assumed to be 1.15 g/cm^3 for all isomers (i.e. value determined from helium pycnometer for meta-CF_3), and subsequently calculate the radius of correlation using the following relationship $\xi = V_\alpha^{1/3}$[40]. The value of ξ corresponds to the (typical) size of a CRR postulated by Adam and Gibbs, and mentioned before[4]. Hong et al. showed that there is a correlation between the radius of cooperatively reorientating domains and the activation volume[40]. This correlation was satisfied for a wide and diverse range of materials from low-molecular-weight glass formers to larger but flexible polymers. Thus, it was interesting to check if this correlation is also valid for sizable isomers studied herein. Figure 11 shows the correlation between ξ and $\Delta V^\#$ reported by Hong et al.[40] with added data for sizable isomers. One can see that our results (marked with stars) matched the trend established by the authors very well. After taking into account data points for sizable molecules, the slope of a linear function that approximates the correlation is equal to 0.303 ± 0.02. The highest activation volume $\Delta V^\#$ near T_g was found for para isomer characterized by the highest radius of correlation and the highest volume occupied by dynamically correlated molecules. The characteristic length scale related to dynamic cooperativity reported for various glass-forming liquids was estimated to be 1 – 4 nm[37]. Referring to this, the values obtained for the tested isomers are relatively high. For ortho-CF_3 the radius of correlation was equal to ξ = 3.26 nm. The higher value was found for meta-CF_3 i.e. ξ = 3.54 nm while for para-CF_3 the determined ξ value was the highest, i.e. ξ = 3.81 nm. The increasing correlation length scale determined at T_g for particular isomers corresponds well with the increasing degree of molecule elongation resulting from the different positions of the –CF_3 group, which again proves the overriding role of anisotropy in determining the dynamic properties of isomers studied. Our results i.e. confirmation of correlation compliance for sizable glass-formers pointed out that the ξ parameter has a more universal meaning than the number of correlated molecules. The value of N_α^D, determined by the specific and inherent properties of the system, can be treated more as a characteristic feature of a given class of glass-forming molecules.

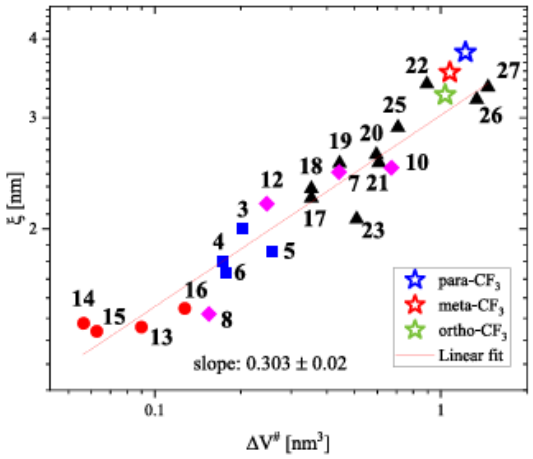

Figure 11. Correlation between the cooperativity length scale ξ and the activation volume $\Delta V^\#$ at T_g reported by Hong et al.[40] with added data for sizable isomers investigated herein (marked with stars). The compounds hidden under the depicted numbers are described in ref.[40].

Conclusions

In the present work, a series of structural isomers were studied by differential scanning calorimetry and dielectric spectroscopy at ambient and elevated pressure. Investigated isomers possess the same large-sized rigid core and a trifluoromethyl group variously substituted in the ortho, meta, or para positions to the phenylene ring. Variations in the position of the polar $-CF_3$ group differentiated the dipole moment of the molecule and the molecular shape. Our results showed that the specific molecular features of isomers studied—their large size, stiffness of some heterocyclic building blocks, elongated shape, the dipole moment properties, affect the picture of molecular dynamics to a great extent. From both calorimetric and dielectric studies, it was shown that isomers differ in their glass transition temperature, melting point, and tendency to recrystallize from the supercooled liquid state. The observation of bifurcation of the structural relaxation process, or the significant frequency distribution of relaxation times, is closely related to the detection of different types of relaxation motions, attributed to long and short axes reorientations of anisotropic molecules studied herein. We confirmed that depending on the thermodynamic conditions and cooperativity degree, the individual modes could be distinguished in the dielectric response of some sizeable glass formers. The meta-CF_3 isomer is another example of a sizable glass-forming molecule for which it was possible to distinguish the time scale of individual modes associated with long or short axes reorientations at (T, p) conditions where the dynamics were more independent. This is an important observation showing that spectra recorded at high temperatures may contain additional information about motion components that are unattainable around T_g due to the highly cooperative nature of molecular dynamics. As in our previous study on another group of sizable glass-formers, unusually large pre-exponential factors τ_0 were observed[3,7] which strengthens the general importance of our previous report. Molecular dynamics studies under elevated pressure revealed that the entire series was characterized by very high values of dT_g/dP and $\Delta V^{\ddagger}$. The highest values of the mentioned parameters were found for the most elongated para-CF_3 isomer. An interesting result was the observation that the long-axis reorientations were characterized by a larger activation volume than those relative to the short axis, which was contrary to common-sense expectations. An explanation for this situation may be to consider a cluster of cooperatively reorienting molecules, rather than the result expected from a single molecule. Our discussion shows that the activation volume can contain information about the morphology of relaxing units and how clusters of cooperatively reorientating molecules grow. We identified another feature specific to the class of sizable glass formers, which was small magnitudes of the number of dynamically correlated molecules in T_g. The determined values of this parameter are the lowest ever reported for van der Waals glass-forming molecules. Interestingly, among so many peculiar properties characterizing the dynamics of sizable isomers, it was found that they satisfied a correlation valid for many other glass-forming systems between the radius of correlation at T_g and the activation volume.

Our results clearly show that not only the chemical composition or mass of the molecules but also molecular shape, anisotropy, and the place of substitution of the polar group can affect the reorientation dynamics. This discovery may contribute to a better understanding of the link between the structure of molecules and their dynamics, which is desirable, especially in the context of designing new molecules for selected applications. Further investigations improving our molecular-level understanding of remarkable sizable systems dynamics, e.g. employing Raman or infrared spectroscopy measurements, can bring us closer to the ultimate goal that has remained unchanged for years which is improving the understanding of glass-formers dynamics in general.

Methods

Materials

We investigated herein three isomers of sizable molecules whose chemical structures are shown in Fig. 1. All materials were synthesized by TriMen Chemicals (Łódź, Poland) with a declared purity of ≥ 97%. Isomers studied herein will be reffered to as ortho-CF_3 (*N*-(7-[(2-trifluoromethylphenyl)ethynyl]-9,9-dibutyl-9H-fluoren-2-yl)-*N*,*N*-diphenyamine), meta-CF_3 (*N*-(7-[(3-trifluoromethylphenyl)ethynyl]-9,9-dibutyl-9H-fluoren-2-yl)-*N*,*N*-diphenyamine), para-CF_3 (*N*-(7-[(4-trifluoromethylphenyl)ethynyl]-9,9-dibutyl-9H-fluoren-2-yl)-*N*,*N*-diphenyamine. The molecular mass of each compound was M = 613.75 g/mol. Note that the supplier of the para-CF_3 sample was different than in ref.[7] and found properties differed slightly from a batch of the material tested elsewhere.

Differential scanning calorimetry (DSC)

We used a Mettler-Toledo DSC1 STARe differential scanning calorimeter to study the thermal properties and phase transformations in the investigated isomers. This calorimeter was equipped with a nitrogen cooling system and an HSS8 ceramic sensor equipped with 120 thermocouples. Temperature and enthalpy calibration was carried out using indium and zinc standards. The samples (with a mass of around 5 mg) were placed in 40 µl aluminum vessels. The measurement protocol for each sample was the same. In the first temperature ramp, the crystalline sample was heated from T = 273 K to T = 453 K with a heating rate of 10 K/min. After the first scan, the sample was cooled at 10 K/min to vitrify the liquid and measured again on heating. The melting and crystallization temperatures were determined from the onset of the process, while the glass transition temperature was assessed from the midpoint of the heat capacity change.

Stochastic temperature-modulated differential scanning calorimetry (TMDSC) implemented by Mettler-Toledo (TOPEM) was used to determine the calorimetric relaxation times near the glass transition and heat capacity of the studied compounds. The samples were heated at a rate of 0.5 K/min. In the experiment, the temperature amplitude of the pulses of 0.5 K was selected. We analyzed the dynamic behavior in the range from 5 to 20 mHz. The values of the quasi-static heat capacity were calibrated using a sapphire reference curve.

Broadband dielectric spectroscopy (BDS)

The study of the complex electric permittivity $\varepsilon^*(f) = \varepsilon'(f) - i\varepsilon''(f)$ at varying temperatures was carried out using an Alpha Impedance analyzer spectrometer by Novocontrol. The samples were analyzed in the frequency range of 10^{-1}—10^6 Hz. In the vicinity of the glass transition temperature, T_g, the frequency range was extended to 10^{-2} Hz. Before the measurement, the materials were dried under vacuum after melting (40 min at T = 363 K) and then quenched on a cooled copper plate to vitrify. The sample has been placed between parallel steel capacitor plates with a diameter of 15 mm. A gap of 0.1 mm was provided by quartz fibers. The capacitor with the investigated material was placed in the spectrometer and analyzed immediately after preparation. Dielectric measurements at ambient pressure were carried out with a step of $\Delta T = 2$ K at various temperature ranges, i.e. 327 K—395 K for para-CF_3, 313 K—387 K for meta-CF_3, and 315 K—355 K for ortho-CF_3. The ortho and meta isomers were measured on cooling while para, due to its high tendency to crystallization, could be measured on heating only. The Novocool system by Novocontrol was responsible for stabilizing the temperature to within 0.2 K.

Dielectric measurements under elevated pressure were carried out by combining an Alpha-A impedance analyzer (range 10^{-1} to 10^6) by Novocotrol with a hydrostatic pressure-generating system by Unipress, a tensometer by Nova Swiss, and a thermostat by Julabo. A set temperature (± 1 K) was reached by flowing liquid in a heating jacket around the pressure chamber. The investigated samples were prepared in the same manner as in the dielectric measurements at ambient pressure by melting, drying under vacuum, and then quenching on a cooled copper plate. Materials were placed between two parallel steel capacitor plates (with a diameter of 15 mm) separated with a 0.1 mm thick Teflon ring. Two wires connected the capacitor covers with the analyzer. After preparation, the sample was secured with Teflon tape and placed inside a chamber filled out with non-polar silicone oil as the compression medium.

Data availability

Data supporting the findings of this study are available within the article. Source data are available from the corresponding author on request.

Received: 7 November 2023; Accepted: 27 December 2023
Published online: 09 January 2024

References

1. Kremer, F. & Schonhals, A. *Broadband Dielectric Spectroscopy* (Springer, 2003).
2. Dunmur, D. A., De Fuente, M. R., Jubindo, M. A. P. & Diez, S. Dielectric studies of liquid crystals: The influence of molecular shape. *Liq. Cryst.* **37**, 723–736 (2010).
3. Rams-Baron, M., Yao, B., Cheng, S., Dulski, M. & Paluch, M. Complex reorientation dynamics of sizable glass-formers with polar rotors revealed by dielectric spectroscopy. *J. Phys. Chem. Lett.* **12**, 11303–11307 (2021).
4. Adam, G. & Gibbs, J. On the temperature dependence of cooperative relaxation properties in glass-forming liquids. *J. Chem. Phys.* **43**, 66 (1965).
5. Floudas, G., Paluch, M., Grzybowski, A. & Ngai, K. L. *Molecular Dynamics of Glass-Forming Systems. Effects of Pressure* (Springer, 2010).
6. Hong, L., Gujrati, P. D., Novikov, V. N. & Sokolov, A. P. Molecular cooperativity in the dynamics of glass-forming systems: A new insight. *J. Chem. Phys.* **131**, 66 (2009).
7. Jedrzejowska, A. *et al.* New paradigm of dielectric relaxation of sizable and rigid molecular glass formers. *Phys. Rev. E* **101**, 010603 (2020).
8. Hong, L., Novikov, V. N. & Sokolov, A. P. Dynamic heterogeneities, boson peak, and activation volume in glass-forming liquids. *Phys. Rev. E Stat. Nonlinear Soft Matter Phys.* **83**, 1–10 (2011).
9. Wang, L. M. & Richert, R. Glass transition dynamics and boiling temperatures of molecular liquids and their isomers. *J. Phys. Chem. B* **111**, 3201–3207 (2007).
10. Jenekhe, S. A. & Roberts, M. F. Effects of intermolecular forces on the glass transition of polymers. *Macromolecules* **26**, 35 (1993).
11. Juszyńska, E., Massalska-Arodź, M., Zieliński, P. M. & Ściesiński, J. DSC studies of neohexanol and its isomers. *Phase Transit.* **79**, 899–909 (2006).
12. Angell, C. A., Sare, J. M. & Sare, E. J. Glass transition temperatures for simple molecular liquids and their binary solutions. *J. Phys. Chem.* **82**, 2622–2629 (1978).
13. Turnbull, D. Under what conditions can a glass be formed?. *Contemp. Phys.* **10**, 473–488 (1969).
14. Turnbull, D. & Cohen, M. H. Free-volume model of the amorphous phase: Glass transition. *J. Chem. Phys.* **34**, 120–125 (1961).
15. Pacult, J., Rams-Baron, M., Chrząszcz, B., Jachowicz, R. & Paluch, M. Effect of polymer chain length on the physical stability of amorphous drug-polymer blends at ambient pressure. *Mol. Pharm.* **15**, 2807–2815 (2018).
16. Havriliak, S. & Negami, S. A complex plane representation of dielectric and mechanical relaxation processes in some polymers. *Polymer* **8**, 161–210 (1967).
17. Hill, N., Vaugham, W. E., Price, A. H. & Davies, M. *Dielectric Properties and Molecular Behaviour* (1969).
18. Kohlrausch, F. Nachtrag über die elastiche Nachwirkung beim Cocon und Glasladen. *Annalen der Physik und Chemie* (1863).
19. Williams, G. & Watts, D. C. Non-symmetrical dielectric relaxation behaviour arising from a simple empirical decay function. *Trans. Faraday Soc.* **66**, 80–85 (1970).
20. Vogel, H. Das Temperaturabhangigkeitgesetz Der Viskosität von Flüssigkeiten. *Physikalische Zeitschrift* **22**, 645–646 (1921).
21. Fulcher, G. S. Analysis of recent measurments of the viscosity of glasses. *J. Am. Ceram. Soc.* **8**, 339–355 (1925).
22. Tammann, G. & Hesse, W. Die Abhängigkeit Der Viscosität von Der Temperatur Bie Unterkühlten Flüssigkeiten. *Z Anorg Allg Chem* **156**, 245–257 (1926).
23. Zeißler, R., Pabst, F., Böhmer, T. & Blochowicz, T. Influence of intramolecular dynamics on the relaxation spectra of simple liquids. *Phys. Chem. Chem. Phys.* **25**, 16380–16388 (2023).
24. Stickel, F., Fischer, E. W. & Richert, R. Dynamics of glass-forming liquids. I. Temperature-derivative analysis of dielectric relaxation data. *J. Chem. Phys.* **102**, 6251–6257 (1995).
25. Angell, C. A. Relaxation in liquids, polymers and plastic crystals-strong/fragile patterns and problems. *J. Non Cryst Solids* **131**, 13–31 (1991).
26. Angell, C. A., Ngai, K. L., McKenna, G. B., McMillan, P. F. & Martin, S. W. Relaxation in glassforming liquids and amorphous solids. *J. Appl. Phys.* **88**, 3113–3157 (2000).

27. Hodge, I. M. Strong and fragile liquids-a brief critique. *J. Non Cryst. Solids* **202**, 164–172 (1996).
28. Kremer, F. & Loidl, A. *The Scaling of Relaxation Processes* (Springer, 2018).
29. Ngai, K. L. & Paluch, M. Classification of secondary relaxation in glass-formers based on dynamic properties. *J. Chem. Phys.* **120**, 857–873 (2004).
30. Johari, G. P. Glass transition and secondary relaxations in molecular liquids and crystals. *Ann N Y Acad. Sci.* **279**, 117–140 (1976).
31. Ngai, K. L. Relation between some secondary relaxations and the α relaxations in glass-forming materials according to the coupling model. *J. Chem. Phys.* **109**, 6982–6994 (1998).
32. Paluch, M., Rzoska, S. J., Habdas, P. & Ziolo, J. On the isothermal pressure behaviour of the relaxation times for supercooled glass-forming liquids. *J. Phys. Condens. Matter* **10**, 4131–4138 (1998).
33. Koperwas, K. *et al.* Pressure coefficient of the glass transition temperature in the thermodynamic scaling regime. *Phys. Rev. E Stat. Nonlinear Soft Matter Phys.* **86**, 66 (2012).
34. Roland, C. M., Hensel-Bielowka, S., Paluch, M. & Casalini, R. Supercooled dynamics of glass-forming liquids and polymers under hydrostatic pressure. *Rep. Prog. Phys.* **68**, 1405–1478 (2005).
35. Paluch, M., Grzybowska, K. & Grzybowski, A. Effect of high pressure on the relaxation dynamics of glass-forming liquids. *J. Phys. Condens. Matter* **19**, 205117 (2007).
36. Paluch, M., Gapinski, J., Patkowski, A. & Fischer, E. W. Does fragility depend on pressure? A dynamic light scattering study of a fragile glass-former. *J. Chem. Phys.* **114**, 8048–8055 (2001).
37. Hempel, E., Hempel, G., Hensel, A., Schick, C. & Donth, E. Characteristic length of dynamic glass transition near Tg for a wide assortment of glass-forming substances. *J. Phys. Chem. B* **104**, 2460–2466 (2000).
38. Grzybowska, K., Grzybowski, A., Wojnarowska, Z., Knapik, J. & Paluch, M. Ionic liquids and their bases: Striking differences in the dynamic heterogeneity near the glass transition. *Sci. Rep.* **5**, 66 (2015).
39. Capaccioli, S. *et al.* Dynamically correlated regions and configurational entropy in supercooled liquids. *J. Phys. Chem. B* **1**, 10652–10658 (2008).
40. Hong, L., Novikov, V. N. & Sokolov, A. P. Is there a connection between fragility of glass forming systems and dynamic heterogeneity/cooperativity?. *J. Non Cryst. Solids* **357**, 351–356 (2011).

Acknowledgements

This research was funded in a whole by the National Science Centre, Poland [Opus 21, 2021/41/B/ST5/00992]. For Open Access, the author has applied a CC-BY public copyright license to any Author Accepted Manuscript (AAM) version arising from this submission. The study was implemented as part of strategy of the University of Silesia—Inicjatywa Doskonałości (POB 1—Priorytetowy Obszar Badawczy 1: Harmonijny rozwój człowieka—troska o ochronę zdrowia i jakość życia).

Author contributions

A.B. planned and carried out the experimental work, analyzed the data, prepared figures, and co-wrote the manuscript; M.R.-B. co-wrote the manuscript, and supervised the project; M.P. co-wrote the manuscript.

Competing interests

The authors declare no competing interests.

Additional information

Correspondence and requests for materials should be addressed to M.R.-B.

3.4 Oświadczenia współautorów publikacji

Chorzów, 11.05.2026
Miejsce i data

mgr Alfred Blażytko
Imię i nazwisko współautora publikacji

Uniwersytet Śląski w Katowicach
Wydział Nauk Ścisłych i Technicznych
Instytut Fizyki im. A. Chełkowskiego
Afiliacja

OŚWIADCZENIE

Oświadczam, że w pracy:

A1. M. Rams-Baron, A. Błażytko, K. Jurkiewicz, P. Lodowski, M. Książek, J. Kusz, W. Mozga, M. Fordymacka, M. Teymouri, J. Krzywik & M. Paluch. Image of the solid-state rotary motion encoded in the dielectric response. Reports on Progress in Physics. 87, 108002 (2024), DOI: 10.1088/1361-6633/ad7288.

mój udział polegał na zaplanowaniu i przeprowadzeniu części eksperymentów za pomocą spektroskopii dielektrycznej oraz skaningowej kalorymetrii różnicowej.

A2. A. Błażytko, M. Rams-Baron, M. Książek, J. Kusz, M. Matussek, J. Grelska & M. Paluch. Engineering of Rotational Dynamics via Polymorph Manipulation. The Journal of Physical Chemistry A, 128, 50 (2024). DOI: 10.1021/acs.jpca.4c04964.

przygotowaniu manuskryptu, zaplanowaniu badań, przeprowadzeniu eksperymentów za pomocą spektroskopii dielektrycznej i skaningowej kalorymetrii różnicowej oraz analizie wyników.

A3. A. Błażytko, M. Rams-Baron & M. Paluch. The influence of molecular shape on reorientation dynamics of sizable glass-forming isomers at ambient and elevated pressure. Scientific Reports, 14, 887 (2024). DOI: 10.1038/s41598-023-50894-8.

mój udział polegał na przygotowaniu manuskryptu, zaplanowaniu badań, przeprowadzeniu eksperymentów za pomocą spektroskopii dielektrycznej oraz skaningowej kalorymetrii różnicowej oraz analizie wyników.

Błażytko
Podpis współautora publikacji

Chorzów, 11.05.2026
Miejsce i data

prof. dr hab. Marian Paluch
Imię i nazwisko współautora publikacji

Uniwersytet Śląski w Katowicach
Wydział Nauk Ścisłych i Technicznych
Instytut Fizyki im. A. Chełkowskiego
Afiliacja

OŚWIADCZENIE

Oświadczam, że w pracy:

A1. M. Rams-Baron, A. Błażytko, K. Jurkiewicz, P. Lodowski, M. Książek, J. Kusz, W. Mozga, M. Fordymacka, M. Teymouri, J. Krzywik & M. Paluch. Image of the solid-state rotary motion encoded in the dielectric response. Reports on Progress in Physics. 87, 108002 (2024), DOI: 10.1088/1361-6633/ad7288.

mój udział polegał na nadzorowaniu prowadzonych badań.

A2. A. Błażytko, M. Rams-Baron, M. Książek, J. Kusz, M. Matussek, J. Grelska & M. Paluch. Engineering of Rotational Dynamics via Polymorph Manipulation. The Journal of Physical Chemistry A, 128, 50 (2024). DOI: 10.1021/acs.jpca.4c04964.

mój udział polegał na konceptualizacji i nadzorowaniu badań oraz korekcji manuskryptu.

A3. A. Błażytko, M. Rams-Baron & M. Paluch. The influence of molecular shape on reorientation dynamics of sizable glass-forming isomers at ambient and elevated pressure. Scientific Reports, 14, 887 (2024). DOI: 10.1038/s41598-023-50894-8.

mój udział polegał na korekcji manuskryptu.

.....
Podpis współautora publikacji

Chorzów, 11.05.2026
Miejsce i data

dr hab. Marzena Rams-Baron, prof. UŚ
Imię i nazwisko współautora publikacji

Uniwersytet Śląski w Katowicach
Wydział Nauk Ścisłych i Technicznych
Instytut Fizyki im. A. Chełkowskiego
Afiliacja

OŚWIADCZENIE

Oświadczam, że w pracy:

A1. M. Rams-Baron, A. Błażytko, K. Jurkiewicz, P. Lodowski, M. Książek, J. Kusz, W. Mozga, M. Fordymacka, M. Teymouri, J. Krzywik & M. Paluch. Image of the solid-state rotary motion encoded in the dielectric response. Reports on Progress in Physics. 87, 108002 (2024), DOI: 10.1088/1361-6633/ad7288.

mój udział polegał na przygotowaniu manuskryptu, nadzorowaniu prowadzonych badań, analizie wyników i wykonaniu części eksperymentów za pomocą spektroskopii dielektrycznej.

A2. A. Błażytko, M. Rams-Baron, M. Książek, J. Kusz, M. Matussek, J. Grelska & M. Paluch. Engineering of Rotational Dynamics via Polymorph Manipulation. The Journal of Physical Chemistry A, 128, 50 (2024). DOI: 10.1021/acs.jpca.4c04964.

mój udział polegał na konceptualizacji badań, korekcji manuskryptu i zapewnieniu źródła finansowania.

A3. A. Błażytko, M. Rams-Baron & M. Paluch. The influence of molecular shape on reorientation dynamics of sizable glass-forming isomers at ambient and elevated pressure. Scientific Reports, 14, 887 (2024). DOI: 10.1038/s41598-023-50894-8.

mój udział polegał na nadzorowaniu badań i korekcji manuskryptu.

Marzena Rams-Baron
Podpis współautora publikacji

Chorzów, 11.05.2026
Miejsce i data

prof. dr hab. Joachim Kusz
Imię i nazwisko współautora publikacji

Uniwersytet Śląski w Katowicach
Wydział Nauk Ścisłych i Technicznych
Instytut Fizyki i. A. Chełkowskiego
Afiliacja

OŚWIADCZENIE

Oświadczam, że w pracy:

A1. M. Rams-Baron, A. Błażytko, K. Jurkiewicz, P. Lodowski, M. Książek, J. Kusz, W. Mozga, M. Fordymacka, M. Teymouri, J. Krzywik & M. Paluch. Image of the solid-state rotary motion encoded in the dielectric response. Reports on Progress in Physics. 87, 108002 (2024), DOI: 10.1088/1361-6633/ad7288.

A2. A. Błażytko, M. Rams-Baron, M. Książek, J. Kusz, M. Matussek, J. Grelska & M. Paluch. Engineering of Rotational Dynamics via Polymorph Manipulation. The Journal of Physical Chemistry A, 128, 50 (2024). DOI: 10.1021/acs.jpca.4c04964.

mój udział polegał na wykonaniu pomiarów XRD.

.....
Podpis współautora publikacji

Chorzów, 11.05.2026
Miejsce i data

dr inż. Karolina Jurkiewicz, prof. UŚ
Imię i nazwisko współautora publikacji

Uniwersytet Śląski w Katowicach
Wydział Nauk Ścisłych i Technicznych
Instytut Fizyki im. A. Chełkowskiego
Afiliacja

OŚWIADCZENIE

Oświadczam, że w pracy:

A1. M. Rams-Baron, A. Błażytko, K. Jurkiewicz, P. Lodowski, M. Książek, J. Kusz, W. Mozga, M. Fordymacka, M. Teymouri, J. Krzywik & M. Paluch. Image of the solid-state rotary motion encoded in the dielectric response. Reports on Progress in Physics. 87, 108002 (2024), DOI: 10.1088/1361-6633/ad7288.

mój udział polegał na wykonaniu pomiarów XRD i analizie wyników.

Jurkiewicz
.....
Podpis współautora publikacji

Chorzów, 11.05.2026
Miejsce i data

dr Maria Książek
Imię i nazwisko współautora publikacji

Uniwersytet Śląski w Katowicach
Wydział Nauk Ścisłych i Technicznych
Instytut Fizyki i. A. Chełkowskiego
Afiliacja

OŚWIADCZENIE

Oświadczam, że w pracy:

A1. M. Rams-Baron, A. Błażytko, K. Jurkiewicz, P. Lodowski, M. Książek, J. Kusz, W. Mozga, M. Fordymacka, M. Teymouri, J. Krzywik & M. Paluch. Image of the solid-state rotary motion encoded in the dielectric response. Reports on Progress in Physics. 87, 108002 (2024), DOI: 10.1088/1361-6633/ad7288.

A2. A. Błażytko, M. Rams-Baron, M. Książek, J. Kusz, M. Matussek, J. Grelska & M. Paluch. Engineering of Rotational Dynamics via Polymorph Manipulation. The Journal of Physical Chemistry A, 128, 50 (2024). DOI: 10.1021/acs.jpca.4c04964.

mój udział polegał na rozwiązaniu struktury krystalicznej badanych związków.

Maria Książek
.....
Podpis współautora publikacji

Warszawa, 12.05.2026
Miejsce i data

dr Joanna Grelska
Imię i nazwisko współautora publikacji

Uniwersytet Warszawski
Wydział Chemii
Zakład Chemii Teoretycznej i Strukturalnej
Afiliacja

OŚWIADCZENIE

Oświadczam, że w pracy:

A2. A. Błażytko, M. Rams-Baron, M. Książek, J. Kusz, M. Matussek, J. Grelska & M. Paluch. Engineering of Rotational Dynamics via Polymorph Manipulation. The Journal of Physical Chemistry A, 128, 50 (2024). DOI: 10.1021/acs.jpca.4c04964.

mój udział polegał na wykonaniu pomiarów XRD oraz analizie wyników.

Joanna Grelska
Podpis współautora publikacji

Kraków, 20.05.2026
Miejsce i data

dr inż. Julia Krzywik
Imię i nazwisko współautora publikacji

TriMen Chemicals Sp. z o.o.
Afiliacja

OŚWIADCZENIE

Oświadczam, że w pracy:

A1. M. Rams-Baron, A. Błażytko, K. Jurkiewicz, P. Lodowski, M. Książek, J. Kusz, W. Mozga, M. Fordymacka, M. Teymouri, J. Krzywik &M. Paluch. Image of the solid-state rotary motion encoded in the dielectric response. Reports on Progress in Physics. 87, 108002 (2024), DOI: 10.1088/1361-6633/ad7288.

mój udział polegał na syntezie opisanych związków: zaprojektowaniu ścieżek syntetycznych oraz optymalizacji poszczególnych ich etapów prowadzących ostatecznie do oczekiwanych cząsteczek.

.....Julia Krzywik.....
Podpis współautora publikacji

Chorzów, 11.05.2026
Miejsce i data

dr hab. Piotr Lodowski, prof. UŚ
Imię i nazwisko współautora publikacji

Uniwersytet Śląski w Katowicach
Wydział Nauk Ścisłych i Technicznych
Instytut Chemii
Afiliacja

OŚWIADCZENIE

Oświadczam, że w pracy:

A1. M. Rams-Baron, A. Błażytko, K. Jurkiewicz, P. Lodowski, M. Książek, J. Kusz, W. Mozga, M. Fordymacka, M. Teymouri, J. Krzywik & M. Paluch. Image of the solid-state rotary motion encoded in the dielectric response. Reports on Progress in Physics. 87, 108002 (2024), DOI: 10.1088/1361-6633/ad7288.

mój udział polegał na wykonaniu obliczeń DFT i analizie wyników.

.....
Podpis współautora publikacji

Chorzów, 11.05.2026
Miejsce i data

mgr inż. Witold Mozga
Imię i nazwisko współautora publikacji

Trimen Chemicals sp. z o.o.
Afiliacja

OŚWIADCZENIE

Oświadczam, że w pracy:

A1. M. Rams-Baron, A. Błażytko, K. Jurkiewicz, P. Lodowski, M. Książek, J. Kusz, W. Mozga, M. Fordymacka, M. Teymouri, J. Krzywik & M. Paluch. Image of the solid-state rotary motion encoded in the dielectric response. Reports on Progress in Physics. 87, 108002 (2024), DOI: 10.1088/1361-6633/ad7288.

mój udział polegał na syntezie badanych związków.

Witold Mozga

Podpis współautora publikacji

Chorzów, 11.05.2026
Miejsce i data

dr Marek Matussek
Imię i nazwisko współautora publikacji

Uniwersytet Śląski w Katowicach
Wydział Nauk Ścisłych i Technicznych
Instytut Chemii
Afiliacja

OŚWIADCZENIE

Oświadczam, że w pracy:

A2. A. Błażytko, M. Rams-Baron, M. Książek, J. Kusz, M. Matussek, J. Grelska & M. Paluch. Engineering of Rotational Dynamics via Polymorph Manipulation. The Journal of Physical Chemistry A, 128, 50 (2024). DOI: 10.1021/acs.jpca.4c04964.

mój udział polegał na charakteryzacji badanych związków za pomocą NMR i MS.

Matussek
.....
Podpis współautora publikacji

Chorzów, 11.05.2026
Miejsce i data

dr Marta Fordymacka
Imię i nazwisko współautora publikacji

Trimen Chemicals sp. z o.o.
Afiliacja

OŚWIADCZENIE

Oświadczam, że w pracy:

A1. M. Rams-Baron, A. Błażytko, K. Jurkiewicz, P. Lodowski, M. Książek, J. Kusz, W. Mozga, M. Fordymacka, M. Teymouri, J. Krzywik & M. Paluch. Image of the solid-state rotary motion encoded in the dielectric response. Reports on Progress in Physics. 87, 108002 (2024), DOI: 10.1088/1361-6633/ad7288.

mój udział polegał na syntezie badanych związków.

Marta Fordymacka
Podpis współautora publikacji

Chorzów, 11.05.2026
Miejsce i data

dr Mahshid Teymouri
Imię i nazwisko współautora publikacji

Trimen Chemicals sp. z o.o.
Afiliacja

OŚWIADCZENIE

Oświadczam, że w pracy:

A1. M. Rams-Baron, A. Błażytko, K. Jurkiewicz, P. Lodowski, M. Książek, J. Kusz, W. Mozga, M. Fordymacka, M. Teymouri, J. Krzywik & M. Paluch. Image of the solid-state rotary motion encoded in the dielectric response. Reports on Progress in Physics. 87, 108002 (2024). DOI: 10.1088/1361-6633/ad7288.

mój udział polegał na syntezie badanych związków.

Mahshid Teymouri Teymouri
Podpis współautora publikacji

4. Podsumowanie

Niniejszą rozprawę doktorską stanowi cykl trzech artykułów naukowych, w których przedstawiono wyniki badań na temat wpływu budowy molekularnej, położenia polarnego podstawnika oraz lokalnego otoczenia cząsteczki na dynamikę rotacji i relaksacji strukturalnej specjalnie zaprojektowanych, dużych i anizotropowych molekuł. Układy te umożliwiły analizę dynamiki wewnętrznej rotacji w stanie krystalicznym i szklistym, a także badanie relaksacji całych molekuł w stanie cieczy przechłodzonej. Główną techniką eksperymentalną wykorzystaną w pracy była szerokopasmowa spektroskopia dielektryczna, uzupełniona metodami kalorymetrycznymi i strukturalnymi.

W artykule A1 wykazano, że spektroskopia dielektryczna jest doskonałym narzędziem w badaniach rotacji wewnętrznej w amfidynamicznych kryształach. Na podstawie badań fluoropodstawionych rotorów fenylowych stwierdzono, że zmiana położenia i liczby atomów fluoru prowadzi do istotnych różnic w dynamice rotacji, mimo zachowania zbliżonej architektury całej molekuły. Analiza danych uzyskanych za pomocą BDS w oparciu o ADWP umożliwiła wyjaśnienie dwóch odmiennych wzorców temperaturowej ewolucji amplitudy maksimum strat dielektrycznych. Dla M-meta-F, gdzie obserwowano najniższą barierę rotacji oraz wzrost amplitudy procesu relaksacyjnego przy obniżaniu temperatury, model ADWP wskazał na niemal symetryczny potencjał rotacyjny. Z kolei dla M-ortho-F i M-2F spadek amplitudy maksimum strat wraz z obniżaniem temperatury został powiązany z większą asymetrią potencjału, wynikającą z silniejszej nierównoważności dostępnych orientacji rotora.

W kolejnym artykule A2 przeanalizowano wpływ otoczenia na dynamikę rotacji molekularnej. Wykazano, że ta sama cząsteczka, w zależności od sposobu upakowania w sieci krystalicznej, może wykazywać istotnie odmienne parametry rotacji. Uzyskane wyniki dowiodły, że zmiana formy polimorficznej prowadzi do znaczącej modyfikacji wysokości bariery aktywacji rotora. Oznacza to, że dynamika rotacji w ciele stałym może być kontrolowana nie tylko poprzez projektowanie nowej struktury chemicznej, lecz również poprzez manipulację organizacją cząsteczek w krysztale. Analiza strukturalna wykazała, że kluczowe znaczenie mają liczba, geometria i charakter kontaktów typu C-H···F pomiędzy rotorem a jego otoczeniem.

W artykule A3 badania za pomocą spektroskopii dielektrycznej trzech izomerów w fazie cieczy przechłodzonej zawierających grupę trifluorometylową w pozycji orto, meta oraz para wykazały, że nawet przy identycznej masie molowej i składzie chemicznym zmiana położenia

polarnego podstawnika prowadzi do istotnych różnic w dynamice molekularnej. Zaobserwowano różnice w temperaturze topnienia, temperaturze zeszklenia, zdolności do rekrystalizacji oraz w kształcie widm relaksacji dielektrycznej. Istotnym było zaobserwowanie bimodalnego charakteru relaksacji strukturalnej dla izomeru meta-CF_3 w wysokich temperaturach, co zinterpretowano jako rozdzielenie czasów reorientacji względem długiej i krótkiej osi molekuły. Badania wysokociśnieniowe wykazały ponadto, że duże anizotropowe izomery szkłotwórcze charakteryzują się bardzo wysoką wrażliwością dynamiki reorientacyjnej na kompresję. Co istotne, uzyskane wyniki nie tylko zwalidowały korelację pomiędzy objętością aktywacji a promieniem korelacji, lecz także rozszerzyły zakres jej obowiązywania na skrajne przypadki dużych molekuł szkłotwórczych.

Uzyskane wyniki pozwoliły sformułować kilka ogólnych wniosków. Po pierwsze, dynamika rotacji molekularnej jest silnie zależna od lokalnego otoczenia rotora i nie może być opisywana wyłącznie na podstawie struktury chemicznej samego fragmentu rotującego. Po drugie, odpowiedź dielektryczna dostarcza cennych informacji o mechanizmie rotacji, asymetrii potencjału oraz rodzaju oddziaływań obecnych w strukturze krystalicznej. Po trzecie, sposób upakowania cząsteczek w krysztale może być wykorzystany jako narzędzie kontroli dynamiki rotacji, co potwierdza znaczenie polimorfizmu w projektowaniu materiałów amfidynamicznych. Po czwarte, w przypadku dużych cieczy szkłotwórczych kształt cząsteczki i orientacja momentu dipolowego determinują zarówno kształt widm dielektrycznych, jak i charakter relaksacji strukturalnej, wrażliwość dynamiki cząsteczkowej na ciśnienie oraz stopień kooperatywności ruchów molekularnych.

Otrzymane wyniki poszerzają wiedzę na temat zależności pomiędzy strukturą molekularną i oddziaływaniem z otoczeniem a dynamiką w układach amfidynamicznych oraz szkłotwórczych. Stanowią one również podstawę do dalszych badań nad projektowaniem materiałów o kontrolowanych właściwościach dynamicznych, istotnych z punktu widzenia rozwoju przyszłych układów funkcjonalnych i elementów maszyn molekularnych.

5. Bibliografia

1. D. A. Leigh, Genesis of the Nanomachines: The 2016 Nobel Prize in Chemistry. *Angewandte Chemie* **128**, 14722–14724 (2016).

2. G. J. Simpson, V. García-López, A. Daniel Boese, J. M. Tour, L. Grill, How to control single-molecule rotation. *Nat. Commun.* **10**, 1–6 (2019).

3. J. Perego, S. Bracco, M. Negroni, C. X. Bezuidenhout, G. Prando, P. Carretta, A. Comotti, P. Sozzani, Fast motion of molecular rotors in metal–organic framework struts at very low temperatures. *Nat. Chem.* **12**, 845–851 (2020).

4. G. S. Kottas, L. I. Clarke, D. Horinek, J. Michl, Artificial molecular rotors. [Preprint] (2005). https://doi.org/10.1021/cr0300993.

5. L. Catalano, P. Naumov, Exploiting rotational motion in molecular crystals. *CrystEngComm* **20**, 5872–5883 (2018).

6. C. S. Vogelsberg, M. A. Garcia-Garibay, Crystalline molecular machines: Function, phase order, dimensionality, and composition. *Chem. Soc. Rev.* **41**, 1892–1910 (2012).

7. G. Floudas, M. Paluch, A. Grzybowski, K. L. Ngai, *Molecular Dynamics of Glass-Forming Systems. Effects of Pressure* (Springer Science & Business Media, 2010).

8. R. Richert, Heterogeneous dynamics in liquids: fluctuations in space and time. *J. Phys.: Condens. Matter* **14**, 703–738 (2002).

9. P. G. Debenedetti, F. H. Stillinger, Supercooled liquids and the glass transition. *Nature* **410** (2001).

10. K. L. Ngai, M. Paluch, Classification of secondary relaxation in glass-formers based on dynamic properties. *Journal of Chemical Physics* **120**, 857–873 (2004).

11. G. P. Johari, Glass transition and secondary relaxations in molecular liquids and crystals. *Ann. N. Y. Acad. Sci.* **279**, 117–140 (1976).

12. G. P. Johari, Localized molecular motions of b-relaxation and its energy landscape. *J. Non. Cryst. Solids*, 307–310 (2002).

13. S. D. Karlen, M. A. Garcia-Garibay, “Amphidynamic crystals: Structural blueprints for molecular machines” in *Topics in Current Chemistry* (2005)vol. 262, pp. 179–227.

14. K. Skopek, M. C. Hershberger, J. A. Gladysz, Gyroscopes and the chemical literature: 1852-2002. *Coord. Chem. Rev.* **251**, 1723–1733 (2007).

15. M. A. Garcia-Garibay, C. E. Godinez, Engineering crystal packing and internal dynamics in molecular gyroscopes by refining their components. Fast exchange of a phenylene rotator by 2H NMR. *Cryst. Growth Des.* **9**, 3124–3128 (2009).

16. P. Commins, J. E. Nunez, M. A. Garcia-Garibay, Synthesis of bridged molecular gyroscopes with closed topologies: Triple one-pot macrocyclization. *Journal of Organic Chemistry* **76**, 8355–8363 (2011).

17. X. Jiang, B. Rodríguez-Molina, N. Nazarian, M. A. Garcia-Garibay, Rotation of a bulky triptycene in the solid state: Toward engineered nanoscale artificial molecular machines. *J. Am. Chem. Soc.* **136**, 8871–8874 (2014).

18. W. Setaka, K. Yamaguchi, Order-disorder transition of dipolar rotor in a crystalline molecular gyrotop and its optical change. *J. Am. Chem. Soc.* **135**, 14560–14563 (2013).

19. J. E. Nuñez, A. Natarajan, S. I. Khan, M. A. Garcia-Garibay, Synthesis of a triply-bridged molecular gyroscope by a directed meridional cyclization strategy. *Org. Lett.* **9**, 3559–3561 (2007).

20. K. Zhu, C. A. O'Keefe, V. N. Vukotic, R. W. Schurko, S. J. Loeb, A molecular shuttle that operates inside a metal-organic framework. *Nat. Chem.* **7**, 514–519 (2015).

21. G. Baggi, B. H. Wilson, A. Dhara, C. A. O'Keefe, R. W. Schurko, S. J. Loeb, Dynamics of a [2]rotaxane wheel in a crystalline molecular solid. *Chemical Communications* **57**, 8210–8213 (2021).

22. Z. Liu, Y. Wang, M. A. Garcia-Garibay, Rotational Dynamics of an Amphidynamic Zirconium Metal-Organic Framework Determined by Dielectric Spectroscopy. *Journal of Physical Chemistry Letters* **12**, 5644–5648 (2021).

23. S. L. Gould, D. Tranchemontagne, O. M. Yaghi, M. A. Garcia-Garibay, Amphidynamic character of crystalline MOF-5: Rotational dynamics of terephthalate phenylenes in a free-volume, sterically unhindered environment. *J. Am. Chem. Soc.* **130**, 3246–3247 (2008).

24. A. Navarro-Huerta, T. Matsuo, A. S. Mikherdov, J. Blahut, E. Bartůňková, P. Jiang, M. Dračínský, S. Teat, M. Jin, S. Hayashi, B. Rodríguez-Molina, Optical Waveguiding Charge-Transfer Cocrystals: Examining the Impact of Molecular Rotations on Their Photoluminescence. *J. Am. Chem. Soc.* **147**, 8343–8349 (2025).

25. A. Navarro-Huerta, M. J. Jellen, J. Arcudia, S. J. Teat, R. A. Toscano, G. Merino, B. Rodríguez-Molina, Tailoring the cavities of hydrogen-bonded amphidynamic crystals using weak contacts: Towards faster molecular machines. *Chem. Sci.* **12**, 2181–2188 (2021).

26. C. M. Roland, S. Hensel-Bielowka, M. Paluch, R. Casalini, Supercooled dynamics of glass-forming liquids and polymers under hydrostatic pressure. *Reports on Progress in Physics* **68**, 1405–1478 (2005).

27. G. L. Hoatson, R. L. Vold, *2H-NMR Spectroscopy of Solids and Liquid Crystals* (Springer-Verlag Berlin Heidelberg, 1994).

28. D. Michell, F. Engelke, "Cross-Polarization, Relaxation Times and Spin-Diffusion in Rotating Solids" (Springer-Verlag Berlin Heidelberg, 1994).

29. F. Kremer, A. Schonhals, *Broadband Dielectric Spectroscopy* (Springer, Berlin, Heidelberg, 2003).

30. F. Kremer, A. Loidl, *The Scaling of Relaxation Processes* (Springer, 2018; http://www.springer.com/series/8283).

31. I. Liepuoniute, C. M. Huynh, S. Perez-Estrada, Y. Wang, S. Khan, K. N. Houk, M. A. Garcia-Garibay, Enhanced Rotation by Ground State Destabilization in Amphidynamic Crystals of a Dipolar 2,3-Difluorophenylene Rotator as Established by Solid State 2H NMR and Dielectric Spectroscopy. *Journal of Physical Chemistry C* **124**, 15391–15398 (2020).

32. Y. B. Tong, L. Te Ren, H. B. Duan, J. L. Liu, X. M. Ren, An amphidynamic inorganic-organic hybrid crystal of bromoplumbate with 1,5-bis(1-methylimidazolium)pentane exhibiting multi-functionality of a dielectric anomaly and temperature-dependent dual band emissions. *Dalton Transactions* **44**, 17850–17858 (2015).

33. R. D. Horansky, L. I. Clarke, J. C. Price, T. A. V. Khuong, P. D. Jarowski, M. A. Garcia-Garibay, Dielectric response of a dipolar molecular rotor crystal. *Phys. Rev. B Condens. Matter Mater. Phys.* **72** (2005).

34. J. Harada, M. Ohtani, Y. Takahashi, T. Inabe, Molecular Motion, Dielectric Response, and Phase Transition of Charge-Transfer Crystals: Acquired Dynamic and Dielectric Properties of Polar Molecules in Crystals. *J. Am. Chem. Soc.* **137**, 4477–4486 (2015).

35. R. D. Horansky, L. I. Clarke, E. B. Winston, J. C. Price, S. D. Karlen, P. D. Jarowski, R. Santillan, M. A. Garcia-Garibay, Dipolar rotor-rotor interactions in a difluorobenzene molecular rotor crystal. *Phys. Rev. B Condens. Matter Mater. Phys.* **74** (2006).